CORROSION PERFORMANCE OF MIG WELDED CU-LEAN AA7XXX ALLOYS

CORROSION PERFORMANCE OF MIG WELDED CU-LEAN AA7XXX ALLOYS

By JACEK DABROWSKI, B.ENG

A Thesis Submitted to the School of Graduate Studies in Partial Fulfillment of the Requirements for the Degree Master of Applied Science

MASTER OF APPLIED SCIENCE (2015)

The Department of Materials Science and Engineering

McMaster University, Hamilton, Ontario, Canada

TITLE: Corrosion Performance of MIG Welded Cu-Lean AA7xxx Alloys

AUTHOR: Jacek Dabrowski, B.Eng (McMaster University)

SUPERVISOR: Dr. Joseph R. Kish

NUMBER OF PAGES: xvii, 174

Abstract

An investigation was undertaken to better understand the corrosion behaviour of dissimilar welded Cu-lean AA7003 and AA7108 extrusions. The major variables under study were the heat-treated condition (as-welded T6 vs. as-welded T6+Paint Bake (PB)), extrusion alloy Cu composition (AA7003 vs. AA7108), weld filler composition (ER4043 vs. ER5356), weld joint geometry (lap-joint vs. T-joint), and weld direction with respect to extrusion direction (parallel (═) vs. perpendicular (⊥)). The corrosion behaviour of the various weld configurations under investigation was observed using an ASTM standard practice for modified salt spray testing (ASTM G85-A2), a GM worldwide engineering standard for cyclic corrosion testing (GMW-14872), and potentiodynamic polarization measurements. The effect of exposure to GMW-14872 on the tensile-shear behaviour of the various weld configurations under study was also investigated using a custom tensile jig.

Examination post exposure to ASMT G85-A2 revealed the presence of differing pitting corrosion morphologies between AA7003 and AA7108. Due to increased Cu-content, AA7003 displayed deep pitting corrosion which penetrated the entirety of the dynamically recrystallized top surface layer and reached the fine-grained interior. Shallow pitting of the recrystallized surface layer was observed on AA7108, with very few penetration sites that reached the underlying fine-grained interior.

No difference in corrosion behaviour was observed between the heat affected zone (HAZ) and unaffected base alloy of welded AA7003 and AA7108, also consistent with

potentiodynamic polarization results. However, the HAZ displayed dual corrosion bands separated by a thin band of unattacked alloy; a result of distinct local microstructural changes induced by thermal cycling from welding.

Tensile-shear testing revealed four types of observed fracture modes: shear across the weld throat, fracture along the AA7xxx/ER5356 interface, fracture along the AA6063/ER5356 interface and fracture in the HAZ of AA7xxx. Little to no corrosion was observed on weld configurations exposed to GMW-14872, resulting in no differences in the tensile-shear behaviour of exposed and unexposed weld configurations. Large variations observed in the tensile-shear results were a result of numerous weld defects.

Acknowledgements

Firstly, I would like to thank my supervisor, Dr. Joseph Kish, for sharing his guidance, motivation, and enthusiastic approach to corrosion science which enabled me to persevere through challenging situations. His continuous support and helpful discussions were instrumental to the completion of this research and thesis.

Secondly, I would like to thank the technical staff at the Centre for Automotive Materials and Corrosion (CAMC), Dr. Michael Bruhis and Connie Barry. Dr. Bruhis' wealth of material mechanics knowledge was invaluable, and his generosity in sharing his insights is greatly appreciated. I would also like to extend my thanks to the technical staff of the McMaster University Department of Materials Science and Engineering (MSE), primarily, Doug Culley, Ed McCaffery, and Xiaogang Li for their in-lab support.

Moreover, the kind financial support provided by the Initiative for Automotive Manufacturing Innovation (iAMi) and General Motors of Canada Limited is greatly appreciated. I would like to thank Kevin Wong from Alcan Automotive Structures & Design and Darren Edmison from General Motors of Canada Limited for their technical assistance and for providing the welded bumper assemblies.

Finally, I would like to thank my colleagues at the Walter Smeltzer Corrosion Laboratory for their mentorship and hours of discussion. I would also like to thank my friends and close family, particularly my parents, who showed unconditional support and love throughout this journey.

Table of Contents

Table of Figures

Appendix Table of Figures

1.0 Introduction

Bumper assemblies are an important passive safety feature found on automobiles, as they are one of the main structures that absorb energy in the event of an automobile collision. Current automotive aluminum bumper assemblies are typically fabricated using heat-treatable AA6xxx-series (Al-Mg-Si) with medium to high strength, toughness, energy absorption, weldability, and formability. In this context, Cu-lean AA7xxx extrusions such as AA7003 and AA7108 which exhibit higher strength than AA6xxx extrusions, represent an attractive alternative light-weight material from which to fabricate bumper assemblies [1], [2].

Arc welding (MIG) is becoming a key joining process for AA7xxx alloys within the transportation industry. A major technological issue preventing widespread utilization of arc-welded AA7xxx joints is limited due to the susceptibility to severe localized corrosion [3], [4], which generally occurs as exfoliation corrosion within the HAZ or as a type of stress corrosion cracking which initiates at the weld toe and propagates into the interfacial region between the weld bead and the HAZ (termed the "white zone"). The typically observed exfoliation corrosion occurs in elongated (deformed) grain structures and involves a galvanic interaction between grain boundary region and the adjacent solute depleted matrix. Consequently, key factors that influence the susceptibility of AA7xxx alloys to exfoliation corrosion include the grain shape (alloying and the degree of cold deformation) and the heat-treated condition (temper). High strength AA7xxx alloys with low aspect ratio grain structures tend to have a lower susceptibility to exfoliation

corrosion due to the decreased length of the intergranular path [5], [6]. In a similar manner, the coarse recrystallized surface layer has also been found to have a beneficial influence on the exfoliation corrosion as compared to the fibrous interior of AA7xxx alloys [7].

Relative to the solution treated condition, an over-aged condition has been commonly observed to have a beneficial effect on the susceptibility to exfoliation corrosion of Cu-rich and Cu-lean AA7xxx alloys by way of reducing the rate of intergranular corrosion [8], [9]. The beneficial influence has been primarily attributed to the lack of a continuous layer of grain boundary precipitates, as a result of coarsening [10]. Using thin film analogues of intermetallic phases to investigate the mechanism of intergranular corrosion in Cu-rich AA7xxx alloys, Ramgopal et al. [11], [12] showed that the dissolution potential of the η-$MgZn_2$ phase is much lower than the pitting potential of the base alloy. They conclude that the grain boundary phase (η-$MgZn_2$) tends to preferentially dissolve at potentials where the matrix is still passive. Moreover, they determined that precipitate dissolution and the resulting microchemistry, which is dependent on heat-treatment history, plays a significant role in controlling the intergranular corrosion. However, little work has been done to investigate the effect of an automotive paint-bake heat-treatment cycle on the corrosion behaviour of Cu-lean AA7xxx alloys [13].

In addition to the micro-galvanic cell activity induced by the intermetallic constituents and strengthening particles present, there is strong evidence to suggest that

macro-galvanic cell activity between the weld bead and base AA7xxx alloy may also be playing a controlling role. Electrochemical profiles taken in cross-section across MIG welded joints during exposure to saline solutions suggest that a potential difference exists across the AA7xxx welded joint [14], [15], [16]. These studies consistently show that the HAZ and base alloy are more electronegative with respect to the weld bead (MIG-welded with AA5xxx filler wire).

The majority of recent corrosion research efforts into welded AA7xxx alloys has been focused on Cu-rich alloys, due to their widespread use in the aerospace industry and friction stir welding, due to the processes' low thermal input [17], [18], [19]. This leaves a significant gap in literature concerning the corrosion behaviour of welded Cu-lean AA7xxx alloys.

This study was undertaken to investigate the corrosion behaviour of welded Cu-lean AA7003 and AA7108. The major variables under study were: the heat-treated condition (as-welded T6 vs. as-welded T6+PB), extrusion alloy Cu composition (AA7003 vs. AA7108), weld filler composition (ER4043 vs. ER5356), weld joint geometry (lap-joint vs. T-joint), and weld direction with respect to extrusion direction (parallel (═) vs. perpendicular (⊥)). The effects of the aforementioned variables on the corrosion behaviour of welded AA7003 and AA7108 using ASTM and GM Worldwide Engineering standardized cyclic corrosion tests and potentiodynamic polarization scans are demonstrated in this thesis. Additionally, the effect of corrosion on the tensile-shear behaviour of the various weld configurations utilizing a custom made tensile-shear jig is

shown. Finally, the corrosion behaviours observed between the two unaffected base alloys, the corrosion found in the HAZ, differing corrosion behaviours found between the variables of interest, and the effect of exposure to GMW-14872 on the tensile-shear behaviour on welded AA7003 and AA7108 are discussed.

2.0 Literature Review

2.1 Microstructure of AA7xxx alloys

AA7xxx alloys belong to the Al-Zn-Mg-(Cu) family of aluminum alloys, which obtain their strength from age-hardening due to the precipitation of Zn and Mg from solid solution [20]. Cu additions have been found to increase the age-hardening response by increasing precipitation within the matrix [21]. Moreover, due to the complicated interactions between the Al solid solution and major (Cu, Mg, Zn) and minor (Fe, Si, Mn, Zr) alloying additions, results in a heterogeneous microstructure. The resulting microstructure consists of two physiochemically differing areas: the grain matrix and the grain boundary regions. The grain matrix contains three types of second-phase particles: fine strengthening precipitates, coarse intermetallics, and dispersoids, whereas the grain boundary region is characterized by a precipitate-free zone (PFZ) and grain boundary precipitates [22].

2.1.1 Strengthening Precipitates

AA7xxx alloys inherit their medium to high strength from the precipitation of Guinier-Preston (GP) zones and the metastable η' phase [23]. The precipitation of these phases is a result of aging (tempering/heat-treating) the supersaturated solid solution (α). The precipitation sequence of AA7xxx alloys has been studied extensively and is summarized by the following [24], [25], [26]:

$$\alpha \rightarrow \alpha + \text{GP-zones} \rightarrow \alpha + \eta' \rightarrow \alpha + \eta \qquad \text{Equation [1]}$$

$$\alpha \rightarrow \alpha + \text{GP-zones} \rightarrow \alpha + \tau' \rightarrow \alpha + \tau \qquad \text{Equation [2]}$$

The three precipitate phases present in the grain matrix are: GP-zones, the metastable η' phase, and the equilibrium η phase. The chemical composition of all three phases is generally accepted as $MgZn_2$ [20]- [26]. The τ-phase, $Al_2Mg_3Zn_3$, is typically observed in Cu-free AA7xxx alloys and is not observed during commercial heat-treatments [26].

GP-zones form as fine (≈ Å) spherical solute atom clusters that are coherent with the Al matrix, and which have nucleated either homogeneously or heterogeneously at vacancies and dislocations [27]. The composition of GP-zones is difficult to measure due to their size, but their Zn-Mg ratio is believed to range from 1-1.3 [24], [28], [29], [30]. Transformation of, or subsequent nucleation on, GP-zones leads to the formation of the metastable η' phase. η' precipitates are plate-like and semi-coherent with the surrounding matrix and their Zn-Mg ratio is believed to range from 1-1.5 [27], [31], [32] . Subsequent transformation leads to the equilibrium η phase, which can also be heterogeneously nucleated at grain boundaries, dislocations, and dispersoid particles [27], [33] . The η phase is the largest of the three phases and is incoherent with the matrix exhibiting a plate or rod-like shape, with a Zn-Mg ratio of approximately 2 [24], [27], [34] .

Upon heat-treatment, peak-aged (T6) AA7xxx alloys contain a high concentration of the η' phase in the grain interior with the η phase located on grain boundaries. In comparison, the over-aged (T7) alloys contain a smaller concentration of η phase particles, which have increased both in size and spacing, within the grain matrix and on the grain boundaries [35], [36], [37]. In Cu-containing AA7xxx alloys the η' and η phase

are believed to have the composition $Mg(Al, Cu, Zn)_2$ with Cu-content of the precipitates increasing with aging time [25], [31].

Grain boundaries are characterized by a single precipitate phase (η phase) and a PFZ, as shown in Figure 1. Grain boundary precipitate compositions have been shown to depend on Cu-content of the alloy [38]. The grain boundary precipitates of low Cu-content AA7004 (4.3Zn-1.6Mg-0.01Cu) were determined to be $MgZn_2$. Increased Cu-content of various AA7xxx alloys showed a decrease in the Zn content of $Mg(Cu, Zn, Al)_2$ precipitates with an increase in alloy Cu-content. Mg and Al content appeared largely unchanged. Similar conclusions were drawn for precipitates within the grain interior.

PFZs are believed to be a result of either solute depletion in the vicinity of the grain boundary due to grain boundary precipitation or a depletion of the critical number of vacancies required for precipitation [39], [40]. An investigation [41] into the composition of the PFZ of AA7075 (5.5Zn-2.4Mg-1.55Cu) in the T6 and T7 conditions revealed a depletion of Zn across the PFZ in both tempers. However, Cu-concentration across the PFZ was found to decrease within the over-aged (T7) condition compared to the T6. A study [42] conducted on AA7449 (8.5Zn-2.1Mg-1.9Cu) in the T6, T79, and T76 tempers also revealed a similar conclusion. The Zn-content was depleted across the PFZ of all tempers with a decrease in Cu-content upon over-aging to either the T79 or T76 conditions.

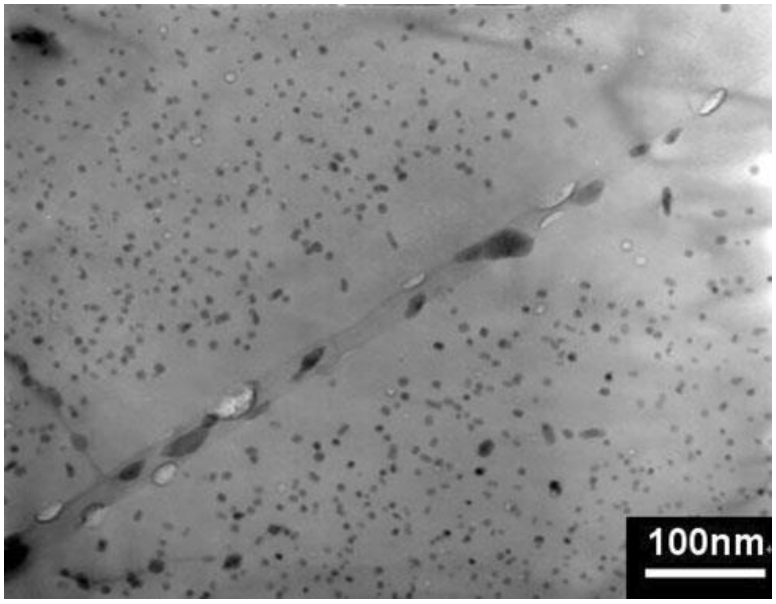

Figure 1: The typical appearance of the grain boundary region of AA7005-T73 (4.4Zn-1.3Mg-0.01Cu) denoted by the presence of grain boundary precipitates and a PFZ **[43]**.

2.1.2 Intermetallic Particles

Intermetallics are large, irregular shaped particles that are formed during casting and ingot homogenization. These particles arise from the interaction between major alloying elements (Zn, Mg, Cu) and minor alloying elements (Fe, Mn, Si). Minor alloying elements with a low solubility in Al solid solution form during solidification and interact with the major alloying elements to form intermetallic particles [44]. Intermetallics tend to vary in size from 1-20 μm. Unlike strengthening precipitates, intermetallic particles do not distribute uniformly throughout the grain matrix. They instead form in localized clusters in regions of high alloying content [45]. Subsequent mechanical processing (rolling or extrusion) breaks up the clusters of intermetallic particles and aligns them as bands that are parallel to the working direction.

Intermetallic particles which have been observed in various Cu-rich AA7xxx alloys are: Al_7Cu_2Fe, $(Al,Cu)_6(Fe,Cu)$, and Mg_2Si. Less frequently occurring particles are: Al_3Fe, Al_2CuMg, $Al_{12}(Fe,Mn)_3Si$, and Mg(Al,Cu) [24], [46], [47], [48]. However, in Cu-lean AA7xxx alloys, no Cu-containing intermetallics have been observed. Instead, Mg_2Si and Al(Fe,Mn)SiZn particles were observed in AA7003 (5.5Zn-0.8Mg) [49], and Al_3Fe and $Al_3(Fe,Si)$ were observed in AA7004 (4.3Zn-1.6Mg-0.01Cu) and AA7039 (4.0Zn-2.9Mg-0.08Cu) [38]. However, it must be stated that not all of the aforementioned intermetallic particles appear simultaneously. The chemistries and frequencies of such particles are dictated by alloy composition and thermal history.

Upon the application of different tempers (T6 and T7) on AA7075 (5.8Zn-2.5Mg-1.4Cu) and AA7475 (5.9Zn-2.4Mg-1.6Cu) intermetallic particles have been observed to not undergo any physiochemical changes [46]. However, at higher temperature homogenization treatments Al_3Fe and Al_7Cu_2Fe have been found to transform into AlFeSi [50].

2.1.3 Dispersoids

Dispersoids are formed during solidification or homogenization by the interaction of Cr, Zr, Ti, Mn with Al. They are typically 1 μm in size with little to no solubility in Al. Dispersoids suppress grain boundary movement and decrease quench sensitivity [51]. Dispersoid particles that have been observed in AA7xxx alloys are: Al_3Ti, Al_3Zr, Al_6Mn, $Al_{20}Cu_2Mn_3$, and $Al_{18}Mg_3Cr_2$ [51], [46], [52]. Zr is believed to refine grain size without effecting quench sensitivity, but Cr is believed to increase quench sensitivity [51].

Although not effected by commercial tempering temperatures, dispersoid particles have been observed to undergo changes during homogenization treatments of AA7xxx alloys [53], [54]. Homogenizing AA7050 (6.3Zn-2.3Mg-2.3Cu) at 495°C led to higher Zr solubility and diffusion rates. This subsequently led to the formation of a lowered volume fraction of larger dispersoids and minimized the potential of Zr to inhibit recrystallization. A lower homogenization temperature of 475°C reduced the overall recrystallization fraction by half compared to 495°C.

Al_3Zr particles in AA7108 (5.5Zn-1.2Mg) and Al-6.1Zn-2.3Mg have been discovered to act as heterogeneous nucleation sites for η' phase precipitates during slow cooling rates, creating a PFZ around the η' particle as a result of local solute depletion. This hindered the precipitation of GP-zones and the subsequent transformation to the metastable η phase in the heterogeneous nucleation site vicinity [55], [56]. An investigation of Al-5.8Zn-0.8Mg showed that the Al_3Zr/Al interface acted as a vacancy sink, which reduced the amount of vacancies locally available for formation of GP-zones and for the nucleation of subsequent hardening precipitates [57].

2.2 Localized Corrosion of AA7xxx Alloys

The heterogeneous microstructure of AA7xxx alloys that results from alloying creates second-phase particles and grain boundary regions that exhibit electrochemical behaviour differing from the matrix, making AA7xxx alloys susceptible to localized forms of corrosion. The main forms of observed localized corrosion in AA7xxx are pitting corrosion and intergranular corrosion (IGC). Depending on the grain structure and

environmental conditions, IGC can take the form of exfoliation corrosion or stress-corrosion cracking (SCC). A summary of the localized corrosion behaviour of AA7xxx is given in the following sections.

2.2.1 Pitting Corrosion

Pitting corrosion is a localized form of corrosion that is denoted by small cavities created in the material after exposure to a corrosive environment. Pitting initiation occurs at a critical pitting potential (E_{pit}), also referred to as the breakdown potential (E_{brk}), at which point the passive surface film begins to locally rupture or break down in the presence of aggressive anions such as Cl^- [58], [59], [60]. In pure Al, the pitting resistance depends on the stability of the passive film. However, in Al-alloys, pitting is influenced by second-phase particles, which exhibit differing surface film characteristics than the solid solution matrix as a result of micro-galvanic coupling with the surrounding matrix [61].

To better understand pitting corrosion of AA7xxx alloys, investigations into the electrochemical behaviour of various second-phase particles were undertaken by Birbilis and Buchheit [62], [63]. A summary of the corrosion and pitting potentials (E_{corr} and E_{pit}) for various second-phase particles and the matrix of AA7X75 (3-4Zn-2-3Mg-0.5-1Cu) is provided in Table 1. From Table 1 it is observed that particles containing Cu, Fe, Mn, Ti, and Zr exhibited a less active E_{corr} than the AA7X75 matrix and displayed a unique E_{pit}. As a consequence, these particles can form a passive film in a potential range between their respective E_{corr} and E_{pit}. At E_{corr} values of these particles, the AA7X75 matrix

underwent high rates of anodic dissolution. Less active particles containing Fe and Cu were able to sustain large cathodic currents. Less active particles containing Mn, Ti and Zr, primarily dispersoids, were only capable of sustaining small cathodic currents and are believed to not be associated with pitting of AA7xxx. Second-phase particles containing Mg, Si and Zn were observed to be more active than the matrix with no observed E_{pit}, allowing them to corrode without a passive film at potentials above their respective E_{corr}. At matrix E_{corr} values, these particles underwent anodic dissolution.

Table 1: E_{corr} and E_{pit} of various second-phase particles and AA7X75 matrix [61].

Second-phase particle	E_{corr} (mV SCE in .1M NaCl)	E_{pit} (mV SCE in .1M NaCl)
Al_3Fe	-539	106
Al_7Cu_2Fe	-551	-448
Al_3Ti	-603	-225
Al_3Zr	-776	-275
Al_6Mn	-779	-755
Al_2CuMg	-883	80
Mg(Al,Cu)	-943	-2
AA7X75 Matrix	-965	-739
$Al_{32}Zn_{49}$	-1004	-
Mg_2Al_3	-1013	-846
$MgZn_2$	-1029	-
Mg_2Si	-1538	-

Second-phase particles can either be anodic (more active) or cathodic (less active) relative to the matrix, allowing for two types of pit morphologies to be observed in Al alloys: circumferential pitting and selective dissolution of the second-phase particle [64], [65], [66]. Circumferential pitting is characterized by attack of the matrix surrounding the less active second-phase particle. In AA7075-T651 (3-4Zn-2-3Mg-.5-1Cu), this has been observed around particles of Al_7Cu_2Fe [67]. Attack around the particles appeared as trenches seen in Figure 2. An explanation for this behaviour is that a galvanic couple between the less active particle and the active matrix is present. It is believed that the ability of the less active secondary-phase particles to sustain high cathodic currents increases the local pH, by oxygen reduction, which results in local breakdown of the passive film around the particle [68], [69]. Similar attack of the matrix surrounding the less active $(Al,Cu)_6(Fe,Cu)$ and $Al_{23}CuFe_4$ particles has also been observed in AA7075 (5.4Zn-2.4Mg-1.5Cu) [70], [71].

The second observed pit morphology is characterized by anodic dissolution of the more active second-phase particle relative to the less active matrix. Particles such as Mg_2Si and the strengthening particles $MgZn_2$ undergo dissolution relative to the matrix of Cu-rich AA7075 [62], [72]. However, due to the smaller volume fraction of Mg_2Si [48], [46] observed in AA7075, it is believed $MgZn_2$ plays the greater role [72]. More active second-phase particles are believed to be less detrimental to the pitting resistance of AA7xxx alloys than less active particles because more active particles are removed by dissolution whereas less active particles remain in the matrix promoting a continuous galvanic couple with the surrounding matrix [72], [73], [71].

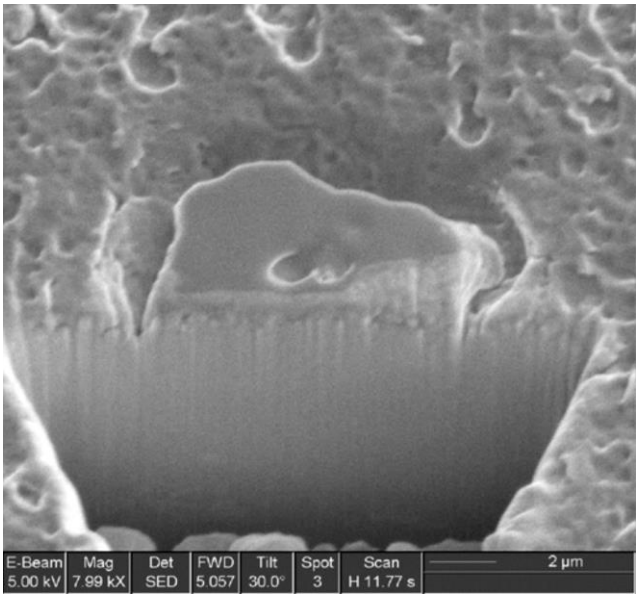

Figure 2: SEM image of an Al_7Cu_2Fe cross-sectioned with a focused ion beam of an AA7075-T651 sample exposed to 0.1M NaCl **[67]**.

Certain second-phase particles present in AA7xxx alloys, which contain less active elements (Cu and Fe), have been observed to undergo pole reversal, starting off active to the matrix and becoming less active with time [60], [74]. An investigation of Al_3Fe particles in alkaline sodium hydroxide (NaOH) solution has shown that at first the particle underwent anodic dissolution of Al until the particle was enriched in Fe. Once enriched in Fe it became cathodic relative to the matrix, enhancing the anodic dissolution of the matrix. It was observed that additions of Mn and Si to Al_3Fe particles, Al(Fe,Mn)Si and AlFeSi, were able to suppress the cathodic reaction of such particles, which lowered the dissolution rate of the matrix. Similar observations were made about Al_2CuMg through anodic polarization scans in 0.5 M NaCl [75], [76] . It was observed that under anodic polarization Cu dealloyed from the intermetallic particle. Upon liberation into the solution, the Cu ions adsorbed onto the alloy's surface, forming a porous Cu-rich

structure which reversed its galvanic relationship with the matrix becoming highly cathodic relative to the matrix.

The effects of various tempers (W, T6 and T7) on the pitting corrosion behaviour of AA7075 have been investigated [70], [72]. Attention was focused on the potential difference between Al_7Cu_2Fe and $(Al,Cu)_6(Fe,Cu)$ particles and the matrix. The largest potential difference was observed in the W-temper: +604 mV and +500 mV, for Al_7Cu_2Fe and $(Al,Cu)_6(Fe,Cu)$ respectively. This large potential difference was attributed to the high solute (Mg and Zn) concentration in the matrix as a result of the solutionizing heat-treatment of the W-temper. The T6-temper exhibited a potential difference of +320 mV and +375 mV between the matrix and Al_7Cu_2Fe and $(Al,Cu)_6(Fe,Cu)$ particles, respectively. This lowered potential difference was attributed to the precipitation of $MgZn_2$, which lowers the solute content of Zn and Mg in the matrix. The potential difference of the T7-temper was slightly higher than the T6-temper, +375 mV and +430 mV between Al_7Cu_2Fe and $(Al,Cu)_6(Fe,Cu)$ particles, respectively. This was attributed to Cu-enrichment of $MgZn_2$ precipitates, which depleted the matrix of Cu.

The difference between T6 and T7-tempers on the distribution of pits in AA7075 was studied by Dey at al. [72] The T6-temper exhibited a higher number of smaller pits, pit density, and total pitted area compared to the T7-temper. Pitting in the T6-temper also appeared to not reach a saturation point with increased exposure time, while pitting in the T7-temper appeared to saturate. The difference in pit distributions between the two tempers was attributed to the difference in the volume fraction and size of $MgZn_2$

precipitates. The T6-temper resulted in smaller pits, an increased pit density, and total pitted area due to having an increased volume fraction and smaller precipitate size. However, the authors concluded that pitting is a result of the higher potential difference between the active $MgZn_2$ precipitates and the close proximity of less active Al_7Cu_2Fe and Al_3Fe particles, and not the potential difference between $MgZn_2$ precipitates and the matrix.

2.2.2 Intergranular Corrosion

Intergranular corrosion (IGC) is defined as the selective attack of grain boundary regions (PFZs) and/or grain boundary precipitates resulting from the aging of heat-treatable Al alloys [58]. The three major accepted theories of IGC, pertaining to AA7xxx alloys, are discussed within this section.

2.2.2.1 Galvanic Couple Theory

Galvanic couple theory was introduced by Dix et al. [77] while studying the Al-Cu system. The authors postulated that IGC is a result of a galvanic corrosion cell between the less active grain matrix and the active grain boundary region (either the PFZ or grain boundary precipitates). In an additional study, Brown and Mears [78] verified Dix et al.'s claims by isolating the grain matrix and the grain boundary region of Al-4%Cu and measuring their respective E_{corr} in a NaCl-H_2O_2 solution. The observed E_{corr} difference between the grain matrix and grain boundary region was +0.044 V SCE, with the grain boundary region being more active. In addition, transmission electron

microscopy (TEM) analysis of AA2024 (4.3Cu-1.5Mg) post corrosion exposure confirmed attack along the Cu-depleted PFZ, leaving behind unattacked grain boundary precipitates ($Al_2Cu(Mg)$) [79].

Dix et al. also examined IGC as observed in the Al-Zn-Mg system [80] using a similar approach to Brown and Mears [78]. Aside from isolating the grain boundary region, Dix et al. also measured the E_{corr} of $MgZn_2$ analogs. It was discovered that the difference in E_{corr} between the grain matrix and the grain boundary region was negligible. However, the E_{corr} difference between the grain boundary PFZ and the more active $MgZn_2$ was +0.020 V SCE. Dix et al. explained that IGC in the Al-Zn-Mg system was a result of a galvanic corrosion cell between the $MgZn_2$ grain boundary precipitates and the PFZ. On the contrary, Fink et al. [81] postulated that solute depletion (Cu,Mg,Zn) in the PFZ would make it more active to the grain matrix, much like what was observed in the Al-Cu system. Observation by TEM of AA7075-W, post exposure to NaCl-H_2O_2, confirmed Fink's hypothesis, revealing corrosion along the PFZ, and not the grain boundary precipitates [82]. It is possible, however, that the mechanism responsible for IGC in Al-Zn-Mg/AA7xxx alloys is dependent on the chemical composition and the thermal history of the alloy under study [83].

2.2.2.2 Breakdown Potential Model

IGC is not observed in environments that do not contain Cl^- ions [80], [81], [82]. Therefore, the shortcoming of the galvanic couple theory lies in its inability to explain the role of Cl^- ions in IGC. To account for this shortcoming, Galvele and De Micheli [84]

developed a theory to explain IGC based on the difference in E_{brk} of the PFZ and the grain matrix in an Al-4%Cu alloy. Two distinct E_{brk} were observed during potentiodynamic polarization in 1 M NaCl. Observations post potentiostatic polarization revealed the more active E_{brk} was associated with IGC and the less active E_{brk} was associated with IGC and pitting corrosion within the matrix.

Similarly, Maitra and English [85] studied AA7075 (6Zn-2.5Mg-1.7Cu) tempers (W, T651 and T751) in 0.6 M NaCl and also observed two distinct E_{brk}. Potentiodynamic polarization scans of the W-temper exhibited a single E_{brk} (at -800 mV SCE), below which minimal corrosion was observed and above which pitting of the matrix was observed. However, both of the artificially aged tempers, T651 and T751, revealed the presence of two E_{brk}. In the T651-temper, the more active E_{brk} (-800 mV SCE) correlated to IGC and the less active E_{brk} (-725 mV SCE) corresponded to pitting of the matrix. It was postulated that the more active E_{brk} associated with IGC was a result of solute (Mg and Zn) retention in the PFZ, compared to the lower solute concentration found in the grain interior as a result of $MgZn_2$ precipitation. Park and Ardell [41] have refuted this claim by showing the PFZ of AA7075-T6 to be depleted in Zn. The T751-temper revealed uniform corrosion at the more active E_{brk} (-800 mV SCE) and pitting of the matrix at the less active E_{brk} (-765 mV SCE). A reduction of the second E_{brk} of the T751-temper to more active values was reasoned to be a result of Cu-removal from solid solution to the η phase, in agreement with more recent studies [70].

Huang and Frankel [86] also studied the effect of various tempers (W, T6 and T7) on the localized corrosion of AA7075. Similar E_{brk} observations were made from the potentiodynamic scans of the W (-812 mV SCE) and T6-tempers (-796 and -758 mV SCE), however, only one E_{brk} (-753 mV SCE) was observed for the T7-temper. Potentiostatic tests at -725 mV SCE revealed pitting corrosion in the W-temper. Under the same potentiostatic conditions the T6 and T7-tempers exhibited corrosion that was limited to the dissolution of certain grains, termed selective grain corrosion [87], a result of Zn-retention in the grain matrix compared to the PFZ [12]. Similar selective grain dissolution was also observed during exfoliation corrosion testing of AA7178 (6.9Zn-2.8Mg-2.0Cu) [88].

Meng and Frankel [38] investigated the effect of Cu-content on the corrosion behaviour of five AA7xxx-T6 alloys: AA7004 (4.3Zn-1.6Mg), AA7039 (4.0Zn-2.9Mg-0.1Cu), AA7029 (4.6Zn-1.7Mg-0.7Cu), AA7075 (5.4Zn-2.4Mg-1.4Cu), and AA7050 (5.9Zn-2.0Mg-2.0Cu). Potentiodynamic polarization scans in deaerated 0.5 M NaCl revealed the presence of two E_{brk} for alloys containing Cu, except AA7004 (deemed essentially Cu-free), which displayed a single E_{brk}. Inspection of the AA7004 surface after potentiodynamic polarization revealed pitting, while the Cu-containing AA7xxx alloys displayed IGC and selective grain attack. TEM observation of AA7075-T6 after potentiostatic polarization tests, at potentials lower than the second E_{brk} but above the first breakdown potential, revealed dissolution of a thin surface layer. The two E_{brk} of the Cu-containing AA7xxx alloys increased with increasing Cu-content, appearing to decrease corrosion susceptibility. However, polarization resistance measurements in aerated 0.5 M

NaCl displayed quite the opposite. Cu-rich AA7xxx alloys displayed a decreased polarization resistance (increased corrosion susceptibility) compared to the Cu-lean alloys. Long term E_{corr} testing in aerated 0.5 M NaCl solution revealed differing behaviour between Cu-rich and Cu-lean alloys. For Cu-lean AA7004 and AA7039 Ecorr values started out close to the first and second breakdown potentials, respectively, but then decreased to very low values. OCP values of Cu-rich AA7029, AA7050, and AA7075 remained at values that were slightly higher than their own second E_{brk}. This contradicting behaviour was rationalized as a result of Cu-particle entry into the corrosion solution followed by adsorption/redistribution on the alloy surface. For Cu-rich AA7xxx alloys, Cu-particle adsorption would develop with time and facilitate O_2 reduction, driving the corrosion rate (as indicated by the observed polarization resistance decrease). Conversely, Cu-lean AA7xxx alloys would not permit Cu-particle redistribution on the alloy surface, resulting in the retardation of the cathodic reaction to sustain corrosion with time. This is shown by the observed OCP drop and increase in polarization resistance.

A subsequent study [89] focusing solely on the first E_{brk} of AA7075-T6 concluded that the attacked thin surface layer was a result of mechanical polishing. This layer contained high aspect-ratio nano-grains that displayed a high concentration of Mg and Zn at their boundaries, with very few $MgZn_2$ precipitates, as a result of elemental enrichment from material flow. Corrosion was believed to initiate at the solute-rich grain boundaries, which then led to the attack of the nano-grains. Non-mechanically polished samples only displayed a single E_{brk} leading to the conclusion that the first E_{brk} in Cu-containing AA7xxx alloys corresponds to the breakdown of the thin surface layer created by

mechanical polishing. This result negated the previous claims that the two observed E_{brk} in AA7xxx alloys were a consequence of the dissolution of two distinct phases or two different corrosion modes [38], [85], [86] .

2.2.2.3 Precipitate Dissolution Driven Occlude Environment

The final proposed IGC mechanism was presented by Buccheit et al. [90] and explains IGC as observed in AA2090 (3.0Cu-2.2Li). E_{corr} measurements revealed that the major precipitating T_1 phase (Al_2CuLi) was found to be more active (-1100 mV SCE) than the grain matrix (-720 mV SCE). Furthermore, pH measurements as a function of time were made during the corrosion of the T_1 phase and revealed a decrease in pH with increased exposure time. The authors postulated that the aggressive environment resulting from the dissolution of the T_1 phase on grain boundaries led to the autonomous attack along grain boundaries.

Ramgopla et al. [11] investigated the IGC behaviour of AA7150 (2.5Zn-4.5Mg-0.9Cu) in the T6 and T7-tempers. The T6-temper displayed two E_{brk} (-767 mV SCE and -711 mV SCE) while the T7-temper only showed one E_{brk} (-750 mV SCE). After potentiodynamic polarization, the T6-temper exhibited IGC and pitting, while the T7-temper only exhibited pitting. To further examine the IGC characteristics of AA7150, analogs of the grain matrix, PFZ, and $Mg(Zn, Cu, Al)_2$ grain boundary precipitates were used for electrochemical testing. The grain boundary precipitates of the T6-temper displayed a more active E_{brk} than those of the T7-temper, due to low Cu-content from peak-aging. The authors contend that the dissolution of precipitates of differing chemistry

resulted in differing environments, due to non-faradaic liberation of Cu^{2+} ions into solution [76], [75], under which IGC took place. Potentiodynamic polarizations scans of the PFZ and matrix were performed in 2 M NaCl solutions with various concentrations (0.01 M, 0.1 M and 0.3 M) of Cu^{2+} ions. The solutions with the two lowest Cu^{2+} concentrations, believed to mimic T6 solution conditions, displayed the E_{corr} of the PFZ to be more active than the grain matrix by approximately +60 mV SCE. In the solution of highest Cu^{2+} concentration, mimicking T7 solution conditions, little difference in the E_{corr} values was observed between the PFZ and grain matrix. This led to the conclusion that the T7-temper was less susceptible to IGC than the T6-temper due to the increased concentration on Cu^{2+} ions liberated into solution.

2.2.3 Exfoliation Corrosion

Exfoliation corrosion is a specific type of IGC that is typically observed in Al alloys with a high grain aspect ratio and directionality [58], with severity increasing with increased aspect ratio [5]. The physical appearance is characterized by a leafed/lamellar structure of alternating corroded and uncorroded material. The widely accepted reasoning behind the leafed appearance is a wedging stress that is perpendicular to the processing direction [6]. This arises from the creation of corrosion product along active grain boundary corrosion paths, parallel to the processing direction and whose volume exceeds the metal from which it formed [6], separating the layers of uncorroded material. The corrosion product is believed to be a hydrated aluminum oxide $Al(OH)_3$ with a variable water content, either gibbsite or bayerite whose specific volumes are 6.44 and 6.14 times

greater than Al, respectively [6]. These wedging stresses lift the surface grains and promote further attack.

The propagation of exfoliation corrosion has been linked to a stress-assisted mechanism, although it was initially believed to propagate via an autonomous electrochemical mechanism (consumption of matter along a continuous path) [6], [91]. Wedging force measurements done on Alloy L95 (5.8Zn-2.5Mg-1.6Cu), exposed to the ASTM-G34 solution, using a special jig [91] revealed that an exfoliated surface can exert a force of 600-800 N. Double cantilever beam and crack opening displacement measurements were subsequently utilized to establish and compare stress-corrosion intensity (K_{ISCC}) and stress intensity (K_1) factors. Comparable K_{ISCC} and K_1 values (2.6 and 2.9 $MNm^{-3/2}$) suggested that wedging forces are required for stress-assisted propagation. Similar studies [92] of AA7150 (5.9Zn-3.5Mg-1.7Cu), AA7055 (6.6Zn-3.0Mg-1.9Cu), and AA7449 (7.7Zn-3.5Mg-1.9Cu) show an inverse, linear relationship between wedging force and K_{ISCC}, which provide more evidence that exfoliation is propagated by a stress-assisted mechanism. More recent explorations [93], [94] into the exfoliation corrosion of AA7449 (8.5Zn-2.2Mg-1.9Cu) and AA7150 (6.4Zn-2.3Mg-2.2Cu) revealed the presence of a protruding surface blister before the observance of an exfoliated surface. SEM investigation of the exfoliation crack tip revealed no corrosion product. The authors suggest a hydrogen-assisted propagation mechanism, in which the elemental hydrogen produced at the cathode (PFZ) is absorbed into the material where it recombines into H_2. The absorbed H_2 embrittles the material leading to intergranular decohesion.

Like IGC, exfoliation is believed to be a result of a galvanic couple between the grain boundary region and the grain matrix, but there is no consensus on what specific parts of the grain boundary causes exfoliation. The most accepted explanations for exfoliation corrosion in Cu-containing AA7xxx are either a galvanic couple between the η phase grain boundary precipitates and the adjacent solute (Cu, Mg, Zn) depleted PFZ [94], [6], [7], or a galvanic couple between the solute depleted PFZ and the interior grain matrix [95]. However, in Cu-free AA7xxx alloys, exfoliation has been found to be both intergranular and transgranular [96], [97]. Electrochemical observation [96] of the phases present in naturally aged Al-5Zn-1Mg show that Al(Fe, Mn)Si particles acted as cathodes (E_{corr} ranging between -385 - (-430) mV SCE) and the saturated solid solution acted as the anode (E_{corr} = -970 mV SCE). The cathodic Al(Fe, Mn)Si particles were aligned in streaks parallel to the working direction with narrow zones of the attacked (anodic) saturated solid solution between, displaying a transgranular exfoliation mode. Acetic acid-salt spray tests conducted on AA7004 (4.3Zn-1.8Mg) [97] with varying amounts of Fe, Mn, and Si showed that only samples with Mn exhibited exfoliation, which was both intergranular and transgranular. Transgranular corrosion was observed between elongated intermetallic particles that were aligned during rolling. Electron probe scans of the attacked intergranular region revealed a depletion of Mn across the grain boundary. Similarly, scans of the transgranular attacked region revealed unattacked intermetallic particles rich in Al, Fe, and Mn with Mn-depletion around the intermetallic corresponding to the attacked region. This led to the conclusion that a galvanic couple between Mn-

depleted and Mn-rich regions existed at both grain boundaries and grain interiors, which led to the development of exfoliation.

Heat treatment of the AA7xxx alloy affects exfoliation corrosion. It has been demonstrated in numerous studies [93], [94], [98], [8] that the over-aged T7-temper has improved resistance to exfoliation corrosion compared to the peak-aged T6-temper in Cu-containing AA7xxx. It is believed that over-aging hinders exfoliation corrosion in the following ways:

1) Coarsening of grain boundary precipitates, which creates a non-continuous corrosion path that slows the propagation of exfoliation [10].
2) Enrichment of grain boundary precipitates in Cu, which drives the E_{corr} of the precipitates in the cathodic direction, thus, making them less susceptible to corrosion [94].
3) Even solute distribution between the PFZ and the grain matrix, which reduces the electrochemical potential difference between the two microstructural regions [83].

However, a study [7] of the exfoliation corrosion of AA7010 (6.2Zn-2.2Mg-1.5Cu) and AA7349 (7.6Zn-2.3Mg-1.5Cu) adhering to the ASTM-G34 standard, displayed no difference in the exfoliation corrosion rating between T6 and T7-tempers of these alloys. No effort was made to determine the physiochemical differences between the temper's' microstructures.

According to Matteson et al. [96] the corrosion mode, in Cu-free AA7xxx, changes from the naturally-aged temper to the artificially-aged temper. In the naturally-aged condition, exfoliation results from a galvanic couple between Al(Fe, Mn)Si particles that are aligned parallel to the working direction and narrow zones of anodic saturated solid solution between. In the artificially-aged temper, the Al(Fe, Mn)Si particles remain as cathodes, but the η phase precipitates within the grain matrix form anodes which lead to uniform pitting not exfoliation.

2.3 Properties and Microstructure of Welded AA7xxx Alloys

In order to understand the effects of welding on the corrosion behaviour of any metal/alloy, in this particular instance AA7xxx, it is important to understand the microstructural and compositional changes that arise from welding within the weld region. A typical weld region, as shown in Figure 3, is composed of several distinct macroscopic regions that undergo metallurgical changes as a result of the thermal cycling from welding: the fusion zone, the unmixed region, the partially melted region, the HAZ, and the unaffected base alloy [99]. The fusion zone consists of solidified filler material, which is typically different than the base metal and whose microstructure is primarily influenced by the solidification behaviour of the weld pool [100]. The area adjacent to the fusion zone is the unmixed region, where the base metal has experienced melting, but has not mechanically mixed with the melted filler alloy [99]. The partially melted region follows the unmixed region, and in AA7xxx alloys this zone is often referred to as the "white zone" due to its etching appearance in nitric acid [101].

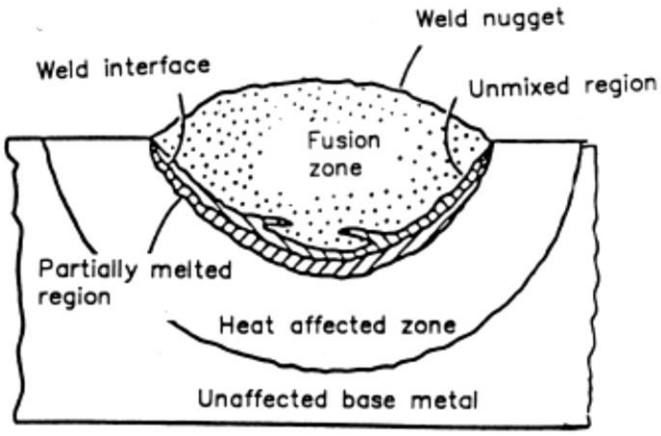

Figure 3: Distinct regions found in a typical weld zone **[99]**

The white zone is characterized by local melting (liquation) at grain boundaries. This embrittles the grain boundaries, which leads to intergranular cracks known as liquation cracks [102]. The white zone is followed by the HAZ, which experiences temperatures that cause solid-state microstructural changes without any melting. Within AA7xxx alloys, pre-existing precipitates in the HAZ can be modified in such ways as: dissolution and/or coarsening of precipitates and phase-stability transformations [103], [104]. Due to the unique metallurgical condition of each of the five previously mentioned regions, each region possesses differing properties from the others. For the purpose of this study interest only lies in the HAZ. Therefore, a more detailed look at the properties of the HAZ of welded AA7xxx is presented in the two subsequent sections.

2.3.1 Microstructure and Properties of the HAZ

Welding has a deleterious effect on the properties of precipitate-hardening Al alloys (AA2xxx, AA6xxx, and AA7xxx) in the HAZ region adjacent to the fusion zone.

This is a result of the high heat input from the welding process. The HAZ of precipitate-hardening Al alloys is most commonly characterized by a softened region that is observed in the hardness profile, as shown in Figure 4 a.

An investigation on modelling of AA7108 –T6 (5.5Zn-.85Mg-0.05Cu) welds by Myher et al. [105] showed that a steep drop in hardness occurred when the peak temperature within the HAZ reached 200-340°C, as demonstrated in Figure 4 a. This temperature range corresponded to the dissolution of η' precipitates and growth of the η phase. Beyond 340°C, complete dissolution of the η phase was believed to occur. The authors concluded that the steep drop in the HAZ hardness for AA7108 welds was a consequence of the poor thermal stability of the η and η' precipitates. This poor thermal stability at higher temperatures leads to extensive GP-zone formation upon cooling and natural aging. This leads to very efficient recovery of hardness within the HAZ after 3-5 months of natural aging. The hardness profile showing hardness recovery after contributions from natural aging is indicated by the dashed line in Figure 4 b. Similarly, Nicolas [103] showed that the HAZ of AA7108.05 (5Zn-0.8Mg) can recover 90% of its hardness in 110 days within the complete dissolution region.

In a complimentary study on the prediction of HAZ properties of AA7108-T6 (5.5Zn-.85Mg-0.05Cu) welds done by Bjorneklett et al. [106], they successfully modeled the aging behavior of the HAZ. The authors postulated that between the fully reverted region of the HAZ and the adjacent unaffected base alloy, a Zn and Mg solute concentration gradient exists as a result of the precipitate modifications.

Investigations into the softening and recovery of the HAZ of welded AA7020-T6 (4.3Zn-1.2Mg-0.1Cu) and AA7005-T6 (4.5Zn-1.4Mg-0.1>Cu) were respectively conducted by Ma et al. [104] and Fu et al. [107]. To investigate HAZ softening, the studies correlated HAZ peak temperatures and TEM micrographs. Both studies split the HAZ into two zones: the dissolution zone and the overaging zone. The dissolution zone corresponds to the area immediately adjacent to the fusion zone and is characterized by precipitate dissolution, whose hardness is recoverable to levels that of the unaffected base alloy by subsequent aging. The overaging zone lies between the dissolution zone and unaffected base alloy and is characterized by precipitate coarsening. Hardness in this region is not recoverable to the levels of the unaffected base alloy by natural aging. The overaging zone is typically seen as a dip or valley in hardness profiles after aging.

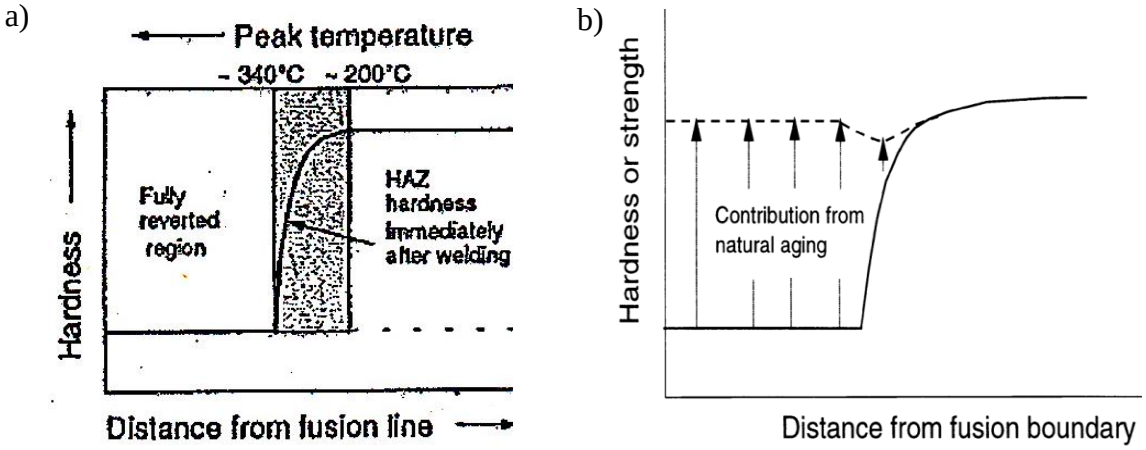

Figure 4: HAZ hardness profile for welded AA7108-T6 a) immediately after welding **[105]** b) after 3-5 months of natural aging **[106]**.

The dissolution zone corresponded to HAZ peak temperatures greater than 390 °C and 380 °C, respectively, for AA7020-T6 and AA7005-T6. The overaged zone was found

in HAZ peak temperatures of 210-390 °C for AA7020-T6 and 230-280 °C for AA7005-T6. Moreover, the studies investigated the recovery of the HAZ after the application of 3 post-weld heat-treatments: natural aging at room temperature (3 months for AA7020-T6 and 4 months for AA 7005-T6), artificial aging for 24 h at 120 °C and step aging (8 h at 100 °C + 16 h at 145 °C for AA7020-T6 and 8 h at 100 °C + 24 h at 150 °C for AA7005-T6). Both studies concluded artificial aging had the best recovery of the HAZ. The degrees of recovery from each heat-treatment for AA7005-T6 are shown in Figure 5; similar observations were made about AA7020-T6.

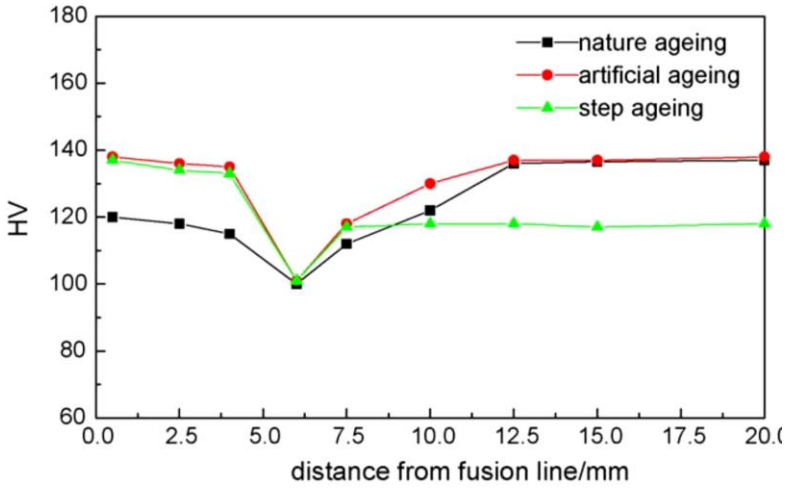

Figure 5: Modifications observed in the HAZ of welded AA7005-T6 after the application of various post-weld heat-treatments **[107]**

Nicolas [103] conducted in-depth analysis of welded AA7108.50 HAZ in various tempers (T4, T6 and T7); data pertaining to the T6-temper is only discussed here. The studies linked TEM, SAXS (Small Angle X-ray Scattering) and DSC (Differential Scanning Calorimetry) data. SAXS provided information regarding the size (R) and

volume fraction (Fv) of precipitates within the HAZ as a function of distance away from the fusion line, shown in Figure 6. From the microhardness plot of Figure 6 it is clear that a transition zone between the unaffected base alloy and the dissolution region lies in a temperature range of 155-245 °C. This transition zone was defined by a decrease in the Fv of precipitates until the dissolution region was reached. However, only at a HAZ peak temperature range of 220-245 °C did the transition zone precipitates coarsen, while the rest of the zone's precipitate size remained constant. This is contrary to the findings of Ma et al. [104] and Fu et al. [107] who claimed this entire transition zone or overaging zone was defined by precipitate coarsening.

DSC was used to further investigate the nature of the precipitate modifications occurring in the HAZ, more specifically, any phase changes (η' to η) observed in the transition zone between the peak temperatures of 220-245 °C. DSC scans of a AA7108.50-T6 HAZ sample 20 mm away from the fusion line and an unaffected AA7108.50 base alloy in the T6 and T7-temper were compared. Both the HAZ and unaffected base alloy scans in the T6-temper showed endothermic peaks around 250 °C, which corresponded to the dissolution of η' precipitates. A lowered dH/dT response of the HAZ sample was observed as a consequence of the lowered Fv of precipitates observed at 20 mm from the fusion line in the HAZ. It was concluded that the HAZ consisted of 3 zones: the fully reverted/solutionized zone (HAZ peak temperatures greater than 245 °C), a η' phase dissolution and coarsening zone (HAZ peak temperature range 220-245 °C), and a η' phase dissolution zone (HAZ peak temperature range 220-155°C).

Nicolas also observed grain boundary precipitates in the HAZ and concluded that grain boundary precipitates (η phase precipitates) did not undergo major modifications when HAZ peak temperatures did not exceed 300 °C (12 mm or further from the fusion line). Temperatures above 300 °C resulted in the dissolution of grain boundary η precipitates. TEM examination of grain boundaries at 5 mm (HAZ peak temperature of ≈ 450 °C) away from the fusion line showed no grain boundary precipitation, while grain boundaries at 14 mm and 17 mm (250-300 °C) away from the fusion line appeared unaltered when compared to the unaffected base alloy.

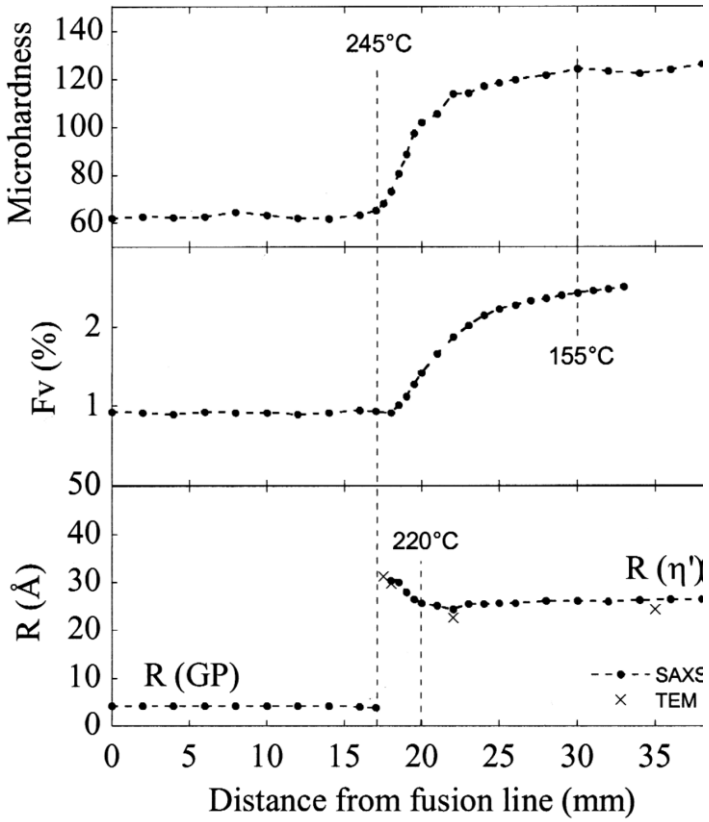

Figure 6: AA7108.50-T6 HAZ characterization using microhardness (top), precipitate volume fraction (middle) and precipitate radius (bottom) **[103]**.

Hwang et al. [108] studied the nature of precipitates in the HAZ of AA7075-T651 (6.0Zn-2.5Mg-1.7Cu) at HAZ peak temperatures of 237 °C, 288 °C, 377 °C, 445 °C, and 546 °C using TEM and DSC. Initially the unaffected base alloy of AA7075-T651 contained η' precipitates. However, at peak temperatures of 237 °C and 288 °C DSC thermographs displayed dissolution peaks of both η' and η precipitates, with an increased response of η precipitates observed at 288 °C. Peak temperatures of 377 °C yielded only the presence of a η precipitate dissolution peak. Finally, at 546 °C two dissolution peaks were observed that were a consequence of GP-zone and η precipitate dissolution. The dissolution peak corresponding to the dissolution of η precipitates was less pronounced than that observed at 288 °C and 377 °C.

2.3.2 Corrosion of Welded AA7xxx Alloys

As shown by the previous section, welding has a profound effect on the microstructure and properties of the HAZ of welded AA7xxx. However, a consensus has not yet been obtained as to what this effect is. Welding affects corrosion behaviour as a consequence of microstructural changes in the HAZ. However, the topic has seldom been studied, and very little attempt has been made to approach the issue with great detail, unlike the corrosion behaviour of non-welded AA7xxx. A summary of studies into the corrosion of welded AA7xxx is provided below.

Early studies [109] on the corrosion of welded AA7xxx were conducted by ALCOA Laboratories (Pittsburgh, Pennsylvania, USA) and focused on the corrosion of AA7005 (4.5Zn-1.3Mg-0.1Cu) welded with ER5356 (~5Mg) filler after exposure to

seawater for one year. Corrosion in the as-welded condition was localized to the HAZ adjacent to the weld, as shown in Figure 7 a. No size quantification for this region was provided. E_{corr} values of the different weld zones (weld, HAZ, and unaffected base alloy) were measured in a solution of NaCl + H_2O_2. The measurements revealed that the HAZ was more anodic than the weld and the unaffected base alloy. E_{corr} values are indicated in Figure 7. No explanation was provided as to why the HAZ was more anodic compared to the other weld zones. Furthermore, the studies also examined the effect of a post-weld heat-treatment on the corrosion of the AA7005 weld. Heat-treatment details were not provided. No corrosion was observed after one year of seawater exposure and E_{corr} measurement of the HAZ and the unaffected base alloy showed no difference between the two weld zones, shown in Figure 7 b.

Similarly, ALCOA [109] investigated the corrosion behaviour of AA7039-T651 (4.0Zn-3.0Mg-0.08Cu), two-pass welded with ER5183 (~4.7Mg) filler. E_{corr} scans as a function of distance away from the weld centerline, in a NaCl + H_2O_2 solution, were created. They revealed the presence of a small region, immediately adjacent to the weld that was highly anodic with respect to the rest of the AA7039-T651 HAZ, as shown in Figure 8. Progression away from the anodic region yielded an increase in E_{corr} to values that of the unaffected base alloy. No explanation for this behaviour was provided.

Enjo and Kuroda [110] investigated the effect of minor (.17 wt%) Cu additions on the corrosion resistance of two Al-Zn-Mg alloys welded with ER5356 in the T5-temper: alloy A (4.5Zn-1.2Mg) and alloy B (4.5Zn-1.1Mg-0.17Cu).

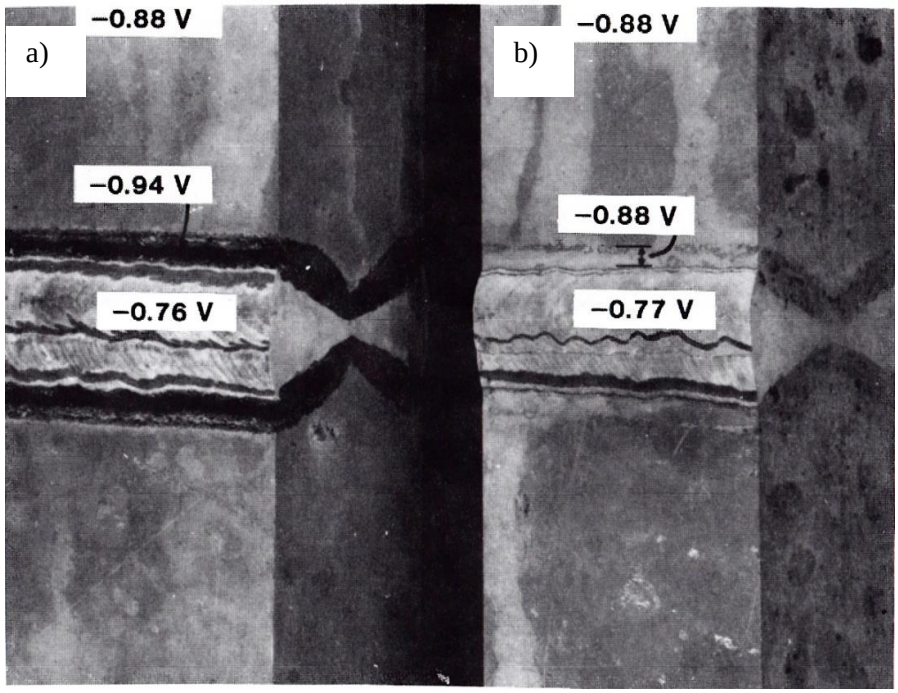

Figure 7: AA7005 welded with ER5356 post exposure to sewater (one year) in a) the as-welded condition and b) post-weld heat-treated condition. All E_{corr} values are referenced against an SCE **[109]**.

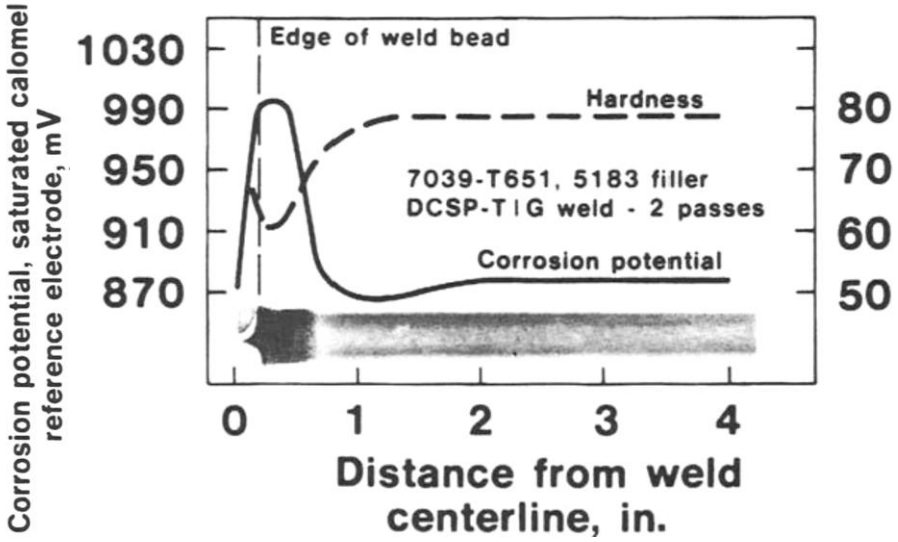

Figure 8: E_{corr} scans as a function of distance away from the fusion line of AA7039-T651, double pass welded with ER 5183 filler **[109]**.

Anodic potentiodynamic polarization scans were carried out in a 1 M NaCl solution, which was deaerated with Ar for 30 min prior to testing. Researchers focused their attention on the area immediately adjacent to the weld. Polarization scans revealed the presence of a single E_{brk} in both alloys. The alloy with less Cu (alloy A) possessed a more anodic E_{brk} at -1000 mV SCE, while the alloy richer in Cu (alloy B) had a less anodic E_{brk} at -900 mV SCE. However, no differences were observed in the E_{corr} of the two alloys. Interestingly, the E_{brk} of the unaffected base alloy of both alloys was observed at -900 mV SCE. A 20 mV SCE Ecorr difference was observed between both unaffected base alloys.

Kuroda et al. [111] investigated the corrosion characteristics of TIG welded 7N01-T6 (4.6Zn-1.2Mg). Anodic potentiodynamic polarization scans were carried out in a 1 M NaCl solution that was deaerated with Ar for 30 min prior to testing. Pitting potentials were then plotted as a function of distance away from the fusion line, as demonstrated in Figure 9. The plot of pitting potential as a function of distance from the weld was broken down into three regions. Region A is characterized by the lowest observed pitting potential, a result of a high solid-solution solute (Zn and Mg) concentration from the complete dissolution of precipitates. An increase in the pitting potential of region A close to the weld was believed to be a result of the dissolution of $Al_{18}Cr_2Mg_8$, resulting in an increase of Cr in solid-solution at the fusion line. Region B1 is denoted by an observed increase in the pitting potential. This is a result of the decreasing solid- solution solute concentration from the partial dissolution of precipitates. Finally, Region B2 was

characterized by a steady pitting potential, typical of the unaffected base alloy, resulting from a smaller solid-solution solute concentration due to a larger number of precipitates.

Wang at al. [112] investigated the corrosion of 7N01-T4 (4.5-5.0Zn-1.0-2.0Mg-0.2>Cu) welded with ER5356 (4.5-5.5Mg) filler. Samples were studied under salt fog exposure to a 0.9 M NaCl solution with $CuCl_2$ additions for 72 h. Pitting and intergranular corrosion was observed in the HAZ. More pits were observed in the HAZ compared to the unaffected base alloy, maximum pit depths in the HAZ were measured at 34.5 µm. Only a handful of pits were observed in the weld with maximum pit depths of 6.5 µm. They proposed that a macroscopic galvanic corrosion cell existed between the less active weld, rich in Al_8Mg_5 phase, and the more active HAZ of 7N01-T6, rich in η phase. Both pitting and intergranular corrosion were observed because $MgZn_2$ precipitates were found both in the grain interior and along grain boundaries.

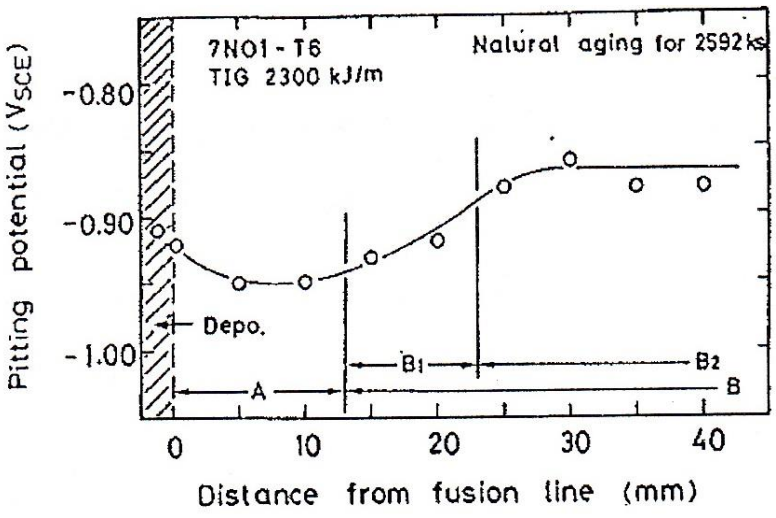

Figure 9: Pitting potential as a function of distance away from the fusion line of TIG welded 7N01-T6 **[111]**

Onoro et al. [113] investigated the effects of different heat-treatments (as-received, T4, T6, and T6*- a shortened T6-heat treatment) prior to welding on the exfoliation corrosion behaviour of AA7015 (4.7Zn-1.9Mg-0.2Cu) welded with an ER5183 (4.6Mg) filler. Exfoliation corrosion behaviour was assessed according to the ASTM G-34 EXCO test. A summary of the EXCO test results is given in Table 2. Results showed only slightly more severe corrosion rating in the HAZ of each heat-treated sample compared to the unaffected base alloy. The biggest difference was observed in welded AA7015-T6*. Corrosion potentials of the weld and successive strips across the HAZ were measured until the unaffected base alloy was reached. Measurements were made in a solution of NaCl + H_2O_2. Results of the E_{corr} measurements yielded very little variation (<10 mV SCE) across the HAZ and into the unaffected base alloy. This is consistent with EXCO testing that showed little variation in the degree of exfoliation severity between the HAZ and unaffected base alloy.

Table 2 ASTM G34 results for various heat-treated welded AA7015 alloys. * denotes a two-step T6 heat-treatment was applied **[113]**.

	Base alloy	**HAZ**
7015-M	EB (moderate)	EC (severe)
7015-T4	EB (moderate)	EB (moderate)
7015-T6	EA (superficial)	EB (moderate)
7015-T6*	EA (superficial)	EC (severe)

3.0 Experimental Details

3.1 AA7xxx Weld Joints

All weld joints under investigation in this study have been prepared from extruded bumper beams of AA7003 (Al-Zn-Mg), AA7108 (Al-Zn-Mg), and bracket components of AA6063 (Al-Mg-Si). Weld joints were metal inert gas (MIG) welded in two joint geometries, lap-joints and T-joints, according to the procedures specified in the General Motors (GM) Global Weld Design Standard "GWS- 1C, Section C: Arc Brazing & Arc Welding". Specific details and parameters pertaining to the welding of the bumper assemblies were not provided. Two different filler alloys, ER4043 (Al-Si) and ER5356 (Al-Mg), were used to fuse the bumper beams and bracket components. Figure 10 and 11 show, respectively, typical lap-joint and T-joint samples labeled with major dimensions. Figures 10 b and 11 b also show three orthogonal directions used to indicate cross-sectional planes: the L (Longitudinal) direction (which is parallel to the extrusion direction), the LT (Longitudinal Transverse) direction, and the ST (Short Transverse) direction.

Chemical compositions of the AA7003 and AA7108 alloys were determined using Inductively Coupled Plasma Optical Emission Spectroscopy (ICP-OES). 1 cm^2 samples were cut from each base alloy and cleaned using ethanol (C_2H_6O) wipes. Each 1 cm^2 alloy sample was then drilled, and 0.1 g of the drill shavings was used for analysis.

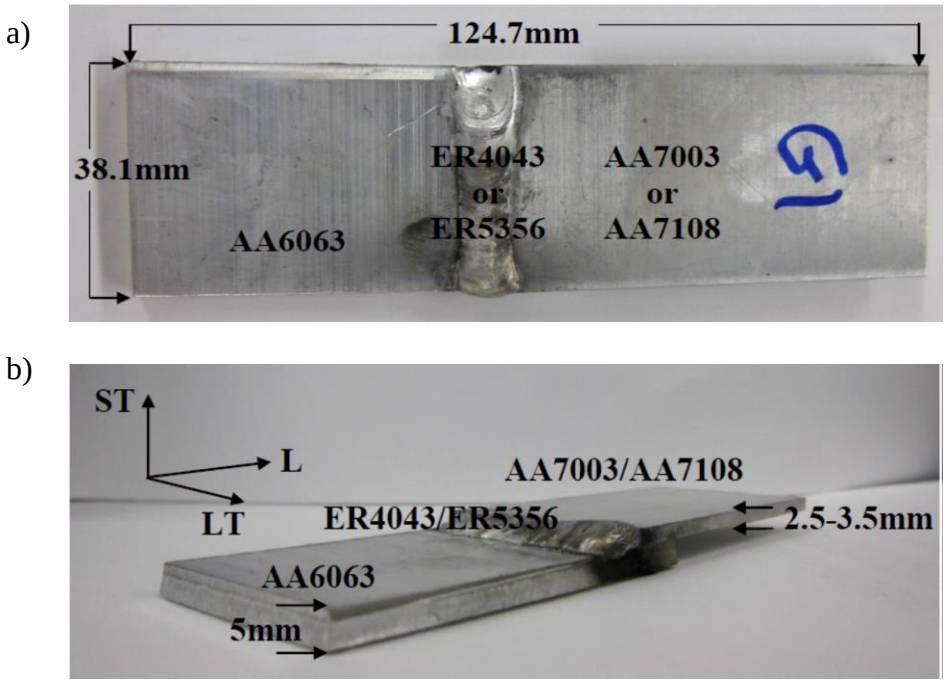

Figure 10: Welded AA7xxx lap-joint configuration with all major dimension as seen from (a) the top view and (b) side view. Figure 10 b indicates three orthogonal directions used to identify cross-sectional planes.

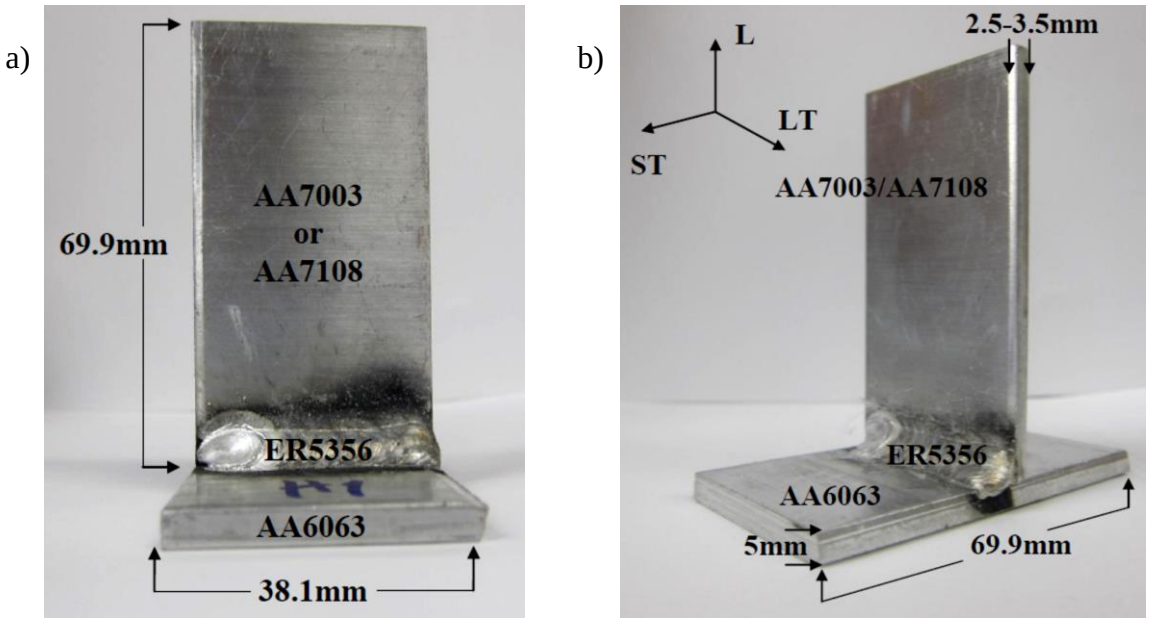

Figure 11: Welded AA7xxx T-joint configuration with all major dimension as seen from (a) the front view and (b) side view. Figure 3.1 b indicates three orthogonal directions used to identify cross-sectional planes.

The 0.1 g samples were then dissolved in 2 ml of borofluoric acid (H_3BF_4, 40 wt%), which was prepared by mixing 38 g of boric acid (H_3BO_4) in 100 ml of hydrofluoric acid (HF, 40 wt%). The samples were then mixed with 3 ml of hydrochloric acid (HCl, 37 wt %) and 10 ml of distilled water (H_2O). The metal-acid solution was then heated over a hot plate at 100°C for approximately 1 h or until the samples were completely digested. The 15 ml solution was then diluted with distilled H_2O to a total volume of 100 ml prior to analysis. Three 0.1 g samples were used for each alloy, and the average was recorded for each observed element. Table 3 shows the results of the average chemical compositions of AA7003 and AA7108 as determined by ICP-OES. Also included in Table 3 are the nominal compositions of AA6082, ER4043, and ER5356, which were not analyzed using ICP-OES. All nominal compositions are as specified by The Aluminum Association [99] and are indicated by an asterisk (*).

Table 3: ICP-OES determined and nominal compositions of various alloys used in the AA7xxx weld joints. Nominal compositions are indicated by an asterisk (*). All compositions are shown in wt%.

Alloy	**Si**	**Fe**	**Cu**	**Mn**	**Mg**	**Cr**	**Zn**	**Zr**	**Ti**
AA7003	0.09	0.16	0.14	0.11	0.94	0.06	6.2	0.16	---
AA7108	0.07	0.17	0.01	---	1.3	---	5.7	0.13	---
AA6063*	0.20-0.60	0.35	0.10	0.10	0.45-0.90	0.10	0.10	---	0.10
ER4043*	4.5-6.0	0.80	0.30	0.05	0.05	---	0.10	---	0.20
ER5356*	0.25	0.40	0.10	0.05-0.20	4.5-5.5	0.05-0.20	0.10	---	0.06-0.20

From Table 3 it is evident that AA7003 is richer in alloying elements Cu and Zn compared to AA7108, while AA7108 is richer in Mg. Both AA7xxx alloys contain similar levels of impurity elements and include Zr as a grain refining element.

Weld joints were examined in two heat-treated conditions, the as-welded T6 condition and the as-welded T6+ (PB) condition. The T6 heat treatment, involving a 3-step heat treatment, was applied prior to welding. First the extrusions were solutionized for 45 min at temperatures of 485-500°C, which was followed by water quenching. The subsequent steps involved aging the extrusions at 92°C for 4 h, followed by a final aging step at 142°C for 12 h. The as-welded T6+PB condition consisted of the aforementioned T6 heat-treatment prior to welding, followed by a subsequent post-weld paint-bake which consisted of heating the weld joints to 185°C for 50 min. This was followed by air-cooling to room temperature for 20 min, and then baking the weld joints a second time at 185°C for 50 min, followed by a final air-cooling to room temperature.

For this investigation eight sets of weld joints in fifteen different configurations were provided by GM Canada Limited for examination. The major variables under study include the heat-treated condition (as-welded T6 vs. as-welded T6+PB), extruded beam alloy Cu composition (AA7003 vs. AA7108), weld filler composition (ER4043 vs. ER5356), weld joint geometry (lap-joint vs. T-joint), and weld direction with respect to extrusion direction (parallel (═) vs. perpendicular (⊥)). Table 4 summarizes these details. Weld configurations in the as-welded T6 condition were denoted by a “1”, the as-welded T6+PB condition was denoted by a “3”.

Table 4: AA7003 and AA7108 Weld Joint Configurations

Configuration	Bumper Alloy	Weld Filler	Weld Geometry	Weld Orientation[1]	Heat Treatment
A1	AA7003	ER5356	Lap-joint	Perpendicular (⊥)	as-welded
A3					T6+PB
C1	AA7108	ER5356	Lap-joint	Perpendicular (⊥)	as-welded
C3					T6+PB
D3	AA7003	ER4043	Lap-joint	Perpendicular (⊥)	as-welded T6+PB
E1	AA7003	ER5356	T-joint	Perpendicular (⊥)	as-welded
E3					T6+PB
F1	AA7108	ER5356	T-joint	Perpendicular (⊥)	as-welded
F3					T6+PB
G1	AA7003	ER5356	Lap-joint	Parallel (═)	as-welded
G3					T6+PB
H1	AA7003	ER5356	T-joint	Parallel (═)	as-welded
H3					T6+PB
I1	AA7108	ER5356	Lap-joint	Parallel (═)	as-welded
I3					T6+PB

[1] Relative to extrusion direction

Due to production capability limitations, GM Canada Limited was unable to provide weld joint configuration D1 for this investigation, which accounts for its omission in Table 4.

3.2 Weld Joint Characterization

One weld joint from each of the fifteen different configurations (Table 4) was utilized for metallographic characterization. Each weld joint was cross-sectioned perpendicular to the weld, along the center-line of the weld assembly using a high-speed cut saw. The halved weld joint was further reduced in size to fit a 3.8 cm diameter mould. Each cut weld joint was then cold-mounted using an epoxy resin.

Once properly cured, the cold-mounted cross-sections were polished with the aid of an automatic polisher (Struers Rotopol-31). Cross-sections were first wet-ground with 1200 grit and finally with 4000 grit silicon carbide (SiC) paper using water as lubricant. Cross-sections were then sequentially polished first to a 3 μm finish and then to a 1 μm finish using polishing clothes and diamond suspension. The final polishing step, a 0.05 μm finish, was accomplished by using a neoprene cloth with a solution consisting of 100 ml of colloidal silica and 10 ml of hydrogen peroxide (H_2O_2). The polished cross-sections were then etched to reveal their respective microstructure. Etching involved immersing the samples in Keller's Reagent, which consisted of 95 ml distilled H_2O, 2.5 ml of nitric acid (HNO_3, 70 wt%), 1.5 ml of HCl (37 wt.%), and 1 ml of HF (45 wt.%), for 15-30 s.

Each etched cross-section was then observed under a light optical microscope (Nikon Eclipse 100LV) to document the microstructural features of the weld, HAZ, and unaffected base alloy. Grain size measurements were done with the assistance of image analysis software (NIS Elements Basic Research (BR)). All grain size measurements

completed with the software were done in accordance with the procedures specified in ASTM E112 “Standard Test Methods for Determining Average Grain Size” [114].

Microhardness measurements were completed on the mounted as-polished cross-sectioned weld joints using a micro-indenter (Clemex CMT-HD). Measurements were made using a 100-g load with a 10 second dwell time. Three measurements were taken every 1 mm apart as a function of distance from the weld center. Measurements were made 150 μm above, 150 μm below, and along the center-line of the AA7xxx extrusion. For welded T-joint configurations, measurements were first recorded moving horizontally from the weld center until the center-line of the vertical AA7xxx extrusion was reached. Once the extrusion center-line was reached, measurements were made vertically. Figures 12 a) and b) show, respectively, the microhardness measurement paths taken on welded lap-joint and T-joint configurations. Error bars on each data point were calculated to a 95% confidence interval (CI) based on 3 measurements taken at each millimeter away from the fusion line, for a total of 20 mm.

a) b)

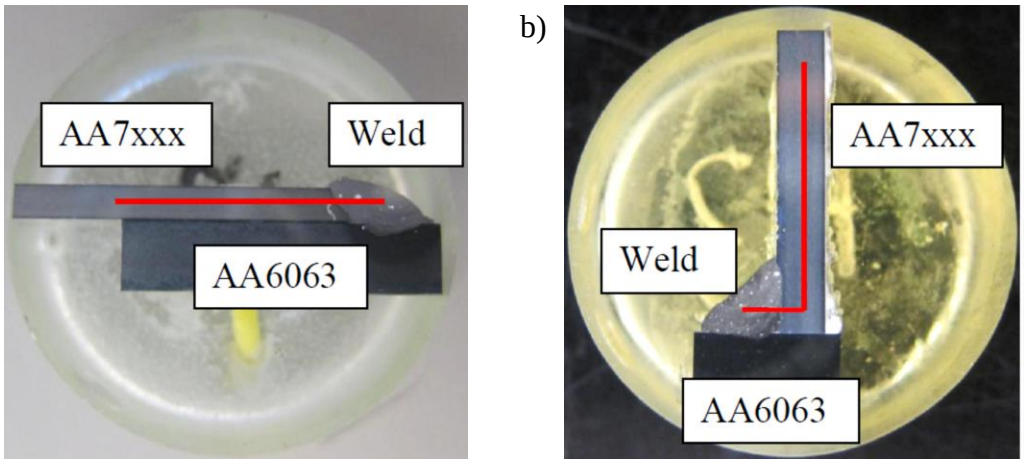

Figure 12: Red line indicating microhardness measurement paths taken on welded AA7xxx (a) lap-joint and (b) T-joint configurations.

3.3 Standardized Corrosion Testing

3.3.1 ASTM G85-A2

To examine the exfoliation corrosion behaviour of each weld joint configuration (Table 4) in an aggressive environment, exposure according to ASTM G85 "Standard Practice for Modified Salt Spray (Fog) Testing" [115] was conducted. The essential details are summarized below.

Duplicates from each weld joint configuration were used for this experiment. Weld joints were exposed in the as-received condition with no surface preparation prior to exposure. Only the front face of the weld joints was directly exposed to the test solution, all other faces (back and sides) were masked off using a silicone coating. Prior to exposure, all weld joint configurations were degreased using an acetone ($(CH_3)_2CO$) wipe, ultrasonically immersed in C_2H_6O for 5 min, and dried under a hot air stream. All coated and cleaned weld joint configurations were photographed prior to exposure.

The adopted procedure involved exposing the duplicates to an acidified cyclic salt fog in a corrosion chamber (Asscot CC450xp) for a period of 6 weeks or 168 cycles. Each cycle lasted 6 h and consisted of three stages, a 0.75 h salt fog stage, a 2 h dry-air purge stage, and a final 3.25 h soak at relative high humidity (95-100% humidity). Each cycle was maintained at a temperature of 49°C.

The initial test solution was prepared in an inert plastic 80 L container by dissolving 53 g of sodium chloride (NaCl) for every liter of distilled H_2O, 2 ml of acetic

acid (CH_3CO_2H) was added for every liter of distilled H_2O to maintain the pH of the solution between 2.8-2.9. The test solution in the 80 L container was stirred once a day for the duration of the test to keep the solution thoroughly mixed. Fresh solution was added as needed in 4 L batches to maintain solution levels in the 80 L container to avoid air suction into the atomizer.

Weld joint configurations were supported using slotted inert plastic racks held horizontally (the weld vertical and facing the atomizer) at an angle of 20° from the vertical with a minimum spacing of 5 cm between each sample. The atomizer was positioned at an angle of 30° from the vertical at the front of the corrosion chamber. Weld joint configurations were exposed in 2 separate batches, lap-joints and T-joints, due to rack size limitations. A schematic of the lap-joint and T-joint rack lay-outs are depicted, respectively, in Figure 13 a and b. The number preceding the weld configuration designation denotes the sample number from each duplicate set.

Upon test completion the weld joints were rinsed under cool running distilled H_2O to remove any salt deposits. The samples were then photographed. The duplicates that showed the most visual corrosion were then cross-sectioned and examined under an optical microscope according to the procedure previously mentioned in Section 3.2.

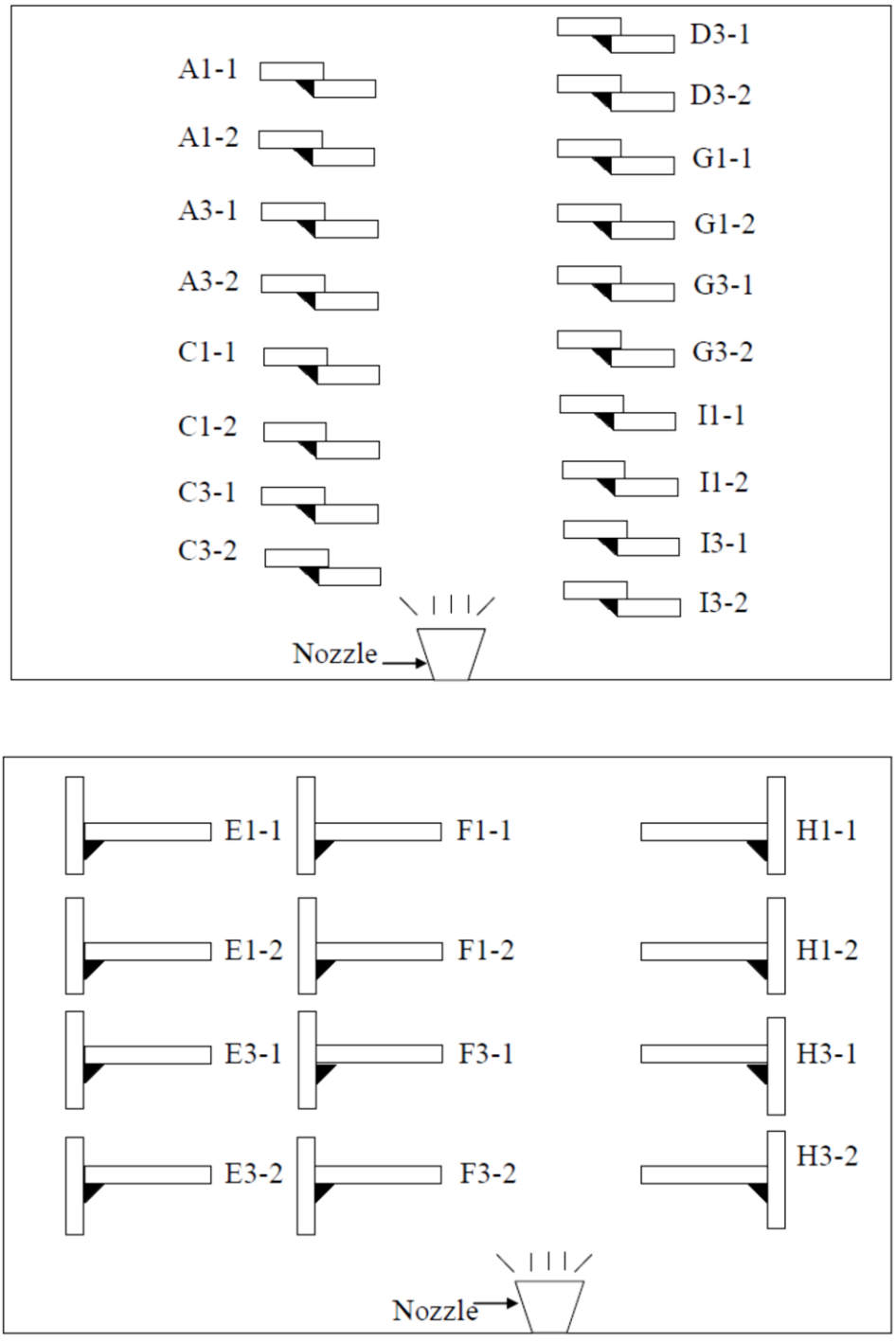

Figure 13: ASTM G85 welded AA7xxx (a) lap-joint and (b) T-joint corrosion chamber rack lay-outs. Internal corrosion chamber dimension necessitated seperate exposure of lap-joint and t-joint weld configurations.

3.3.2 GM-14872

In order to examine the corrosion behavior of each weld joint configuration in a near neutral pH environment, exposure according to the GM Worldwide Engineering Standard GMW-14872 "Cyclic Corrosion Laboratory test" [116] was conducted. The essential details are summarized below.

Quadruplicates from each weld joint configuration were used for this experiment. Weld joints were exposed in the as-received condition with no surface preparation prior to exposure. Weld joint configurations were ultrasonically cleaned in methanol (CH_4O) for a period of 5 min then dried under a hot air stream. No action was taken to mask off any rear or side faces of the weld joint with silicone. This ensures that the conditions closely mimicked real-world conditions. Weld joints were weighed and photographed prior to exposure. All GMW-14872 exposures were conducted in a large environmentally controlled chamber at GM's Milford Proving Grounds (Milford, Michigan, USA). The weld joints were then mailed to McMaster University for further post exposure analysis.

The adopted procedure involved exposing the quadruplicates to a near neutral pH complex salt spray for a period of 120 days (150% of the time specified in the GM standard). Each cycle lasted 24 h and consisted of an 8 h salt spray step (at 25°C with a relative humidity of 45%), an 8 h humidity step (at 49°C with a relative humidity of approximately 100%), and a final drying step (at 60°C with a relative humidity of less than 30%).

Test solutions were prepared in inert plastic containers by dissolving 90 g of NaCl, 10 g of calcium chloride ($CaCl_2$), and 7.5 g of sodium bicarbonate ($NaHCO_3$) in 10 L of distilled H_2O. The measured pH range of the solution was 6.8-7. Test solutions were then sprayed onto the weld joints by a pressurized nozzle controlled by a GM laboratory technician. Salt spray exposures were conducted by hand 4 times during the spray stage, approximately 1.5 h after the previous application in order to allow adequate time for weld joints to dry. During this stage, the racks were removed from the environmental chamber to sit for 8 h and facilitate the salt spray.

During exposure to GMW-14872, weld joints were placed on perforated, coated, and movable steel racks. Welded lap-joint configurations were laid on their backsides with the weld facing up. Meanwhile, welded T-joint configurations were placed upright with the AA7xxx extrusion parallel with the vertical.

Upon test completion the weld joint configurations were cleaned using a mild sand blast at 80 psi to remove any corrosion by-products from the surface of the sample. Upon arriving at McMaster University, the weld joints were photographed. From the quadruplicate set, a single set was used for characterization using light optical microscopy as outlined in Section 3.2 and the remaining triplicates were used for tensile-shear testing, as will be outlined in Section 3.5

3.4 Potentiodynamic Polarization

Potentiodynamic polarization curves for three different weld zones (weld, HAZ and unaffected base alloy), from AA7003 and AA7108 in the as-welded T6 and the as-welded T6+PB conditions, were measured in an acidified NaCl solution at room temperature.

Measurements were conducted using a 3 electrode (working, counter, reference) electrochemical test cell with a volumetric capacity of 1000 ml. Working electrodes were prepared by cutting small rectangular samples (0.7 cm^2-1 cm^2) of each weld zone in the as-welded T6 and the as-welded T6+PB condition . Electrical contact was achieved by attaching a length of copper (Cu) wire to the back of the rectangular samples with conductive Al tape, which was then cold-mounted in epoxy. The electrical lead was then inserted into an inert plastic tube and attached to the back of the cold mount with more epoxy. All working electrodes were sequentially ground from 1200 grit to 4000 grit with SiC paper using H_2O as a lubricant 15 min prior to immersion. All potentials were measured against an external saturated calomel reference electrode (SCE), which was electrically connected to the test solution using a Luggin salt bridge. The reference potential of the SCE electrode is +244 mV versus the standard hydrogen electrode (SHE). A single graphite rod was used as the counter electrode.

Test solutions were prepared by using NaCl, CH_3CO_2H, and distilled H_2O, as previously mentioned in Section 3.3.1, to a total volume of 1000 ml. Each measurement was made in freshly produced solution. No attempt was made to aerate, deaerate, or stir

the test solutions during immersion. The procedure first involved measuring the open circuit potential (OCP) for a period of 60 min before commencing with the potentiodynamic polarization. All polarization measurements were made at a scan rate of 0.2 mV/s using a computer-controlled potentiostat (Gamry Reference 600). Scans began at a potential of -250 mV more negative than the OCP and concluded once a current density of 10 mA/cm^2 was reached. As a consequence of limited sample availability, polarization measurements were only conducted once. HAZ and unaffected base alloy samples were not reused in order to avoid taking polarization measurements on the fibrous fine-grained interior, which ensured measurements were taken on the dynamically recrystallized grain surface layer to match exposure conditions of the ASTM G85-A2 test.

3.5 Tensile-Shear Testing

The shear strength and strain of welded lap-joint and T-joint configurations, unexposed and exposed to GMW-14872, were determined by conducting tensile-shear experiments with the aid of a custom made tensile jigs.

To complete the tensile-shear tests, custom jigs were fabricated out of tool steel (AISI 4041) to accommodate both lap-joint and T-joint weld geometries. Each jig has an adjustable clamp and a built-in stabilizing roller support, shown in Figure 14, to reduce any bending experienced in the area adjacent to the weld region during the tensile-shear pull. The typical arrangement of a lap-joint weld configuration in the custom jig is shown in Figure 14. The T-joint jig is comprised of an adjustable clamp, without a roller support, and a second adjustable upper clamp with cut-out channels that hold the flange (AA6063

bracket) in place. The upper clamp that holds the flange contains 2 spring-loaded ball bearings in the center channel to support and reduce bending of the web (AA7xxx beam extrusion). Two shims were placed between the flange and the bottom of the upper clamp to avoid compression of the weld region during the tensile-shear pull. The typical arrangement of a T-joint weld configuration in the custom jig is shown in Figure 15.

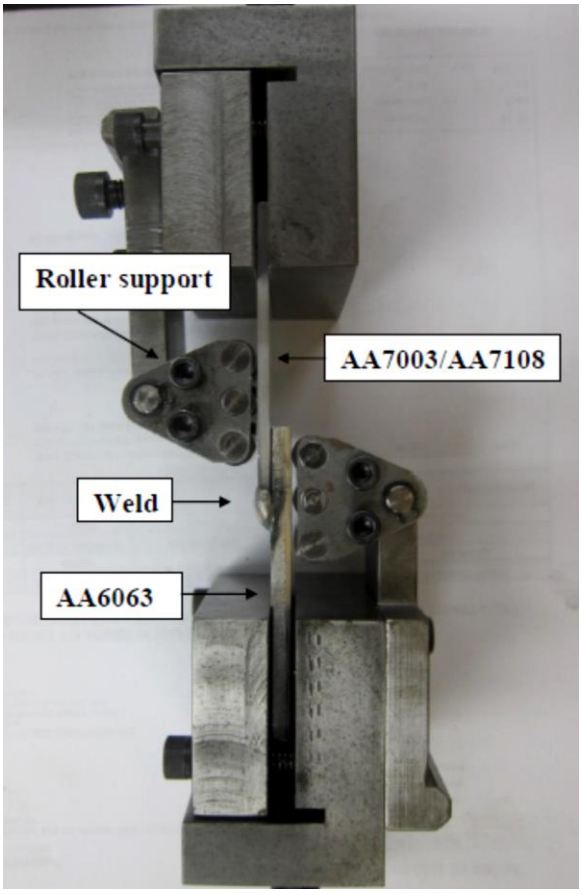

Figure 14: Typical arrangement of a AA7xxx lap-joint weld in the custom jig - all major weld assembly parts are labeled.

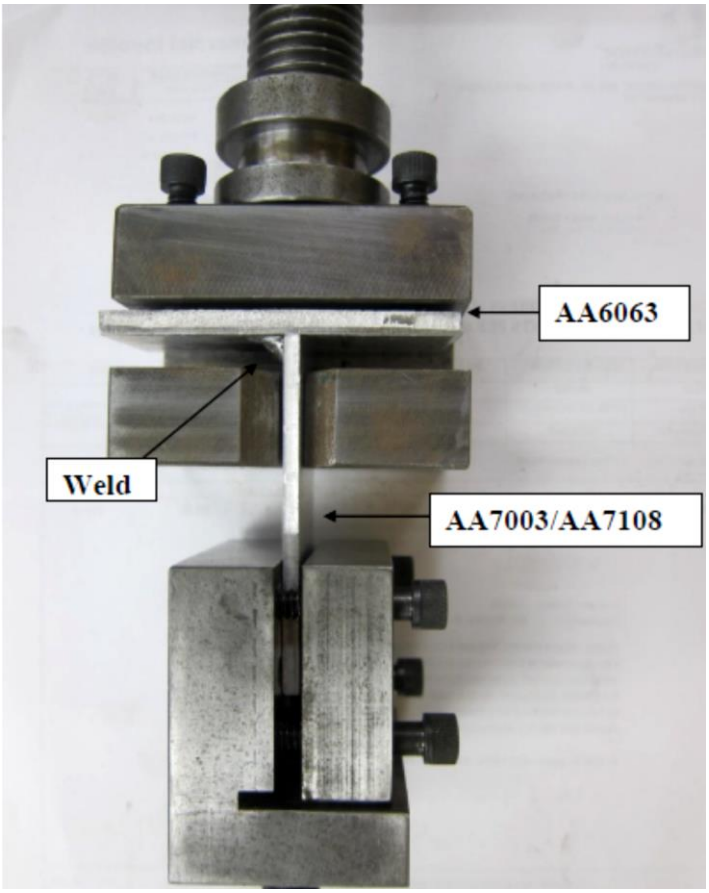

Figure 15: Typical arrangement of a AA7xxx T-joint weld in the custom jig - all major weld assembly parts are labeled.

Preliminary tests with the custom jig showed that the flange of the T-joint welds was permitted to deform with the as-received dimensions. A modified "dog-bone" specimen geometry was then adopted, which eliminated the distortion of the flange. The modified specimen geometries of the lap-joint and T-joint welds configurations is shown, respectively, in Figures 16 a and b.

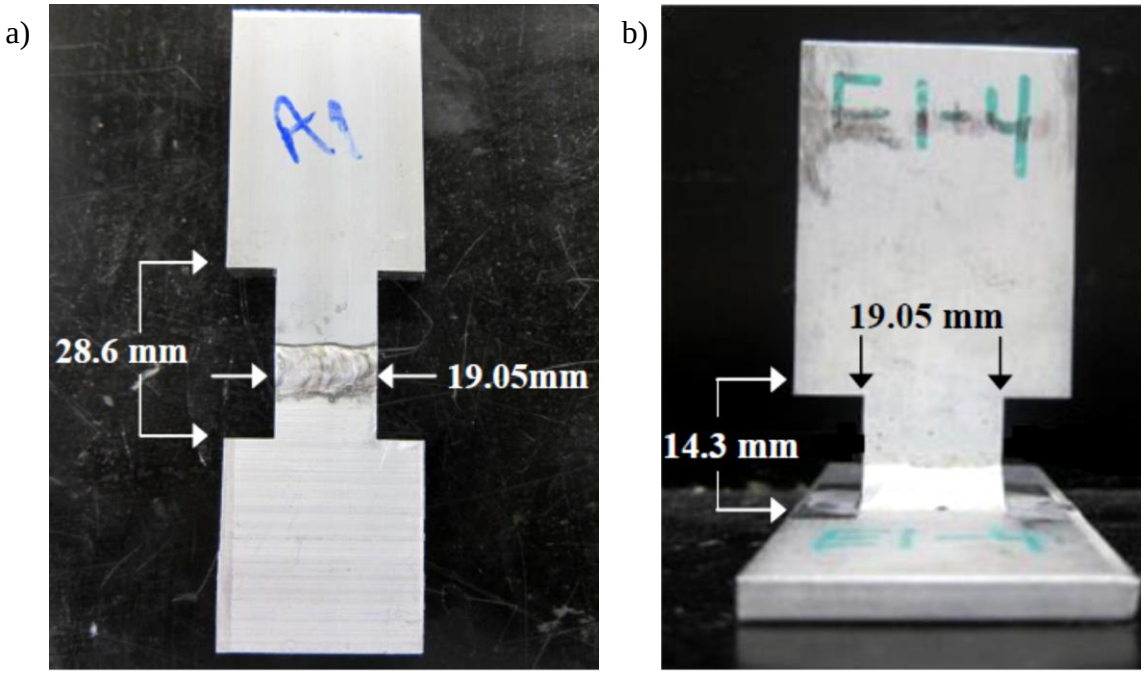

Figure 16: Modified (a) lap-joint and (b) T-joint weld sample geometries adopted for tensile-shear testing.

Tensile-shear testing was carried out using a 250 kN tensile machine (MTS) at a cross-head speed of 1 mm/min. The data output of each tensile-shear test was given in load vs. displacement. Shear-fracture stress (τ_{frac}) was obtained by dividing the force at fracture by the theoretical throat area (A). Shear-fracture strain (ε_{frac}) was determined by taking the tangent of the shear plane's angle from the vertical, which was determined through observation under a stereoscope (Nikon LV100). The theoretical throat area (A) was calculated according to Equation 3. The values l_{AB}, l_{BD}, l_{BC} and L denote the horizontal leg length, vertical leg length, throat length, and weld length. The sample geometry used to derive Equation 3 is shown in Figure 17. Triplicates were used, the

average of each configuration's shear-fracture stress and strain was then obtained and compared in the exposed and unexposed conditions.

$$A = L \cdot l_{BC} = L \cdot l_{AB} \sin\left(\tan^{-1}\frac{l_{BD}}{l_{AB}}\right) \qquad \text{Equation 3}$$

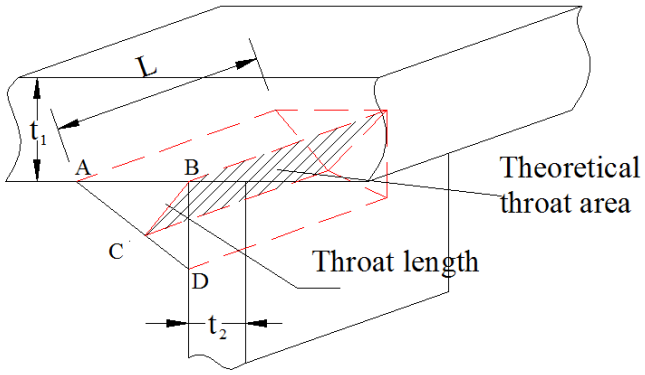

Figure 17: Sample geometry used to derive a mathematical expression to determine the theoretical throat area

4.0 Results

4.1 Weld Joint Characterization

The major microstructural observations found in the three different weld zones (the unaffected base alloy, the HAZ, and the weld) using optical light microscopy are described in detail below.

The microstructures of the cross-sectioned AA7003 and AA7108 extruded base alloys displayed a dual-grain structure, a coarse-grained dynamically recrystallized surface layer, and a fibrous fine-grained interior. Figure 18 a and b show the typical appearance of this dual-grain structure, respectively, for AA7003 and AA7108 along the L-ST plane. The measured thickness of the coarse recrystallized surface layer of the AA7003 extrusion was observed to be 121.9+/- 26.2 µm, compared to the recrystallized surface layer of AA7108 which was found to be 171.3+/- 50.8 µm. Similar recrystallized

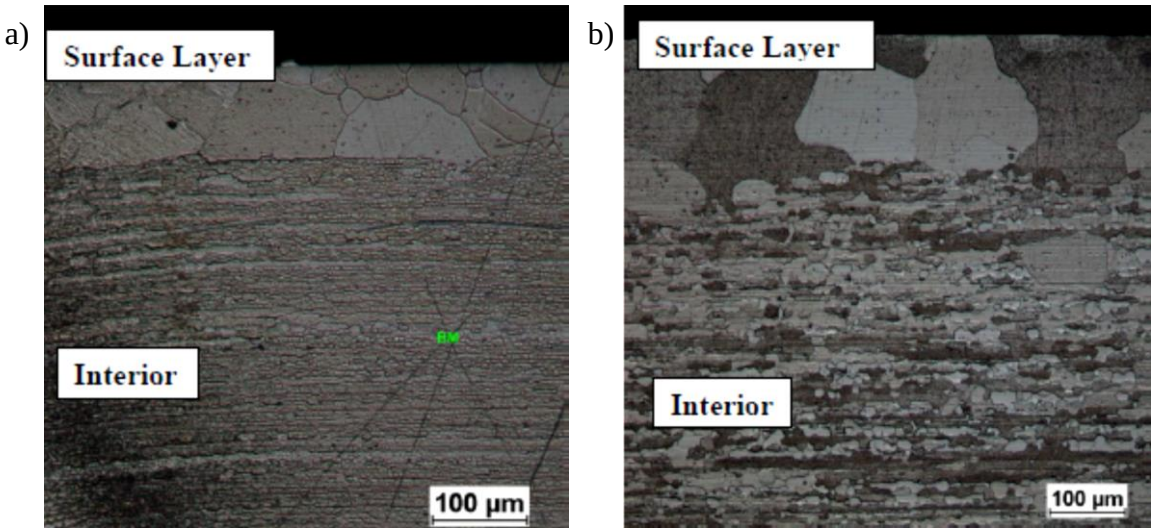

Figure 18: Cross-sectioned (L-ST plane) micrographs showing the coarse-grained surface layer and fine-grained interior microstructure of the unaffected base alloys of (a) AA7003 and (b) AA7108 observed in lap-joint configurations A1 and C1 respectively.

surface layer thicknesses for both AA7003 and AA7018, were observed in cross-section for the LT-ST plane, 114.6+/-28.3 µm and 177.2+/- 44.5 µm. Moreover, similar observations were made on the extruded base alloy in the as-welded T6+PB condition.

Figure 19 a and b show, the typical fine-grained interior microstructure observed along the L-ST and LT-ST planes of AA7003, respectively. From Figure 20 a, it was observed that the L-ST plane displayed a degree of grain directionality along the L-direction (parallel to the extrusion direction) as a result of grain elongation along the extrusion direction. Conversely, Figure 20 b, shows a randomly distributed equiaxed grain structure with no observed grain directionality in the LT-ST plane. Similar observations were made about the AA7108 extrusions. Micron-sized secondary phase particles that are randomly distributed along grain boundaries and grain interiors are also observed in Figure 19 a and b,in both the coarse-grained surface layer and the fine-grained interior. A previous study of AA7003 by Krishnan [13] revealed these particles to be Al12(Fe,Mn)3Si and Al3Fe.

a) b)

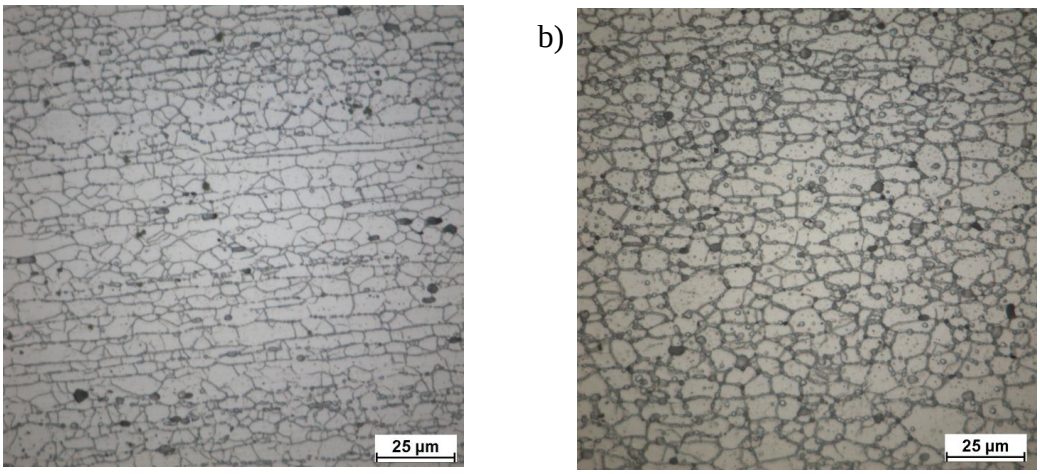

Figure 19: Cross-sectioned micrographs of the fine-grained interior of AA7003 along the (a) L-ST plane and (b) LT-ST plane observed in lap-joint configuration A1.

Figure 20 a and b shows a set of images that document the typical appearance of the HAZ microstructure of AA7003 and AA7108 at the fusion line of a ER5356 weld in a lap-joint welded configuration. The dual-grained structure observed in the AA7xxx base alloy extrusions was also observed in the HAZ and appeared unaltered along with the aforementioned micron-sized secondary phase particles. Similar observations were made in T-joint welded configurations.

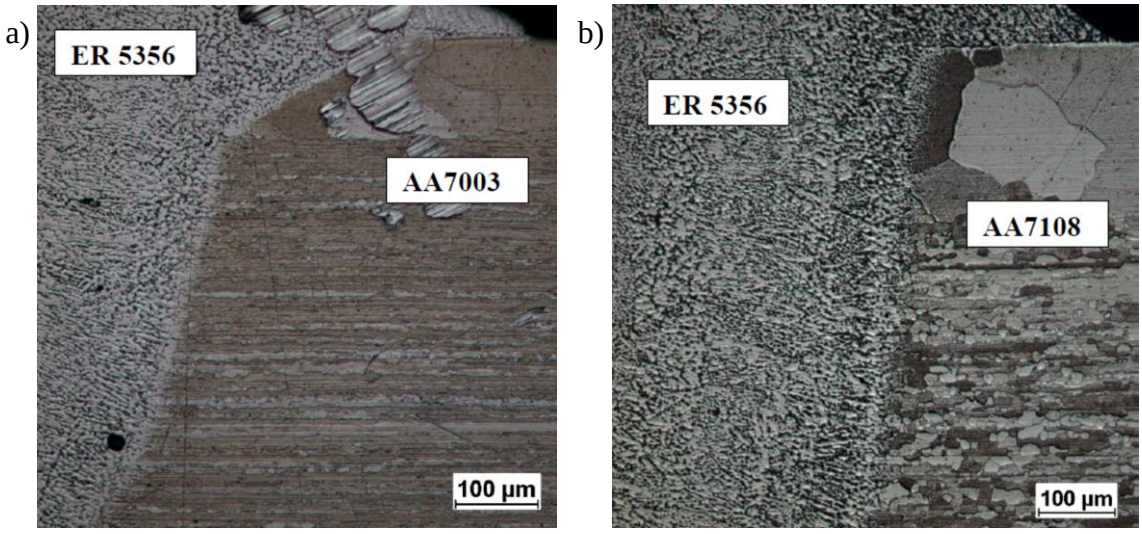

Figure 20: Cross-sectioned fusion line micrographs of (a) AA7003 and (b) AA7108 welded with ER5356 filler found in lap-joint configurations A1 and C1.

Cross-sectioned ER5356 and ER4043 welds revealed an as-cast dendritic microstructure with secondary phase particles occupying the interdendritic regions. The as-cast dendrites of the ER4043 weld, Figure 21 a, appeared to be larger in size with fewer secondary particles in the interdendritic regions compared to the ER5356 weld. Along the fusion line of various ER5356 welded AA7xxx lap-joint and T-joint configurations (A1, A3, C3, E1, G3, H1 and I3) a narrow zone formed, which contained

significantly less precipitated secondary phase particles relative to the adjacent ER5356 weld, shown in Figure 21 b. Observation of the fusion line of lap-joint configuration D3 (ER4043/AA7003-T6+PB/⊥), Figure 21 a, showed a small narrow region in the weld about 20-100 µm wide, that had larger recrystallized grains compared to the adjacent as-cast weld microstructure.

a)

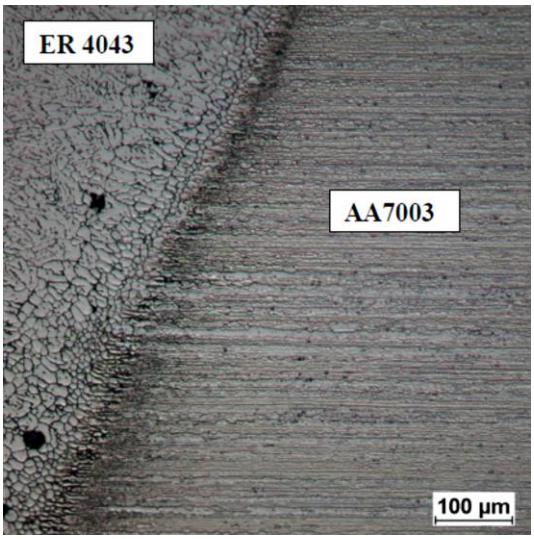

b)

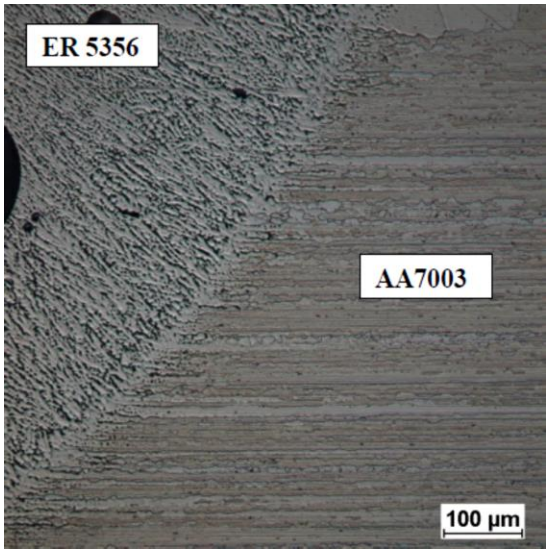

Figure 21: Cross-sectioned fusion line micrographs of (a) AA7003/ER4043 lap-joint configuration D3 and (b) AA7003/ER5356 T-joint configuration E1.

Figure 22 shows the typically observed unimodal grain size distribution plot and Table 5 shows the results of average grain size measurements conducted on the unaffected base alloy and HAZ cross-sectioned planes (L-ST and LT-ST) of AA7003 and AA7018 lap-joint configurations A, C, G and I. All measurements were conducted in the fine-grained interior of each weld joint. The average grain sizes observed in the unaffected base alloy and HAZ of the weld joints fall in a very narrow range of 4.2 μm to 6.6 μm, regardless of heat treatment, cross-sectioned plane, and alloy composition.

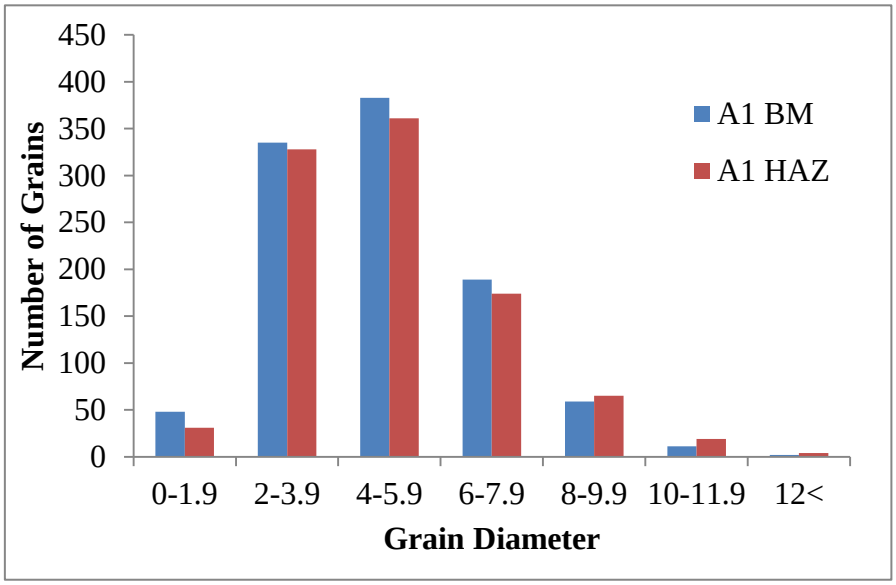

Figure 22: Typical unimodal grain size distribution observed in the unaffected base alloy and HAZ of welded AA7003 and AA7108. Data collected from the fine grained interior of the unaffected base alloy and HAZ of lap-joint configuration A1.

Table 5: Average grain diameter measurements made in the fine-grained interior.

Configuration	Average base alloy grain diameter (µm)	95% Confidence Interval (µm)	Average HAZ grain diameter (µm)	95% Confidence Interval (µm)
A1	4.8	4.7-4.9	4.9	4.8-5.0
A3	4.2	4.1-4.3	N/A	N/A
C1	5.5	5.3-5.7	6.5	6.2-6.8
C3	4.9	4.8-5.0	4.8	4.7-4.9
G1	5.5	5.3-5.7	N/A	N/A
G3	5.3	5.2-5.4	4.9	4.8-5.0
I1	5.6	5.4-5.8	6.5	6.3-6.7
I3	6.2	5.9-6.5	6.6	6.3-6.9

*****N/A – Not Available. N/A values correspond to samples which exhibited a heavily degraded grain interior from etching before grain-boundaries were detailed enough for image analysis software.

The cross-sectioned micrographs of the weld joint configurations revealed the presence of several types of weld defects in both lap-joint and T-joint geometries. These weld defects are shown in Figures 23-26. Figure 23 a and b respectively show two types of porosity defects, scattered porosity and linear porosity, found primarily in ER5356 welds. Scattered porosity, Figure 23 a, was a predominant defect found in most weld joints, with the highest degree found in T-joint welded configurations. Figure 23 b shows linear porosity adjacent to the ER5356/AA6063 fusion line of a T-joint welded configuration. Linear porosity was also found adjacent to the ER5356/AA7xxx fusion line of some T-joint welded configurations. Linear porosity was observed in T-joint weld configurations only. Another predominant defect observed in Figure 23 a is a lack of root

penetration, which is characterized by a lack of weld metal deposit at the root of the weld [99]. This example of a lack of root penetration is particularly excessive due to the presence of a bridging gap at the root of the weld. Observations of a lack of root penetration were made in both lap-joint and T-joint welded configurations, with the most severe cases observed in the T-joint geometry. Figures 24 a and b show, respectively, examples of a lack of fusion and over-penetration of ER5356 filler into the AA7003 extrusions. In Figure 24 a, a distinct boundary is observed between the solidified ER5356 weld and the extruded AA7003. However, the ER5356 weld metal solidified on top of the AA7003 extrusion instead of melting the extrusions and fusing with it. This in turn led to a lack of penetration.

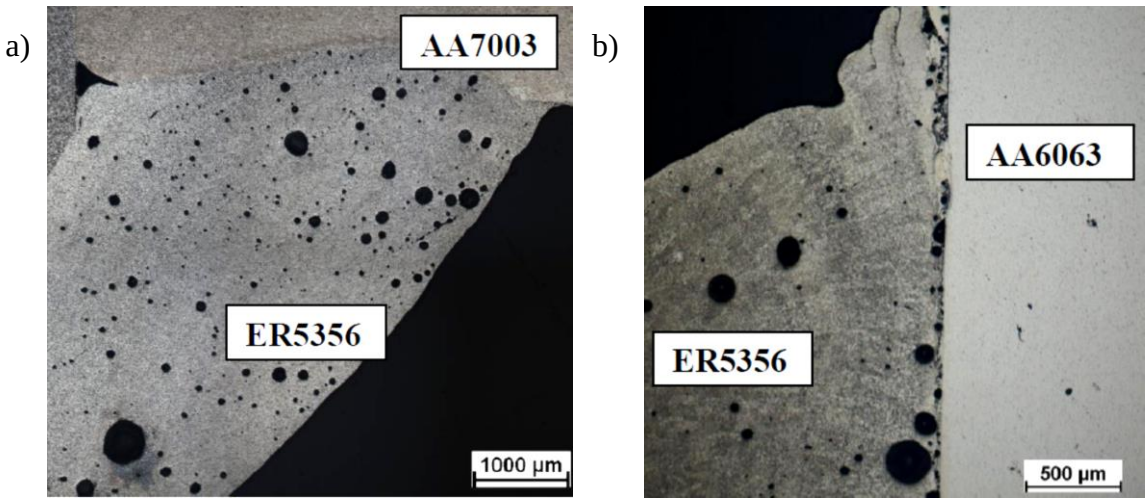

Figure 23: Cross-sectioned weld filler micrographs revealing the presence of (a) scattered porosity and lack of root penetration and (b) linear porosity observed in T-joint configuration H3.

Figure 24 b shows the over-penetration of AA7003 by the ER5356 weld metal, which reduced the cross-sectional thickness of the AA7003 extrusion to less than 1 mm at its thinnest point. Penetration defects were found only in T-joint welded configurations. Figure 25 shows a solidification crack, shown by the red arrow, observed in a T-joint welded configuration. The crack appears to originate along the interface between the AA7003 extrusion and the ER5356 weld, close to the weld root, and proceeds into the interior weld. Examples of solidification cracking were only observed in T-joint welded configurations.

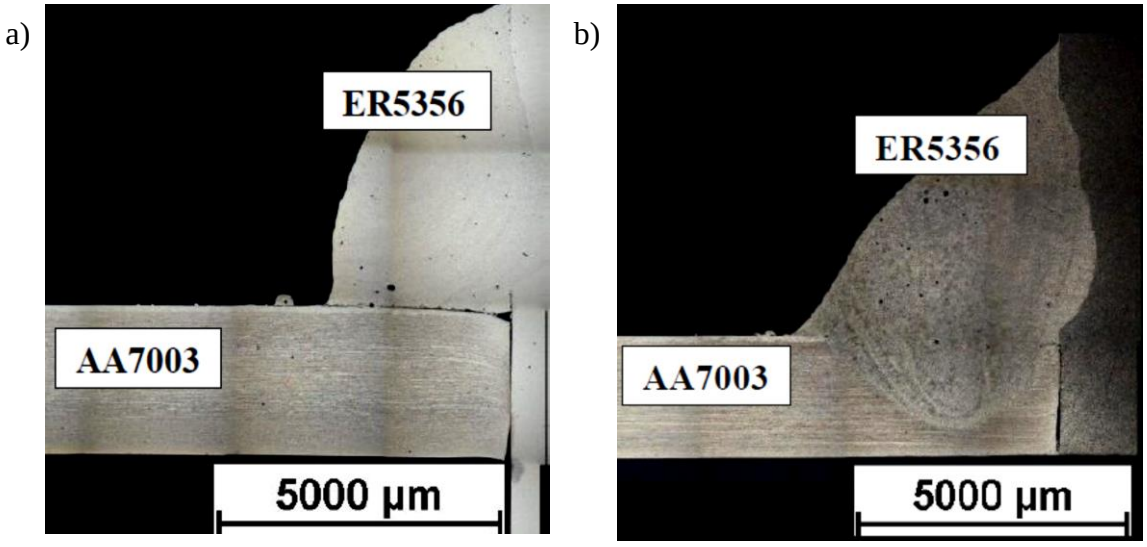

Figure 24: Cross-sectioned weld micrographs revealing the presence of (a) a lack of fusion and (b) over penetration observed in T-joint configurations E3 and E1 respectively.

Moreover, the predominant weld defect observed in lap-joint welded configurations was weld filler overlap, which is defined as the protrusion of weld metal beyond the toe or face of the weld [99]. The overlap of ER5356 beyond the weld toe of an AA7108 extrusion is shown in Figure 26. Embossment of weld filler beyond the surface of the AA7xxx extrusion, as a result of this overlap, is also evident Figure 26.

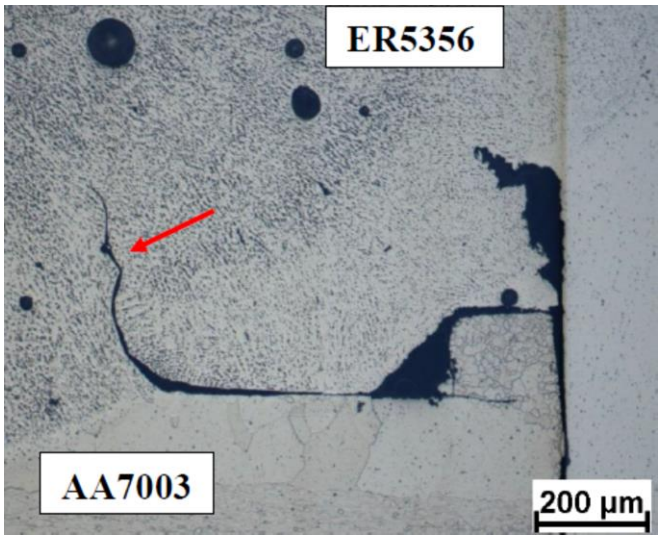

Figure 25: Cross-section micrograph of a weld root revealing the presence of solidification cracks observed in T-joint configuration H1.

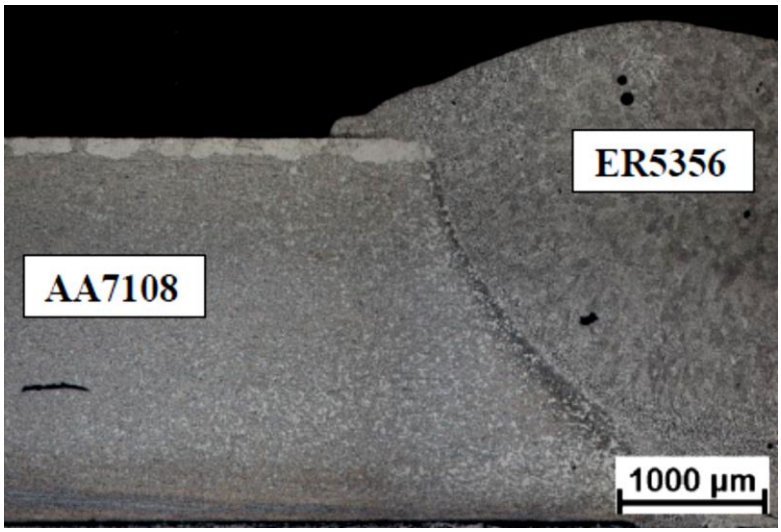

Figure 26: Cross-sections of a weld revealing the presence of overlap and embossment of weld metal beyond the weld toe observed in lap-joint configuration A1.

Microhardness measurements conducted on each weld configuration were plotted as a function of distance from the center of the weld and are provided in Appendix A.

Figures 27 a and b show the microhardness profiles, respectively, of lap-joint welded configurations A and C in both the as-welded T6 and as-welded T6+PB conditions. Several regions typically found in the microhardness profiles have also been observed in other AA7xxx welded alloys [33], [107], [104]. The first region observed is the weld denoted by the first three data points on every plot. The typical microhardness of the weld ranged between 70-85 Vickers hardness. Following the plot away from the weld a steep gradient is encountered across the fusion line, indicating the transition from the weld to the apparent HAZ of the AA7xxx extrusion. Moving away from the fusion line into the apparent HAZ, a softening region is observed in the microhardness profile, with the minima typically located 8-12 mm away from the fusion line into the HAZ. Smaller degrees of softening were observed for configurations D3, E1, F1, G1, and G3 compared to all the other weld configurations. Finally, the softened region is followed by an increase in the profile until the microhardness of the unaffected base alloy is reached. The observed elevated microhardness within the apparent HAZ prior to the softening region signified that natural aging occurred after welding. The unaffected alloy was denoted once there was no observed difference in the 95% CI between data points.

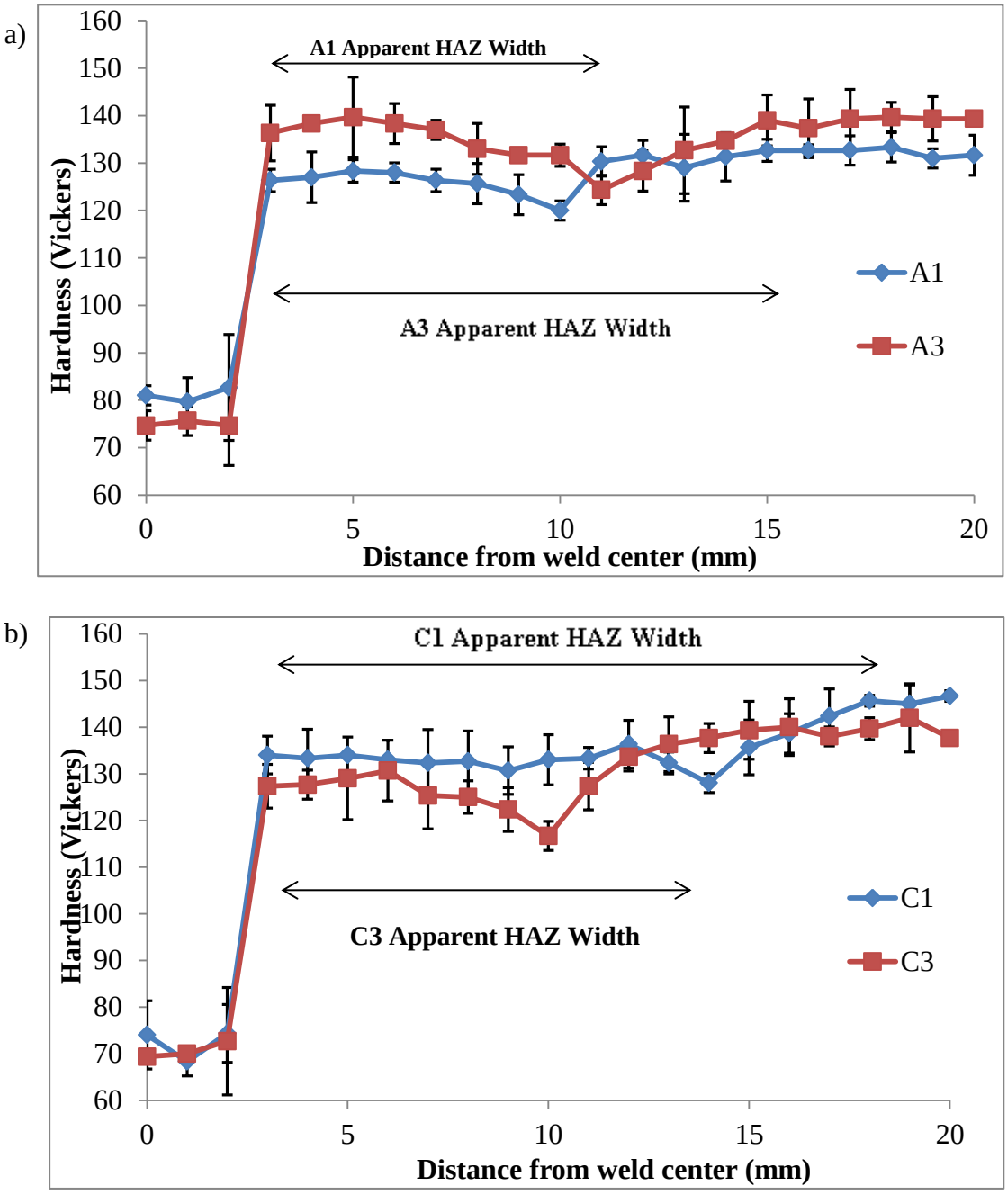

Figure 27: Typical microhardness profiles of welded (a) AA7003 and (b) AA7108 in as-welded T6 and as-welded T6+PB condition. Each error bar was calculated to a 95% confidence interval.

Table 6 demonstrates that all weld configurations in the as-welded T6 condition exhibited higher microhardness values at the initial point and throughout the HAZ and unaffected base alloy than their counterparts in the as-welded T6+PB condition. Lap-joint configurations A (ER5356/AA7003/⊥) and I (ER5356/AA7108/═) did not follow this trend. All weld configurations in the as-welded T6 condition showed an increased apparent HAZ width compared to the weld joints in the as-welded T6+PB condition. Lap-joint configuration A (ER5356/AA7003/⊥) and T-joint configuration E (ER5356/AA7003/⊥) were exceptions to this trend.

Welding direction (relative to the extrusion direction), joint geometry (lap-joint vs. T-joint), and choice of weld filler material (ER4043 vs. ER5356), with all other variables kept constant, appeared to have no significant effect on the microhardness profiles presented in Appendix A.

Table 6: Microhardness and apparent HAZ widths of welded AA7003 and AA7108

Configuration	**Initial HAZ point (Microhardness[1], distance[2])**	**Initial Point in unaffected alloy (Microhrdness[1], distance[2])**	**Apparent HAZ width**
A1	126.3, 3 mm	130.3, 11 mm	8 mm
A3	136.3, 3 mm	139, 15 mm	12 mm
C1	134, 3 mm	145.7, 18 mm	15 mm
C3	127.3, 3 mm	136.3, 13 mm	10 mm
D3	128.7, 3 mm	133, 12 mm	9 mm
E1	136.7, 3 mm	136.0, 13 mm	10 mm
E3	129.3, 3 mm	135.7, 14 mm	11 mm
F1	136.7, 3 mm	147.3, 16 mm	13 mm
F3	133, 3 mm	140, 13 mm	10 mm
G1	135.3, 3 mm	139.7, 17 mm	14 mm
G3	130.3, 3 mm	129.3, 11 mm	8 mm
H1	131, 3mm	141, 16 mm	13 mm
H3	126, 3 mm	130, 12 mm	9 mm
I1	136.7, 3 mm	148, 17 mm	14 mm
I3	136.7, 3 mm	136.7, 15 mm	12 mm

[1]Rockwell C hardness scale, [2]distance from weld center

4.2 Standardized Corrosion Testing

4.2.1 ASTM G85-A2

Photographs documenting the corrosion behaviour of each AA7003 and AA7108 weld joint configuration, following exposure to the ASTM G85-A2 acidified cyclic salt spray test, are provided in Appendix B and C. It is important to note that some results from this section have previously been published [117]. Figure 28 and Figure 29, respectively, show the typical appearance of lap-joint and T-joint welded configurations in the two heat-treated conditions, after exposure to the ASTM G85-A2 cyclic corrosion test. An attacked region adjacent to the weld, consistent with the HAZ, is observed. The width of the HAZ at the beginning of the weld (left side) is wider and tapers to a narrower width as it progresses to its end point (right side). The HAZ shown in Figures 28 a, c, and d and 29 a and c appear to be composed of 2 attacked regions: an attacked area immediately adjacent to the weld, followed by a thin attacked band observed at the outer most region of the HAZ denoting the end of the HAZ. Both attacked regions are separated by a thin region of unattacked alloy. This dual-band HAZ structure was observed on the following configurations: A1 duplicates, C1 duplicates, C3 duplicates, E1-1, F1 duplicates, F3-2, G1 duplicates, H1 duplicates, I1 duplicates, and I3 duplicates. All other samples exhibited a single-band HAZ.

Table 7 contains measured HAZ widths for each duplicate set of weld joint configurations exposed to the ASTM G85-A2 test and compares them to the apparent HAZ widths found using microhardness measurements. There is reasonable (within 3 mm

of each other) between the corrosion determined and microhardness determined HAZ of most weld joints. The only weld joint configurations to exhibit poor (4 mm or greater) HAZ width correlation between the two HAZ determining methods are A3 duplicates, C1 duplicates, I1, and I3 duplicates, including samples F1-1, G1-2 and H1-2. Interestingly, there appears to be little (0-2 mm) to no difference in the corrosion determined HAZ widths between the two heat-treated conditions.

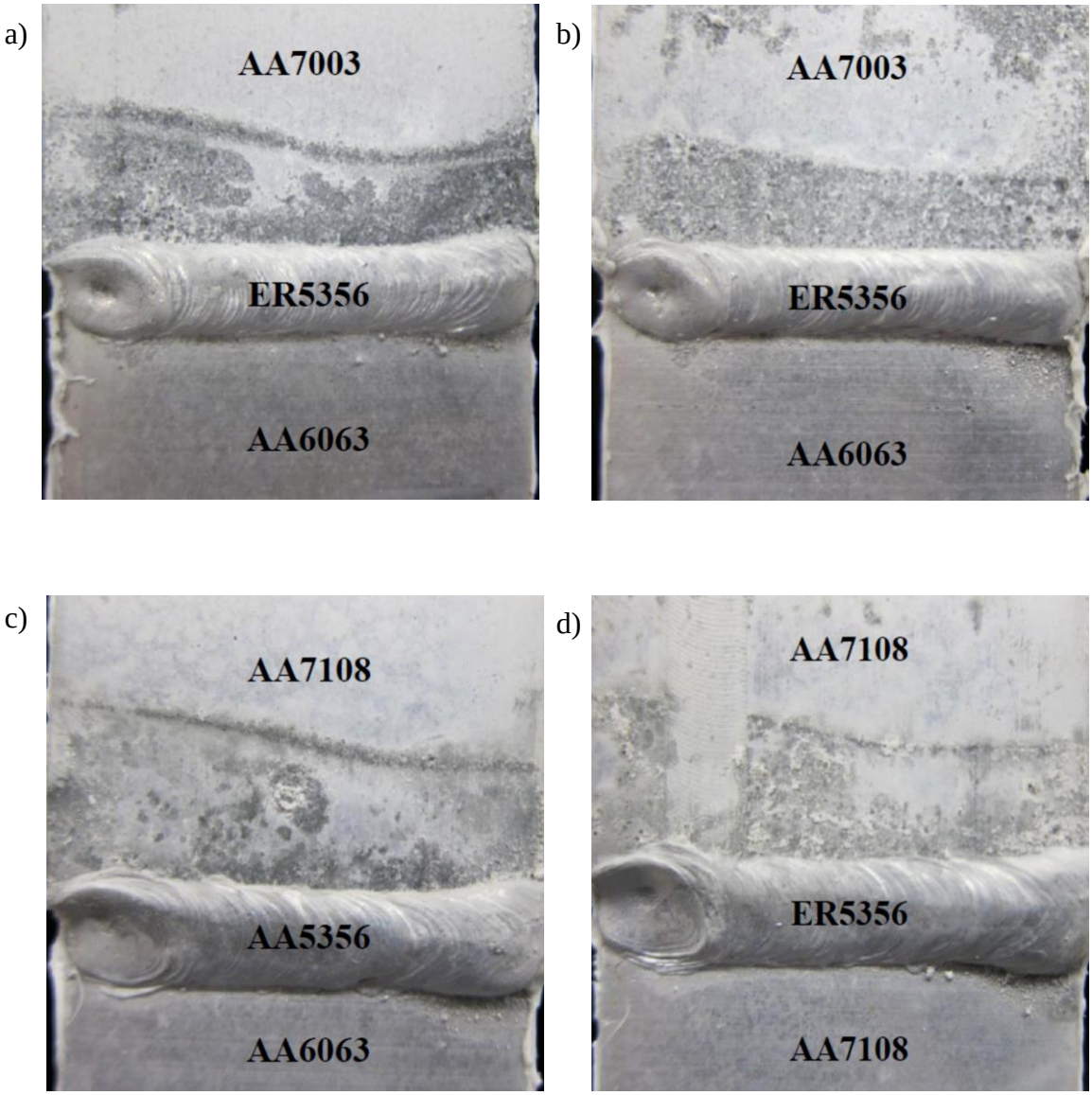

Figure 28: Photographs of lap-joint welded AA7003 (configurations A1 and A3) in (a) as-welded T6 condition, (b) as-welded T6+PB condition and lap-joint welded AA7108 (configurations C1 and C3) in (c) as-welded T6 condition, (d) as-welded T6+PB condition exposed to ASTM G85-A2.

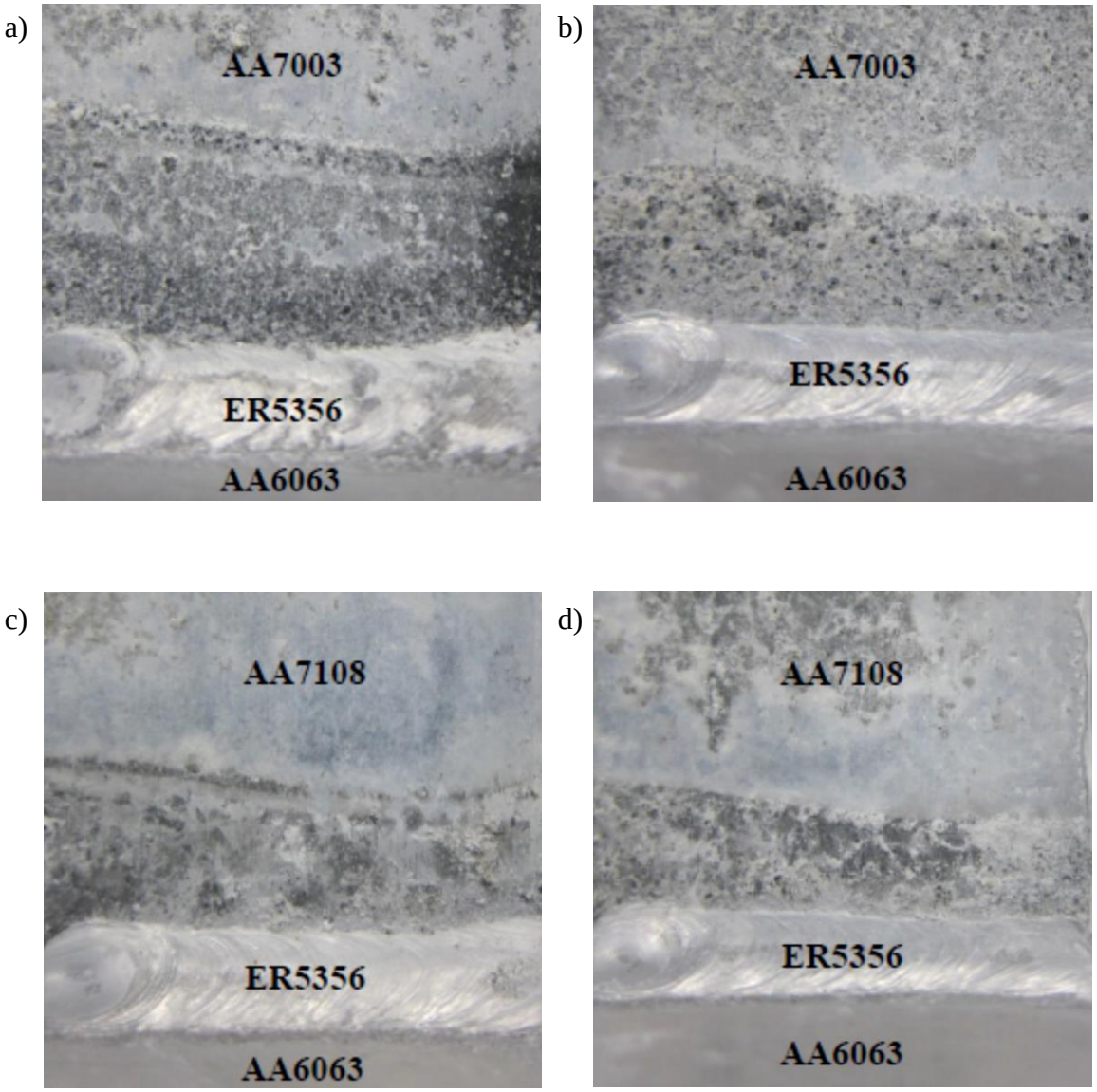

Figure 29: Photographs of T-joint welded AA7003 (configurations E1 and E3) in (a) as-welded T6 condition, (b) as-welded T6+PB condition and T-joint welded AA7108 (configurations F1 and F3) in (c) as-welded T6 condition, (d) as-welded T6+PB condition exposed to ASTM G85-A2

Table 7: Comparison of HAZ widths as measured from ASTM G85-A2 and microhardness testing.

Configuration	Corrosion Determined HAZ Width	Microhardness Determined HAZ Width
A1-1	8 mm	8 mm
A1-2	8 mm	
A3-1	6 mm	12 mm
A3-2	7 mm	
C1-1	10 mm	15 mm
C1-2	10 mm	
C3-1	8 mm	10 mm
C3-2	9 mm	
D3-1	6 mm	9 mm
D3-2	6 mm	
E1-1	12 mm	10 mm
E1-2	12 mm	
E3-1	9 mm	11 mm
E3-2	9 mm	
F1-1	9 mm	13 mm
F1-2	10 mm	
F3-1	9 mm	10 mm
F3-2	9 mm	
G1-1	11 mm	14 mm
G1-2	10 mm	
G3-1	9 mm	8 mm
G3-2	7 mm	
H1-1	11 mm	13 mm
H1-2	9 mm	
H3-1	7 mm	9 mm
H3-2	8 mm	
I1-1	9 mm	14 mm
I1-2	10 mm	
I3-1	8 mm	12 mm
I3-2	8 mm	

None of the corrosion morphologies observed post ASTM G85-A2 exposure included exfoliation corrosion. Instead, differing degrees of pitting corrosion were observed between welded AA7003 and AA7018, with no observed difference in the degree of corrosion found between the HAZ and the unaffected base alloy. The typical pitting corrosion morphology observed in the HAZ of welded AA7003 is shown in figure 30 a. A red horizontal line was added to Figure 30 a to indicate where the original surface of the extrusion once existed, as the degree of corrosion was severe enough to not leave any remnants of the original surface. Figure 30 b displays the typical pitting corrosion morphology that was observed in the HAZ of welded AA7108. The presence of small pits, indicated by the red arrows, on the surface of the welded AA7108 extrusion were

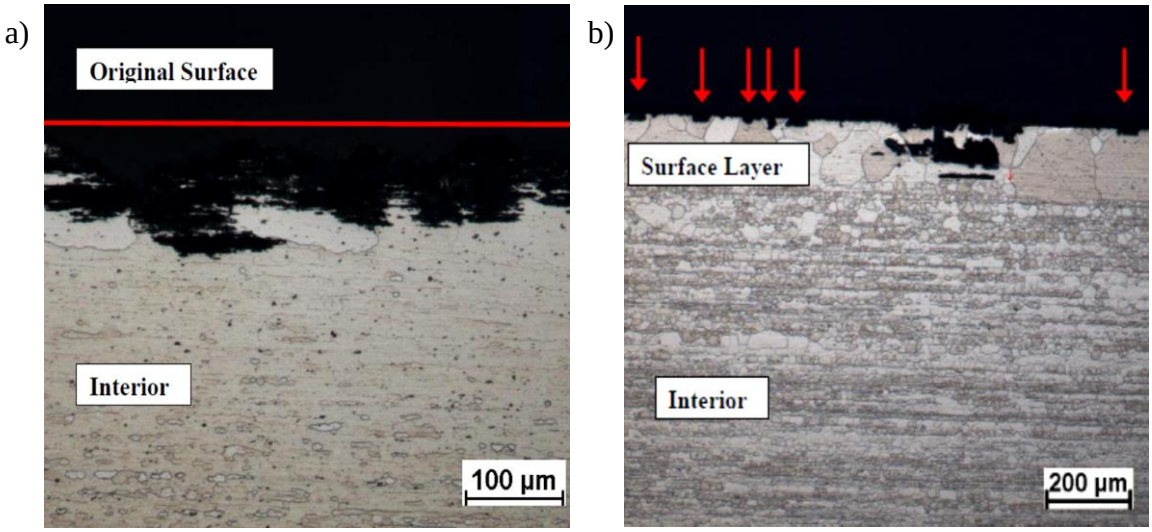

Figure 30: Cross-sections after exposure to ASTM G85-A2 showing (a) uniform and pitting corrosion in the HAZ of welded AA7003(configuration A1) and (b) pitting corrosion observed in the HAZ of welded AA7108 (configuration C1).

predominantly observed. Very few larger pits, comparable to the one observed in the center of the coarse-grained surface layer in Figure 30 b, were observed in AA7108.

Figures 31 a and b show large-area scanned images of the weld and HAZ of AA7003 and AA7108, respectively. It can be seen from Figure 31 a and b that the corrosion observed in the welded AA7003 and AA7108 was primarily confined to the coarse-grained surface layer with shallow penetration into the fibrous interior grains, with a higher degree of corrosion penetration observed in welded AA7003 – Figure 31 a. Interestingly, the end of the HAZ of both welded AA7003 and AA7108 was denoted by a trench-like pit that is noticeably larger than the pits observed in the interior of the HAZ. This trench-like pit corresponds with the second, thinner attacked region. These larger pits, which indicate the end of the HAZ, are denoted by red arrows in Figures 31 a and b. No corrosion was observed in the weld metal of any of the exposed weld configurations except in the T-joint welded configuration I3 (ER5356/AA7108-T6+PB/═). Table 8 summarizes the corrosion morphologies observed in the HAZ and unaffected base alloy of duplicate samples of welded AA7003 and AA7108 configurations exposed to ASTM G85-A2.

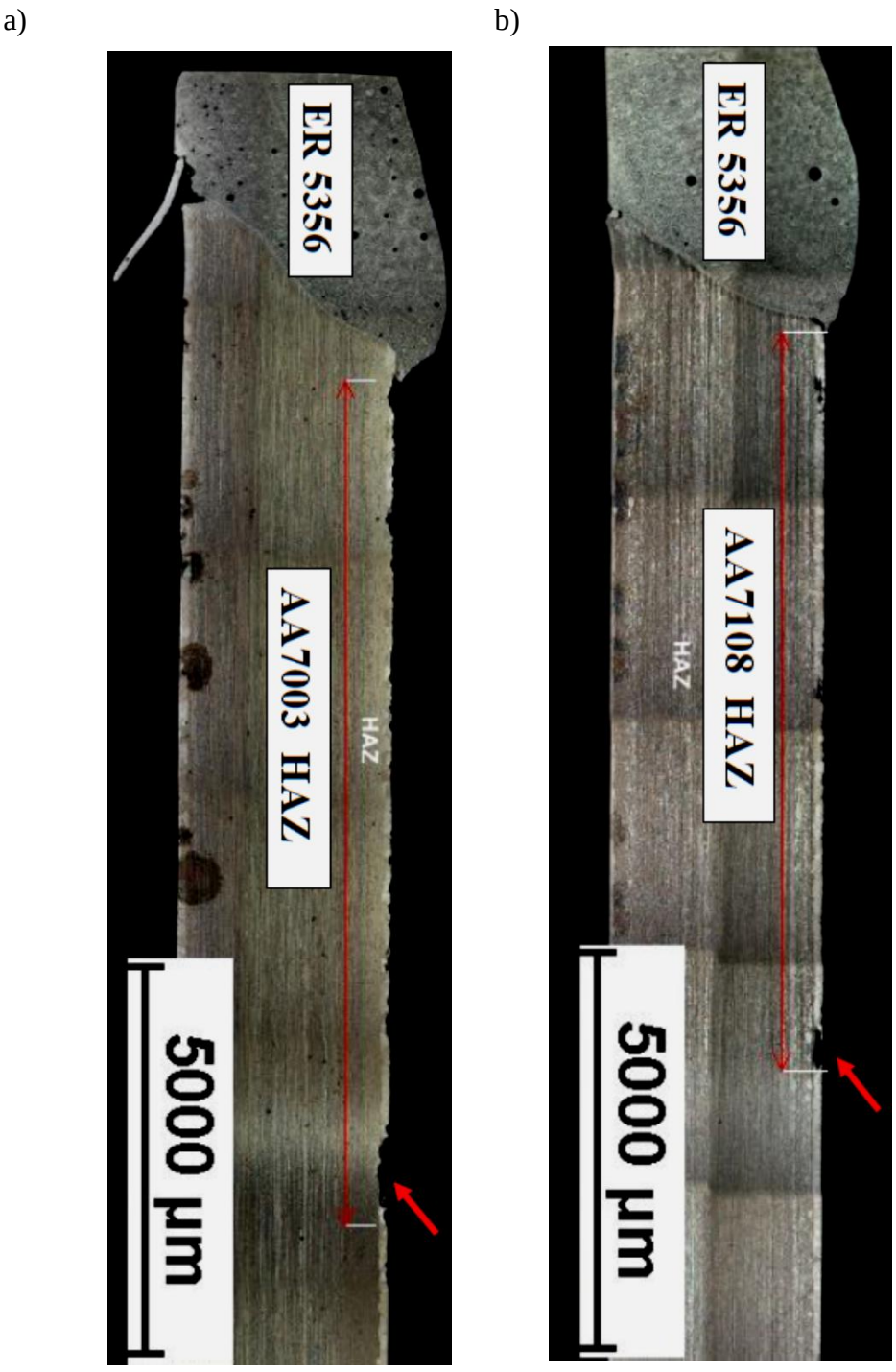

Figure 31: Large area scans of welded (a) AA7003 (configuration A1) and (b) AA7108 (configuration C1) in the as-welded T6 condition post exposure to ASTM G85-A2

Table 8: Corrosion morphologies observed in the HAZ and unaffected base alloy post exposure to ASTM G85-A2.

Configuration	**HAZ Morphology**	**Unaffected Base Alloy Morphology**
A1-1	pitting	pitting
A1-2	pitting	pitting
A3-1	pitting	pitting
A3-2	pitting	pitting
C1-1	pitting	pitting
C1-2	pitting	pitting
C3-1	pitting	pitting
C3-2	pitting	pitting
D3-1	pitting	pitting
D3-2	pitting	pitting
E1-1	pitting	pitting
E1-2	pitting	pitting
E3-1	pitting	pitting
E3-2	pitting	pitting
F1-1	pitting	pitting
F1-2	pitting	pitting
F3-1	pitting	pitting
F3-2	pitting	pitting
G1-1	pitting	pitting
G1-2	pitting	pitting
G3-1	pitting	pitting
G3-2	pitting	pitting
H1-1	pitting	pitting
H1-2	pitting	pitting
H3-1	pitting	pitting
H3-2	pitting	pitting
I1-1	pitting	pitting
I1-2	pitting	pitting
I3-1	pitting	pitting
I3-2	pitting	pitting

4.2.2 GMW-14872

Photographs showing the typical appearance of lap-joint and T-joint welded configurations of AA7003 and AA7108 exposed for 120 days to the GMW-14872 cyclic corrosion test are shown, respectively, in Figures 32 and 33. Based on the visual assessment of all the exposed weld configurations, a mild degree of discoloration was observed, but no readily marked macroscopic corrosion was found in the weld zone, HAZ, or unaffected base alloy. Photographs pertaining to the weld joints exposed to the GMW-14872 cyclic corrosion test are shown in Appendix D.

Using optical light microscopy, inspection of the exposed weld joints in cross-section yielded similar results. No corrosion was observed in either the weld, HAZ, or the unaffected base alloy of all weld joints except T-joint configuration F. In the HAZ of both T-joint welded F configurations (ER5356/AA7108/⊥), a small number of shallow pits with depths ranging from 30 μm to 50 μm into the coarse-grained surface layer were observed. Images showing these shallow pits in configurations F1 and F3, respectively, are shown in Figure 34 a and b.

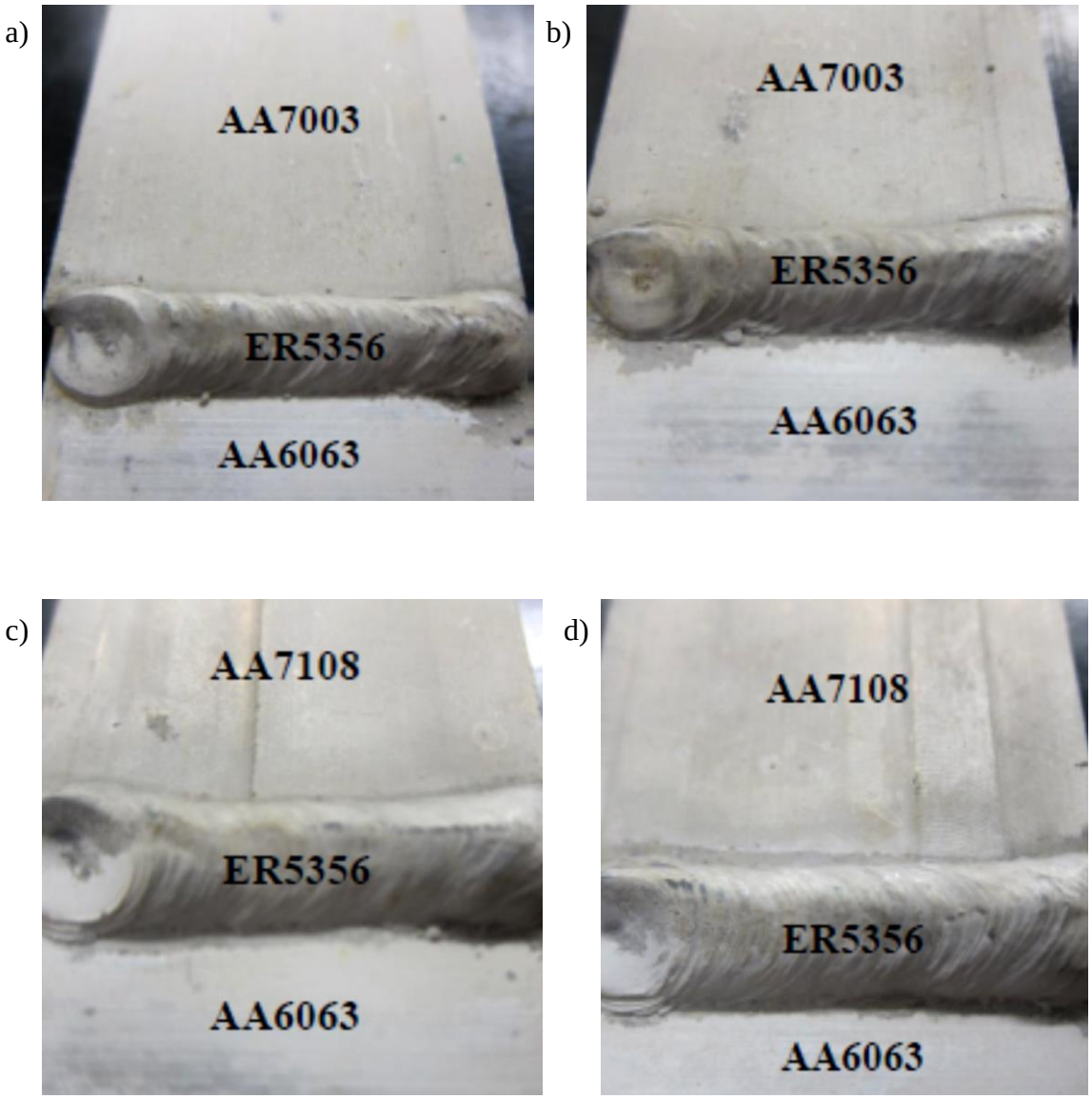

Figure 32: Photographs of lap-joint welded AA7003 (configurations A1 and A3) in (a) as-welded T6 condition, (b) as-welded T6+PB condition and lap-joint welded AA7108 (configurations C1 and C3) in (c) as-welded T6 condition, (d) as-welded T6+PB exposed to GMW-14872.

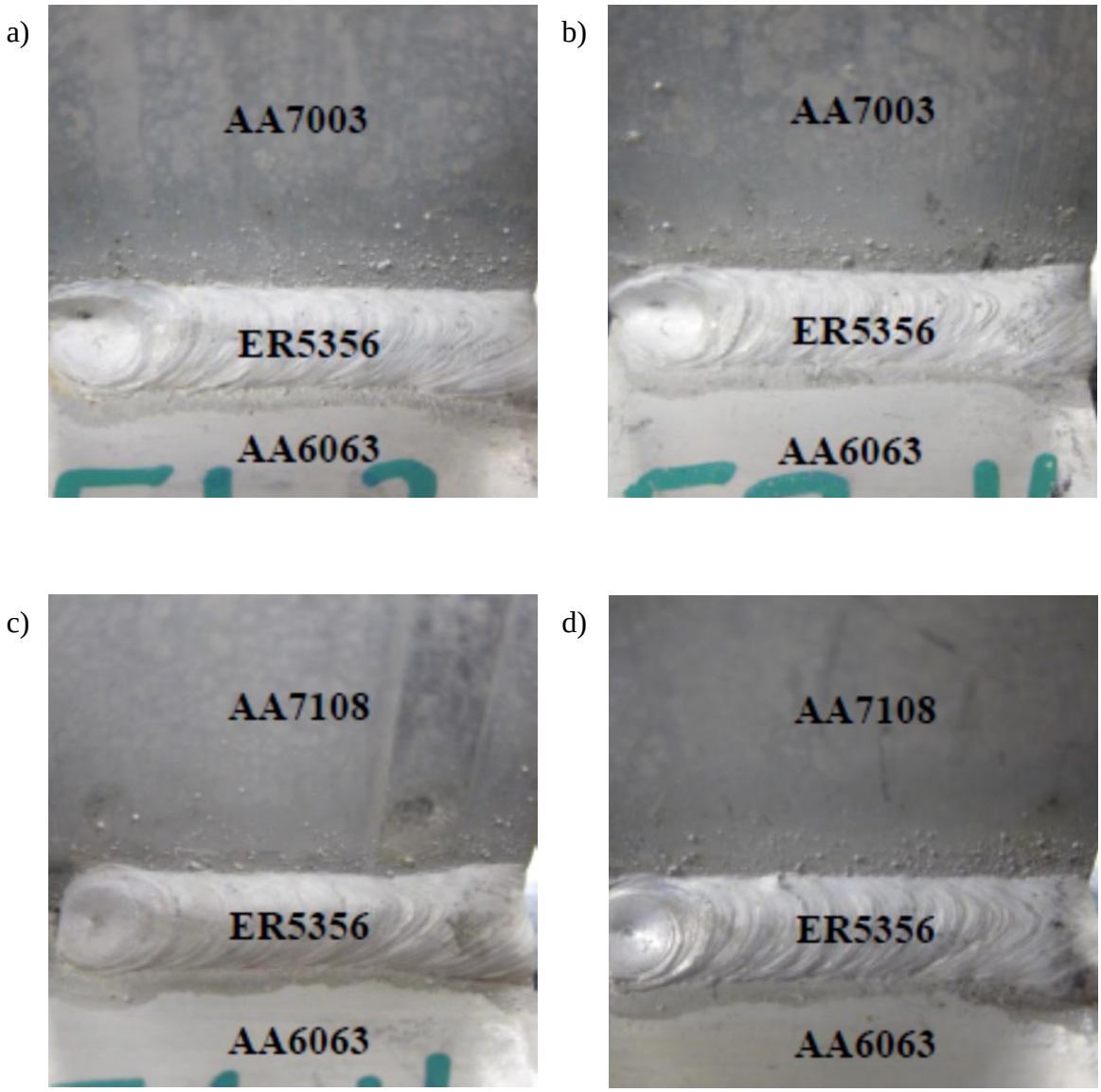

Figure 33: Photographs of lap-joint welded AA7003 (configurations E1 and E3) in (a) as-welded T6 condition, (b) as-welded T6+PB condition and lap-joint welded AA7108 (configurations F1 and F3) in (c) as-welded T6 condition, (d) as-welded T6+PB condition exposed to GMW-14872.

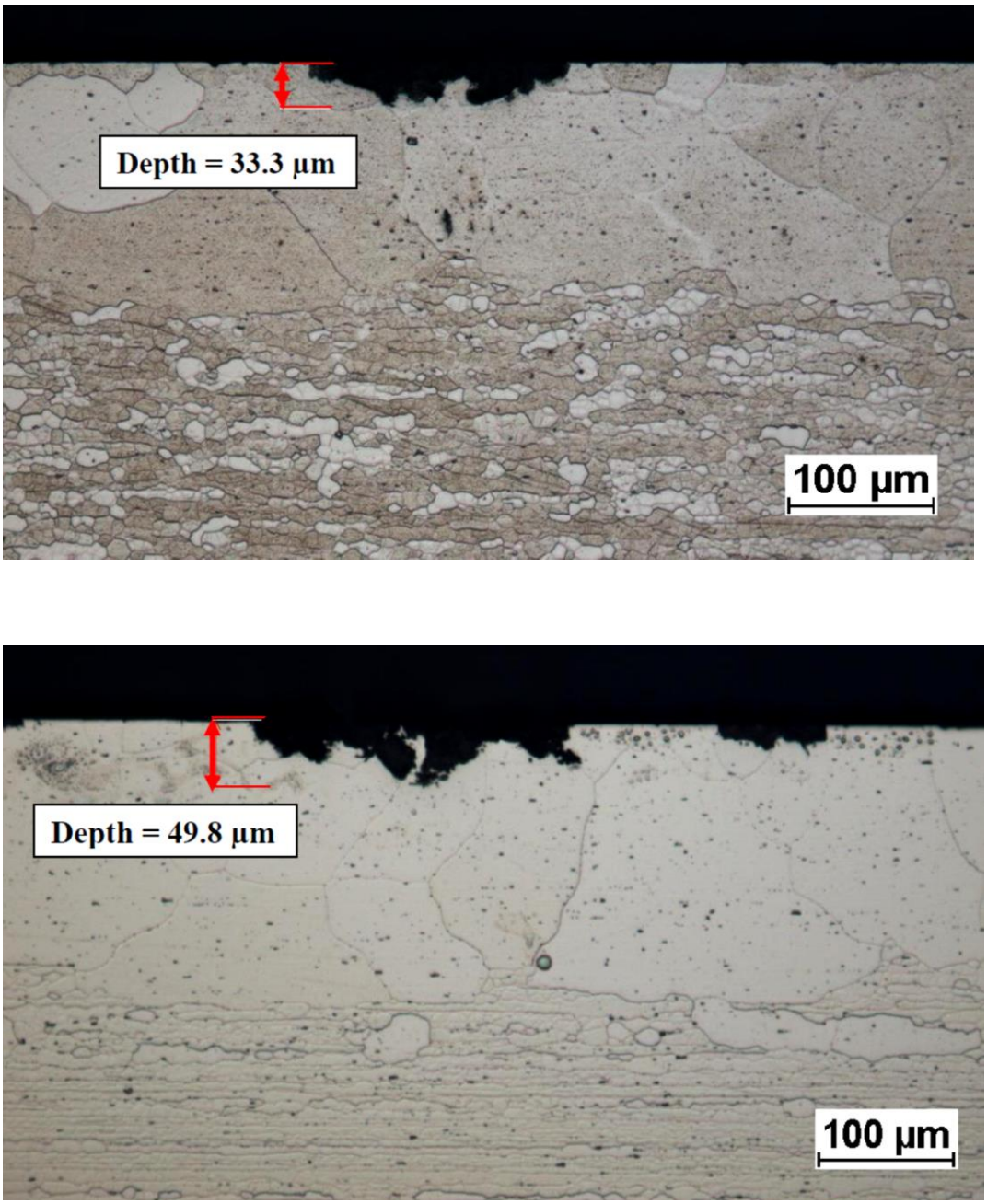

Figure 34: Cross-sections of the HAZ of T-joint welded AA7108 (configurations F1 and F3) showing shallow pits in (a) as-welded T6 condition and (b) as-welded T6+PB condition post exposure to GMW-14872.

4.3 Potentiodynamic Polarization

Potentiodynamic polarization measurements were conducted on the three weld zones of welded AA7003 and AA7108: the weld, HAZ, and unaffected base alloy. A summary of the potentiodynamic polarization results is provided below, although slight differences were observed between polarization curves, none of the difference were considered significant (< 50 mV difference).

Figure 35, 36, and 37 show the typical appearances of the potentiodynamic polarization curves corresponding to the filler alloys and AA7xxx extrusions of both the unaffected base alloy and the HAZ. At small overpotentials above the corrosion potential (E_{corr}), the anodic branch of the polarization curves shows a region of strong dependence of current density (i) on applied potential, beyond which a limiting i is approached. The difference between the polarization curves of the weld filler alloys and the AA7xxx extrusions is the appearance of a "switch-back" or S-shaped region. The "switch-back" is characterized by two potentials: the passivation potential (E_{pass}) and the breakdown potential (E_{brk}). In this study E_{pass} refers to a potential at which i decreases with applied potential. It does not refer to a potential which induces passivation and slows corrosion as a result of stable film formation. At E_{pass}, i began to decrease with applied potential until the E_{brk} was reached. Below E_{brk}, i increases significantly with applied potential until a limiting i is reached.

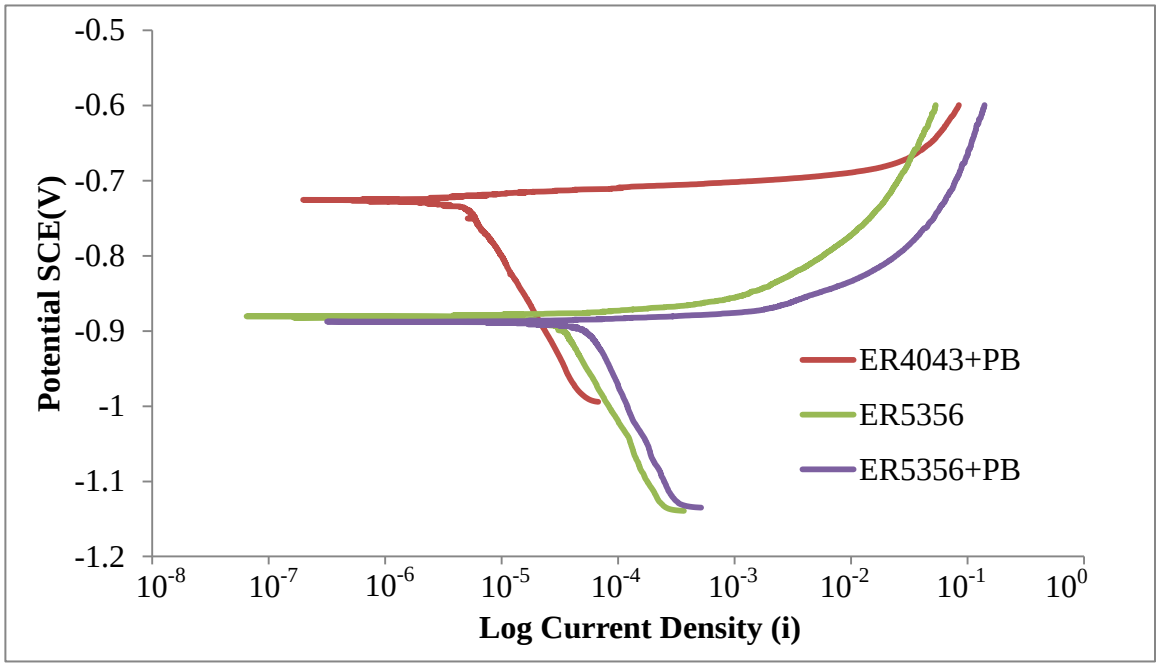

Figure 35: Potentiodynamic polarization scans of filler alloys: ER4043 as-welded T6+PB, ER5356 as-welded T6 and ER5356 as-welded T6+PB.

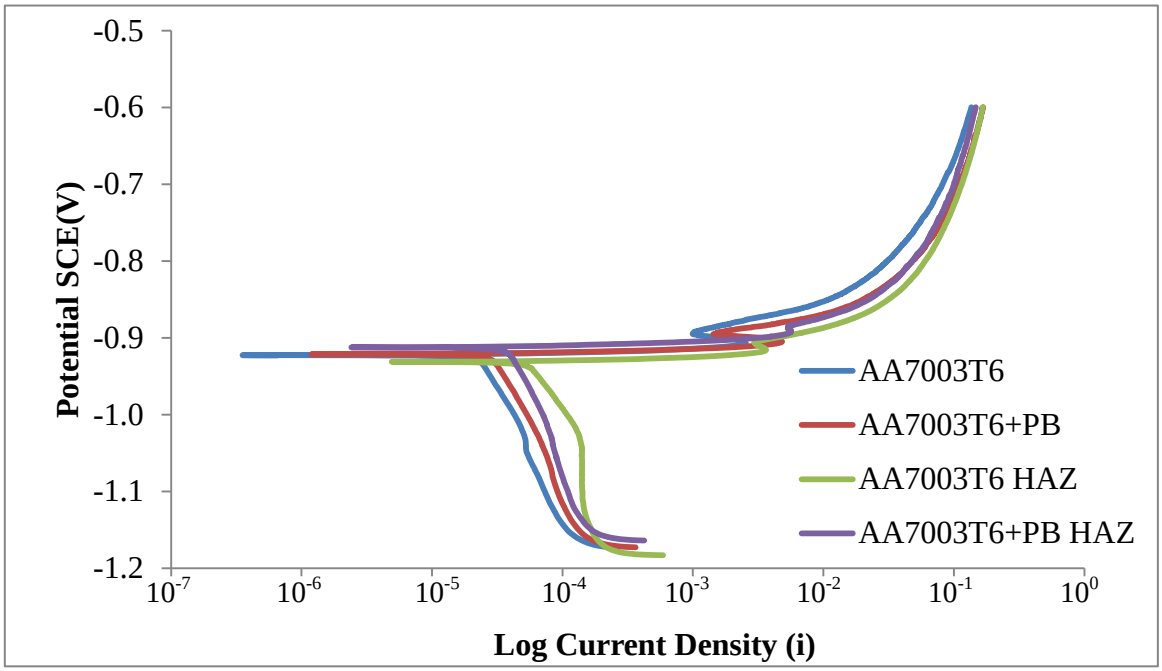

Figure 36: Potentiodynamic polarization scans of the HAZ and unaffected base alloy of AA7003 in the as-welded T6 and as-welded T6+PB conditions.

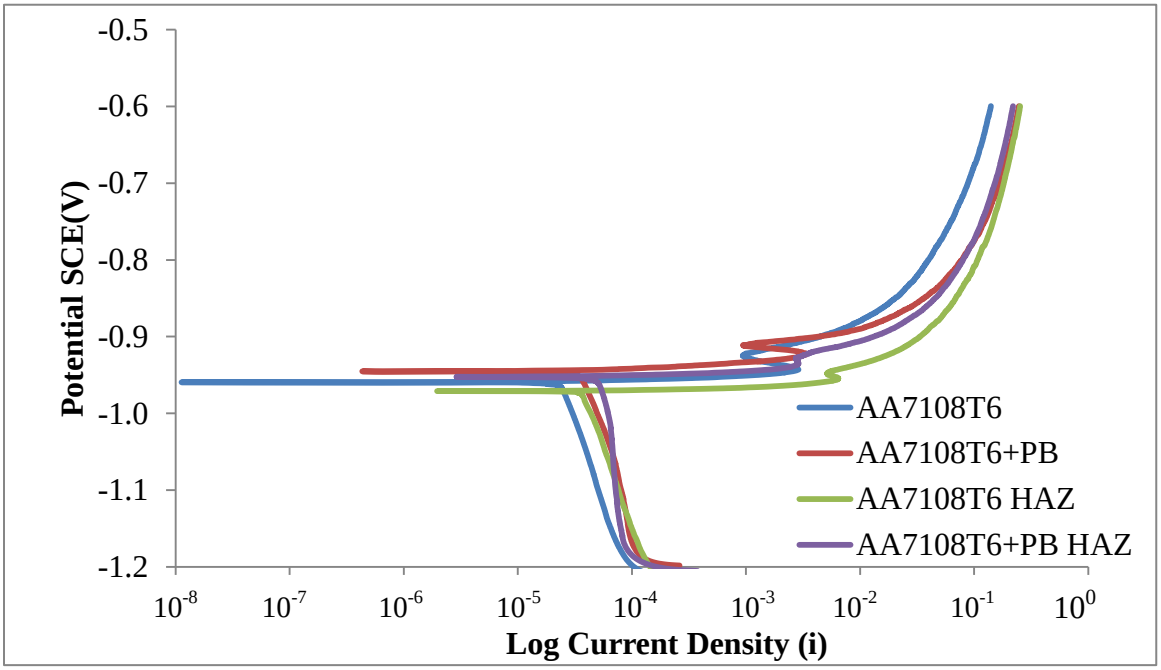

Figure 37: Potentiodynamic polarization scans of the HAZ and unaffected base alloy of AA7108 in the as-welded T6 and as-welded T6+PB conditions.

This investigation's E_{corr} and E_{brk} terms correspond to the first and second breakdown potentials initially found in Maitra and English's work, respectively [85]. This difference stems from this investigation's use of a non-deaerated solution to mimic conditions within the salt spray chamber during ASTM G85-A2 cyclic salt spray testing.

A summary of E_{corr}, E_{pass}, and E_{brk} from each polarization measurement is given in Table 9. A large difference in the E_{corr} of the two filler alloys was observed, with ER5356 as the more active of the two. The difference in E_{corr} between ER4043 and ER5356 in the as-welded T6+PB condition of the two filler alloys was +0.143 V. The difference in E_{corr} between the two heat-treated conditions of ER5356 was +0.006 V.

The unaffected base alloy of AA7108 showed to be more active than AA7003. In the as-welded T6 condition, AA7003 had a less active E_{corr} by +0.036 V, and the as-welded T6+PB condition displayed a less active E_{corr} by +0.024 V. The E_{corr} of AA7003 and AA7108 were found to be less active in the as-welded T6+PB condition compared to the as-welded T6 condition: +0.002 V and +0.014 V less active, respectively.

Similarly, no significant difference in the polarization behaviour of the HAZ compared to the unaffected base alloy for each AA7xxx extrusion was observed. The difference in E_{corr} of the HAZ and its corresponding unaffected base alloy, regardless of heat-treatment, only ranged by +0.007-0.012 V. However, the E_{corr} of the HAZ of AA7108 (in both heat-treated conditions) and the HAZ of AA7003-T6 were slightly more active compared to their unaffected base alloy counterparts.

Moreover, a slightly higher difference in the E_{brk} between the HAZ and the unaffected base alloy was observed for AA7108 (in both heat-treated conditions) and AA7003-T6, with the HAZ displaying a more active behaviour. The difference between the HAZ and unaffected base alloy of AA7003-T6 was +0.014 V. For AA7108-T6, the difference was +0.026 V and for AA7108-T6+PB the difference was +0.017 V. AA7003-T6+PB displayed a less active HAZ compared to the unaffected base alloy by +0.008 V.

Table 9: Summary of potentiodynamic polarization scans

Alloy	**E_{corr} (V) SCE**	**E_{pass} (V) SCE**	**E_{brk} (V) SCE**
ER4043 + PB	-0.744	N/A	N/A
ER5356	-0.881	N/A	N/A
ER5356 + PB	-0.887	N/A	N/A
AA7003-T6	-0.923	-0.907	-0.894
AA7003-T6 HAZ	-0.931	-0.916	-0.908
AA7003-T6+PB	-0.921	-0.905	-0.895
AA7003-T6+PB HAZ	-0.912	-0.891	-0.887
AA7108-T6	-0.959	-0.943	-0.925
AA7108-T6 HAZ	-0.971	-0.954	-0.948
AA7108-T6+PB	-0.945	-0.922	-0.911
AA7108-T6+PB HAZ	-0.952	-0.935	-0.928

4.4 Tensile-shear Testing

The effect of exposure to the GMW-14872 cyclic corrosion test on the tensile-shear properties of each weld configuration were of interest to this investigation. Particularly, its effect on shear-fracture stress and strain was carefully examined. It is important to note again that some results from this section have been previously published [118].

Tensile-shear testing of lap-joint welded configurations of AA7003 and AA7108 resulted in a single fracture mode, in which shear-fracture across the throat of the weld was observed. Additionally, several fracture modes were observed in T-joint welded configurations. Shear-fracture across the weld throat was the primary fracture mode observed in T-joint welded configurations, as shown in Figure 38 a. Figure 38 b and c

depict fracture along the interface of the AA7xxx extruded web/weld and fracture along the interface of the AA6063 extruded flange/weld, respectively. Figure 38 d shows the fourth fracture mode observed in T-joint welded configurations. The nature of this fracture appeared to consist of 2 stages. The first stage was observed to be fracture initiation and propagation along the AA7xxx extruded web/weld interface, as indicated by the red arrow in Figure 38 d. The second stage was defined by fracture propagation through the HAZ of the AA7xxx extruded web until failure.

For the purpose of this investigation, only samples that failed in shear across the weld throat were used for analysis. A more in-depth study is needed to determine the proper formulation(s) with which the stress-strain behaviour of the other three observed fracture modes can be properly quantified. This is beyond the scope of this investigation, which seeks to determine the effect of exposure of AA7xxx welds to the GMW-14872 cyclic corrosion test.

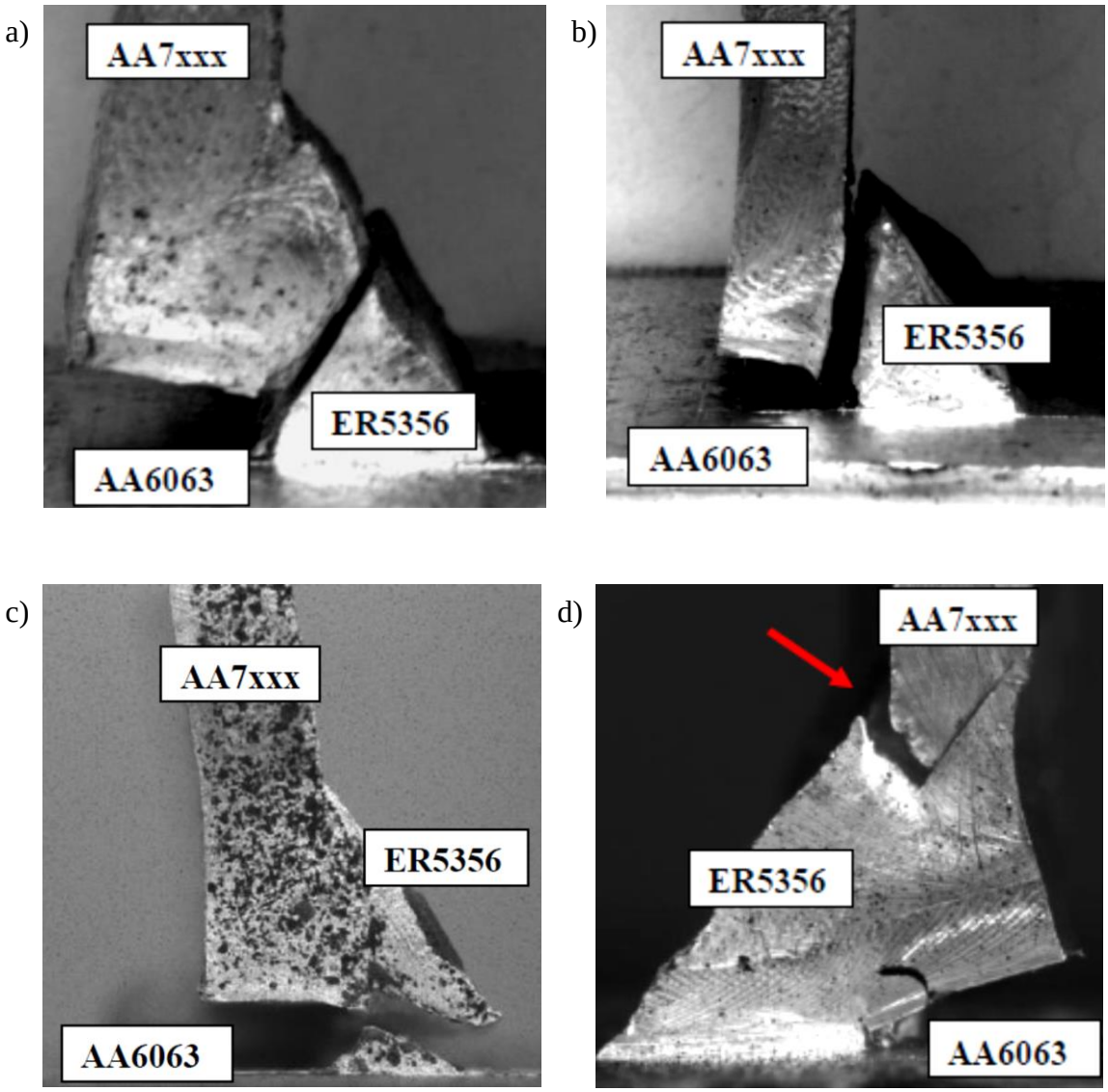

Figure 38: Observed fracture modes in T-joint welded samples (a) shear fracture across the weld throat (configuration H1) (b) fracture along the AA7xxx/ER5356 interface (configuration F3) (c) fracture along the AA6063/ER5356 interface (configuration H3) and (d) fracture in the HAZ of AA7xxx (configuration E1).

Table 10 summarizes the average shear-fracture stress results of the tensile-shear tests. T-joint welded configurations possessing an N/A result for the average shear-fracture stress did not have a single sample that fractured in shear across the weld throat. Three out of fifteen configurations were incomparable due to this condition. In the results obtained from Table 10, a large amount of scatter was observed between samples of the same configuration, which is likely a consequence of weld defects (shown in section 4.1 Weld Joint Characterization) and possible process heterogeneities. All exposed samples except configurations E3 (ER5356/AA7003-T6+PB/⊥) and G1 (ER5356/AA7003-T6/═) exhibited a higher shear-fracture stress than their unexposed counterparts. Small differences (0-15MPa) between shear-fracture stresses of the following exposed and unexposed configurations were observed: A1, A3, C1, C3, H1, I1, and I3. Inspection of the shear-fracture stress ranges (between maximum and minimum values) of exposed and unexposed samples revealed overlap in the shear-fracture stress values between the two test conditions in seven out of fifteen weld configurations. Three out of fifteen weld configurations did not display a maximum/minimum range because only a single sample successfully sheared across the weld throat. There was no overlap in shear-fracture stress ranges observed for samples D3, G1, and G3. This was likely a result of weld defects and heterogeneities. No trend was observed between the two heat-treated conditions.

Table 11 summarizes the average shear-fracture strain results of the tensile-shear tests. Again, configuration results yielding an N/A for the average shear-fracture strain did not have a single sample that fractured in shear across the weld throat. Like the shear-fracture results, shear-strain results contained large amounts of scatter as a probable result

of process heterogeneities and weld defects. Weld configurations A1, D3, G1, H1, H3, and I1 displayed a small difference (0-0.16) in shear-strain between exposed and unexposed weld joints. A3, C3, E3 weld configurations displayed a shear-strain difference of 0.20-0.24 between exposed and unexposed weld joints. A difference in shear-strain of 0.40 was observed between exposed and unexposed welds of configurations C1, G3, and I3. The shear-strain results between the two heat-treated conditions did not display a trend.

Table 10: Summary of average shear-fracture stress

Configuration	**Unexposed Avg. τ_{frac} (MPa)**	**Max/Min (MPa)**	**Exposed Avg. τ_{frac} (MPa)**	**Max/Min (MPa)**
A1	224	276/188	228	229/227
A3	246	259/235	254	267/239
C1	218	229/211	230	233/224
C3	245	249/240	247	252/244
D3	176	192/159	205	223/194
E1	N/A	N/A	N/A	N/A
E3	209	209	142	142
F1	196	206/184	N/A	N/A
F3	212	212/211	N/A	N/A
G1	190	206/173	163	165/162
G3	154	167/148	202	224/177
H1	200	219/186	215	215
H3	165	165	199	208/182
I1	243	240/240	254	267/229
I3	215	239/202	230	235/222

Table 11: summary of average shear-fracture strain.

Configuration	**Unexposed Avg.** ε_{frac}	**Exposed Avg.** ε_{frac}
A1	1.11	1.14
A3	0.93	0.73
C1	1.53	1.13
C3	1.26	1.02
D3	0.80	0.80
E1	N/A	N/A
E3	0.64	0.86
F1	0.70	N/A
F3	0.73	N/A
G1	1.21	1.05
G3	1.20	0.80
H1	0.52	0.53
H3	0.76	0.60
I1	0.98	1.07
I3	1.10	0.70

5.0 Discussion

The overall objective of this body of work was to better understand the influence of welding on the corrosion characteristics of welded Cu-lean AA7003 and AA7108 extrusions. Additionally, the effects of variables such as: heat-treated condition (as-welded T6 vs. as-welded T6+PB), extruded beam alloy Cu composition (AA7003 vs. AA7108), weld filler composition (ER4043 vs. ER5356), weld joint geometry (lap-joint vs. T-joint), and weld direction with respect to extrusion direction (parallel (═) vs. perpendicular (⊥)) were examined. However, to understand the influence of corrosion on the HAZ, the corrosion characteristics of the unaffected base alloy must first be understood.

5.1 Base Alloy Corrosion Behaviour

From the results of the ASTM G-85 A2 corrosion tests, there appears to be a qualitative difference in the pitting corrosion morphologies between AA7003 and AA7108 (Table 8). The greater degree of corrosion was found in AA7003 when compared to AA7108. Large pits that started out in the coarse grained surface layer, that had just begun to penetrate the fine interior grain, were observed in AA7003. The small remnants of the original coarse surface grains suggest that more corrosion of the matrix also took place in AA7003. The presence of small superficial pits that barely penetrated the coarse surface grains in AA7108 were observed. In this case, there were only a few instances where corrosion consumed the coarse grained surface layer and penetrated into

the fine grained interior. These qualitative observations indicate that an increase in the Cu-content of AA7xxx alloys is detrimental to the corrosion behaviour.

However, results of the potentiodynamic polarization scans showed the opposite. An increase in alloy Cu-content was accompanied by a shift of the alloy's anodic polarization curve into a positive direction toward less active values. The observed difference in E_{corr} and E_{brk} between AA7003 and AA7108 was approximately +0.035 V, where AA7003 (0.14 wt% Cu) was found to be less active than AA7108 (0.01 wt% Cu). From this viewpoint it would appear that Cu is beneficial to the corrosion resistance of Cu-bearing AA7xxx alloys.

These conflicting trends were also observed by Meng and Frankel in their investigation into the effect of Cu-content on the corrosion of five AA7xxx alloys [38]. Through anodic potentiodynamic polarization, Meng and Frankel observed that as Cu-content increased, the anodic branch of the alloys' polarization curve shifted in the positive direction, towards less active values. However, by using polarization resistance measurements, Meng and Frankel observed that the polarization resistance of Cu-containing alloys decreases (increasing corrosion susceptibility) with increasing Cu-content. It was proposed that as the Cu-containing alloys corroded, Cu is released into the corrosion solution and then redistributed on the corroding alloy surface as Cu-rich clusters. Because Cu is cathodic, these Cu-rich clusters would promote the cathodic reaction (O_2 reduction), which would subsequently sustain the anodic reaction (Al dissolution) and further perpetuate the corrosion process. With decreasing Cu-content,

Cu-rich cluster formation becomes less prevalent, and therefore less of a cathodic reaction is required to maintain corrosion. This explains why a greater degree of corrosion was observed on AA7003 when compared to AA7108, even though the increased Cu-content of AA7003 showed less active E_{corr} and E_{brk} values.

5.2 HAZ Corrosion

Although there was an observed difference in corrosion behaviour between the unaffected base alloys of welded AA7003 and AA7108, there was no observed difference in the degree of corrosion attack and morphology between the HAZ and the unaffected base alloy of AA7003 and AA7108. This follows the trend observed by Onoro and Ranninger concerning the corrosion of welded AA7015 [113], which showed little to no difference in the corrosion rating and E_{corr} of welded AA7015 exposed to ASTM G34. Interestingly, a very distinct feature was observed in the HAZ of both welded AA7003 and AA7108 post-exposure to the ASTM G85-A2 corrosion test: the appearance of a dual-band of corrosion, as shown in Figure 39 a and b. The two bands of corrosion displayed in Figure 39 are indicated by the colored arrows. The yellow arrow indicates the much larger corrosion band which is immediately adjacent to the weld. The red arrow denotes the thinner corrosion band that is observed at the end of the HAZ. A black arrow between the two bands is shown indicating a thin band of unattacked alloy. While this type of corrosion behaviour in welded AA7xxx alloys has not yet been documented in literature, Mattsson et al. [96] hypothesized that because the HAZ of welded AA7xxx alloys consists of both a solutionized/reverted zone and an over-aged zone, which are

physiochemically different from one another, two zones of differing corrosion characteristics could be observed. The authors hypothesized that the solutionized/reverted zone, immediately adjacent to the weld, would possess the same corrosion behaviour as the unaffected base alloy due to the ability to recover most of the properties lost because of thermal cycling through post-weld natural aging. The over-aged zone's corrosion behaviour would be different due to the inability to recover the initial properties through post-weld natural aging.

a)

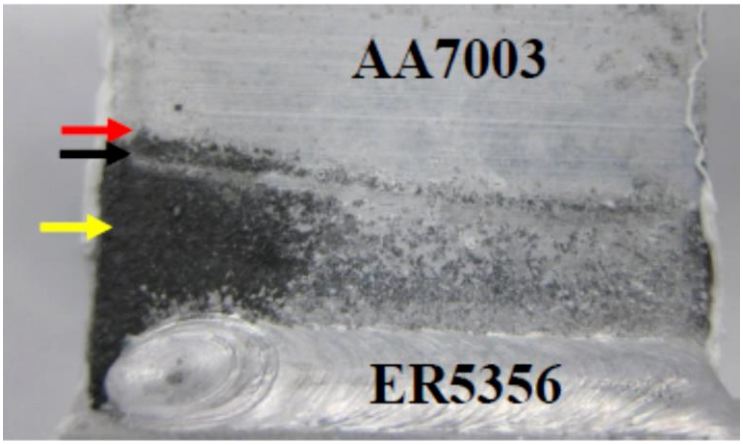

b)

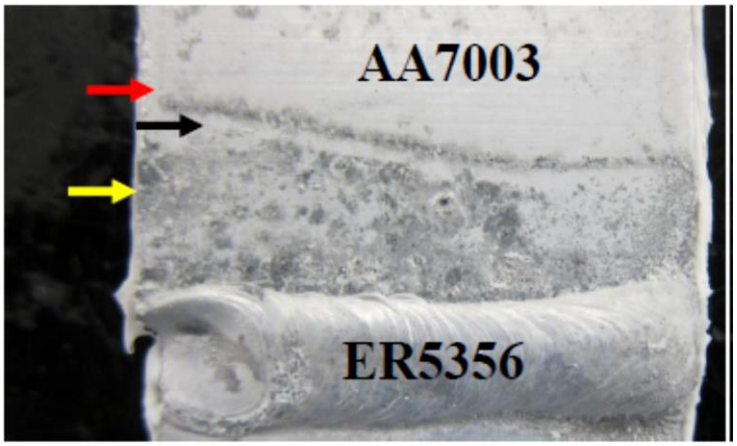

Figure 39: Photographs of (a) T-joint welded configuration H1 and (b) lap joint welded configuration I1 displaying dual corrosion bands denoted by the red and yellow arrows. The black arrow indicates a small uncorroded region between the two corrosion zones.

The appearance of the dual-band corrosion observed in the HAZ of AA7003 and AA7108 can be explained using the proposed microstructural breakdown of the HAZ presented by Nicolas [103]. Nicolas broke the HAZ into three regions: the dissolution + reprecipitation region, the dissolution + coarsening region, and the dissolution region. The dissolution + coarsening region and the dissolution regions make up what is typically termed the over-aged zone in literature. The larger corrosion band immediately adjacent to the weld corresponds to the dissolution + reprecipitation region. In this zone, precipitates are dissolved by the heat input from welding, and GP-zones reprecipitate out upon natural aging. Through natural aging, the microhardness in this region is recovered to similar levels contained in the unaffected base alloy. This causes the dissolution + reprecipitation region and the unaffected base alloy to contain similar amounts of solute (Zn, Mg and Cu) in solid solution. This explanation would allow for both weld zones to display very similar localized corrosion behaviour, as summarized in Table 8. The thin unattacked region between the two corrosion bands corresponds to the dissolution + coarsening region. In this region larger precipitates grow at the expense of smaller ones (typically observed during over-aging), which results in an increase in the Cu-content of the $Mg(Cu, Zn, Al)_2$ precipitates [38]. The increase in the Cu-content of $Mg(Cu, Zn, Al)_2$ precipitates results in a reduced level of Cu-solute within the matrix of this region. As a consequence of the lower levels of Cu retained in solid solution, the region experiences a decreased susceptibility to localized corrosion, resulting in a small thin region of unattacked metal as observed in Figure 40. The thin band of corrosion observed at the outer edge of the HAZ corresponds to the dissolution region. In this region, dissolution

of smaller precipitates takes place. This results in an increase in the Cu, Mg, and Zn solute content of the matrix. However, this partial dissolution of precipitates does not result in a high enough solute content in solid solution to initiate the reprecipitation of GP-zones. Therefore, this slows the kinetics of GP-zone formation in this region [103]. This increase in solute content (Cu) increases the susceptibility of this region to corrode.

Potentiodynamic polarization scans indicated no significant differences between the HAZ and unaffected base alloy samples, despite the fact that the HAZ appeared to consist of dual corrosion bands, as this was likely a result of the metallurgical changes induced by welding. An explanation for this lack of observed effect from the dual corrosion bands on the potentiodynamic polarization scans is the time difference between the ASTM G85-A2 cyclic corrosion test and the potentiodynamic measurements. During the ASTM G85-A2 cyclic corrosion test, the exposed weld configurations spent a total time of 672 h in the fog and humidity stage. This allowed a large amount of time for the dual corrosion bands to distinctly form. This can be compared to the 2 h length of time the potentiodynamic polarization scans took to complete per sample. Therefore the shorter amount of time prevented the dual corrosion bands from distinctly forming.

5.3 Effect of Variables on Corrosion

Paint-Bake Heat-Treatment

The application of a PB heat-treatment to welded AA7003 and AA7108 appeared to influence the apparent microhardness determined HAZ width behaviour of the weld configurations. The welded configurations with an applied PB heat-treatment displayed a decreased apparent HAZ width compared to their as-welded T6 counterparts. However, results of HAZ widths determined post-ASTM G85-A2 testing showed no difference between as-welded T6 and T6+PB heat-treated weld configurations. This discrepancy between the two HAZ width results is likely an outcome of the methodological difference between the two HAZ width determining techniques. The HAZ width post-ASTM G85-A2 testing was determined by simply measuring the distance of the observed HAZ edge from the weld with a ruler. Equal spacing must be maintained between measurement points when using microhardness to determine apparent HAZ width, which makes it very easy to overestimate HAZ width. Thus it is best to use the corrosion determined HAZ widths when discussing HAZ width quantification.

No major differences were observed in the corrosion behaviour between as-welded T6 and as-welded T6+PB heat-treated weld configurations of AA7003 and AA7108. This is likely a consequence of the lack of significant physiochemical differences between the two heat-treated conditions which in turn is a result of either or both of the following factors: sufficiently small time at the prescribed PB temperature or sufficiently low PB temperature. Dehghani et al. [119] Investigated the mechanical

behaviour of AA7075-T6 post-PB(at 150°C and 250°C) at 15 min and 30 min time periods. Their investigation found no change in hardness between PB times at 150° and 250°C, due to the lack of diffusion resulting from the low temperatures and short heat treatment times. Following the results of their investigation, it is plausible that no differences in the corrosion behaviour of AA7003 and AA7108 will be observed when comparing weld configurations with and without the application of a PB heat-treatment.

Welding Direction (Relative to Extrusion Direction)

Both cross-sectioned planes (L-ST & LT-ST) examined in this investigation visually revealed a similar grain size and shape in both the coarse grain surface layer and the fine grain interior. It is therefore unlikely that weld joint orientation would have a significant effect on the corrosion behaviour of welded AA7003 and AA7108.

Joint Geometry

There was no observed difference in the corrosion behaviour between lap-joint and T-joint welded configurations of AA7003 and AA7108. This observation is a result of both joint geometries undergoing the same processing parameters during assembly, which produced similar thermal cycling in the two different joint designs. As a consequence of the two joint geometries experiencing similar thermal cycling, the induced metallurgical changes within the HAZ of both lap-joint and T-joint welded configurations of AA7003 and AA7108 resulted in similar microstructural properties. This led to very similar corrosion behaviours between the two joint geometries.

Filler Alloy Composition

No qualitative difference in the corrosion behaviour between the following weld configurations with differing filler alloy compositions, D3 (ER4043/AA7003-T6+PB/⊥) and A3 (ER5356/AA7003-T6+PB/⊥), was observed. Both weld configurations displayed the same corrosion determined HAZ widths. From the potentiodynamic polarization scans, E_{corr} difference between ER5356 and the HAZ of AA7003 were observed to be .05 V and .025 V, in the as-welded T6 and as-welded T6+PB heat-treated conditions, respectively. Similarly, a much larger E_{corr} difference of .168 V was observed between ER4043 and the HAZ of AA7003 in the as-welded T6+PB condition. The larger observed difference in E_{corr} values between ER4043 and AA7003 indicates a large driving force for galvanic corrosion between the two weld zones, with the ER4043 filler being cathodically protected due to the more active nature of the HAZ of AA7003. No increased corrosion penetration depths were observed near the AA7003 HAZ/ER4043 weld filler interface, a phenomenon typically observed during corrosion of galvanic couples. The observed results indicate that although there is a high driving force for preferential corrosion of the HAZ of welded AA7003, galvanic corrosion is not observed. This occurs because galvanic corrosion of dissimilar alloys is not solely predicted by the difference of E_{corr} values between two alloys. Galvanic corrosion depends on a number of other factors, including: local reactions, metallurgical factors, surface conditions, geometric factors, electrolyte properties, and environmental factors [120].These factors were not examined in this investigation due to its overall large scale.

5.4 GMW-14872 Corrosion

The results of the GMW-14872 cyclic corrosion test revealed discoloration of the test samples with no observed corrosion within the weld material, the HAZ, or the unaffected base alloy of all tested weld configurations. However, several small corrosion pits with a maximum penetration depth of 50 µm into the coarse grained dynamically recrystallized surface layer were observed in the HAZ of T-joint welded configuration F (ER5356/AA7108/⊥). The lack of observed corrosion is a result of the neutral pH of the GMW-14872 solution that was sprayed onto the AA7003 and AA7108 weld configurations. Under neutral pH conditions, Al alloys are resistant to corrosion due to the presence of a thin surface film of $Al_2O_3 \cdot 3H_2O$ which forms upon exposure to air. Due to the very low solubility between pH values of 4-9 of $Al_2O_3 \cdot 3H_2O$, the thin surface film passivates the underlying substrate and protects it from environment around it. Moreover, exposed Al alloys contain a variety of Cl^- ion adsorpation sites on the passive film surface with varying adsorption properties, and only a small amount of these sites are prone to pitting corrosion [59]. The properties of the $Al_2O_3 \cdot 3H_2O$ passive film depend on its structure, which is a function of local composition, defects (both micro and macro), crystal structure, electrolyte composition, pH, and temperature [59]. The few observed pitting corrosion sites in the HAZ of welded AA7108 corresponds to the few local sites which are prone to passive film breakdown under the specific testing conditions.

Due to a lack of observed corrosion on GMW-14872 exposed weld configurations, it is therefore concluded that any difference observed between the tensile-

shear behaviour of exposed and unexposed weld configurations is not a result of expsoure to the GMW-14872 solution. This should be expected, as it has been demonstrated that pre-corrosion exposure followed by tensile testing in an inert environment is not sufficient to produce a degradation in the tensile strength. The stress-intensity factor (K) needed to propogate a crack is much lower during simultaneous exposure to a corrosive solution [121].

5.5 Tensile-Shear Testing

The tensile-shear testing results displayed large amounts of scatter. This made it difficult to elucidated trends when comparing weld configurations with the differing variables under study. The primary reason large amounts of scatter was observed in these results is the presence of varying amounts of defects within the ER4043 and ER5356 weld material which render the results to be meaningless - garbage in, garbage out. The most frequently observed weld defect was porosity. Pores are typically a result of gas (primarily H_2 due to high H_2 solubility in the molten phase of Al) entrapment because of high mositure content, inadequate preperation of weld surface, and excessive flow of sheilding gas [99]. In TIG welded AA2014, AA2021, and AA2219, the presence of pores has been shown to linearly decrease fracture strength as pore area coverage increases, due to the loss of cross-sectional area [122], [123].Pore area coverage of less than 3-5% of the total weld cross-sectional area has been shown to not have any effect on strength in welded Al alloys [124], [125]. Similarly, small amounts of pores (less than 5% of total corss-sectional area coverage) observed in welded AA7039-T6151 with ER5039 filler

have been shown to decrease weld ductility [126]. Furthermore, the spacing of pores has also been found to have an effect on the strength of welded joints. Pores within a distance of less than three diameters of each other have been shown to act as a single large defect with an area equal to the projected area of both pores plus the ligament area (material between both pores) [123].

Cracks within the ER5356 weld material were also observed and should be considered deleterious to overall weld joint performance due to their ability to act as stress concentrators [99]. Cracks within the weld material typically arise from solidification, cooling, and residual stress. Solidification cracks result from the inability of the weld material to withstand the shrinkage strains associated with solidification and cooling, typically occuring within a short period after welding [99]. Al weld filler alloys are good candidates for solidification cracking because of Al's high thermal expansion upon heat-up and large volume change upon soldification. For solidification cracks to occur, strain (in the form of restraint) and a prone microstructure are required. Weld assembly restraints have been shown to increase stress on solidifying weld material [99]. A Mg content of less than 3% in Al-Mg alloys has been observed to increase weld filler crack sensitivity through the formation of brittle Mg rich Al-Mg constitents [99]. Similarly, due to the formation of brittle Mg2Si, ER4xxx filler alloys are not utilized when welding AA7xxx alloys with modest amounts of Mg [99]. Cold cracks, also known as hydrogen-induced cracks, can also occur in Al weld filler material. Cold cracks form due to the diffusion of H_2 to pre-existing weld discontinuities created by minor phase particles and inclusions. The H_2 accumulates at these preferential sites, and the cohesive

energy of the lattice decreases until spontaneous fracture occurs [99]. Due to long H_2 diffusion times, cold cracking is typically observed weeks to months after the completion of the welding operation, which makes it very hard to predict.

Moreover, it is not difficult to conclude that the other weld defects that were observed during this investigation can also influence weld joint behaviour. A study on the lack of penetration [127] into two-sided fillet welded EH-36 steel showed that increasing amounts of penetration increased tensile strength by as much as 37%. Similar results by Rudy and Rupert were observed on TIG welded AA2xxx [122].

The location of weld defects can also be used to predict where fracture may be more likely to occur. If a large amount of a defects (either lack of penetration/fusion or linear porosity) is concentrated along the base alloy or weld filler interface, it is more likely that failure will occur along this interface rather than through the throat of the weld. It is therefore reasonable to state that the different types of failure modes observed in this investigation were a result of an increase in the concentration of weld defects along the failure planes that were not identified as shear fracture across the weld throat.

6 Conclusion

The overall objective of this study was to better understand the localized corrosion behaviour of welded Cu-lean AA7xxx alloys. This study utilized welded AA7003 and AA7108 extrusions and investigated the effects of the following processing variables: extrusion alloy Cu composition, heat-treatment condition (as-welded T6 vs. As-welded T6+PB), weld filler composition (ER4043 vs. ER5356), weld joint geometry (lap-joint vs. T-joint), and weld direction with respect to extrusion direction (parallel (═) vs. perpendicular (⊥)).

The influence of the weld process and the aforementioned processing variables on the resultant microstructure of the various weld regions was characterized using optical light microscopy and microhardness measurements. Major conclusions from this part of the study were:

- The extrusion process yielded a dual-grain structure consisting of a coarse-grained dynamically recrystallized surface layer and a fibrous fine-grained interior. Little to no differences were observed between the grain sizes of the HAZ and the unaffected base alloys, indicating that the thermal heat input from welding does not affect the grain size in the HAZ. No effect on grain size was observed from any of the processing variables of interest.
- Large amounts of macroscopic defects were observed in cross-sections of the weld filler of the various weld configurations. Porosity (scattered and linear) and cracking were the predominantly observed defects. T-joint welded configurations

also possessed penetration (lack of penetration and over-penetration) and weld root bridging defects. Lap-joint welded configurations displayed weld filler overlap beyond the weld toe.

- Microhardness measurement revealed the presence of an apparent HAZ immediately adjacent to the weld filler. The region of the apparent HAZ immediately adjacent to the weld displayed an increase in microhardness to that of the unaffected base alloy, a result of natural aging. The end of the apparent HAZ was denoted by a small region of softening until the unaffected base alloy was reached. No effects from the processing variables of interest were observed.

The influence of the processing variables of interest on the corrosion behaviour of welded AA7003 and AA7108 was investigated using accelerated cyclic salt spray testing. Tests were conducted according to the procedures outlined in the ASTM G85-A2 and GMW-14872 standards. Major conclusions drawn from this part of study are:

- Weld configurations exposed to ASTM G85-A2 displayed a clearly marked HAZ adjacent to the weld material, ranging in width from 6-12 mm. A dual corrosion band HAZ structure, consisting of a single large corrosion band immediately adjacent to the weld and a thin band of corrosion denoting the end of the HAZ, was observed. The two corrosion bands were separated by a thin band of unattacked metal. The appearance of dual corrosion bands is a result of metallurgically differing regions which arose from the unique thermal histories

locally occurring at differing distances from the weld region. The HAZ and unaffected base alloy displayed the same corrosion morphology.

- Differing corrosion behaviour was observed between AA7003 and AA7108. AA7003 displayed a greater degree of pitting corrosion with penetration reaching the fibrous fine grained interior. AA7108 displayed the presence of small corrosion pits penetrating the recrystallized surface layer, and only a few instances of penetration into the fine-grained interior were observed. The observed corrosion differences are a result of the different Cu compositions between the two alloys of interest. The higher Cu content found in AA7003 decreased the corrosion resistance of the alloy by promoting the cathodic reaction (O2 reduction), which in turn sustained the anodic reaction (Al dissolution), and enhanced corrosion. Conversely, the lack of Cu in AA7108 reduced the cathodic reaction which in turn reduced the anodic reaction, and decreased the amount of observed corrosion.
- Exposure to GMW-14872 revealed slight discoloration on all weld configurations. The only corrosion was observed in the form of small pits, penetrating 30-50 μm into the recrystallized surface layer of both T-joint welded F (ER5356/AA7108/ ⊥) configurations. The lack of observed corrosion from the GMW-14872 cyclic corrosion test is a result of the neutral pH of the corrosion solution used, because in neutral environments Al alloys possess a passive surface film of $Al_2O_3 \cdot 3H_2O$ which greatly increases corrosion resistance. The small amounts of pitting observed on both welded F configurations correspond to pitting prone sites within

the passive film that result from heterogeneities within the passive film's structure.

In this investigation, an examination of the effects of the various processing variables was undertaken, and the electrochemical behaviour of the different weld regions by means of potentiodynamic polarization measurements was assessed. The major results from this body of work are:

- AA7108 was found to be more active than AA7003 due its lower Cu content. Similarly, ER4043 was observed to be less active than ER5356, because the less active Si acted as the main alloying constituent in AA4xxx alloys, and the more active Mg acted as the primary alloying element in AA5xxx alloys. Although a large difference (+ .168 V) in E_{corr} values was observed between ER4043 and the HAZ of AA7003, which indicated a large driving force for galvanic corrosion, no signs of galvanic corrosion were observed upon completion of ASTM G85-A2 cyclic corrosion testing.
- Although the observed HAZ consisted of dual corrosion bands, the HAZ and unaffected base alloy of welded AA7003 and AA7108 did not display any significant differences, staying consistent with the results of the ASTM G85-A2 cyclic corrosion test. This is a result of the large difference in exposure times between the two methodologies; the large exposure times of the ASTM G85-A2 cyclic corrosion test allowed for the formation of distinguishably separate corrosion bands.

- No significant difference was observed in the in E_{corr} and E_{brk} values of the as-welded T6 and as-welded T6+PB weld configurations. This is due to the sufficiently low PB temperatures and heat-treatment lengths.

The tensile-shear behaviour of welded AA7003 and AA7108 exposed and unexposed to the GMW-14872 cyclic corrosion test was investigated using custom made tensile jigs. Major conclusions drawn from this part of the study were:

- Several shear fracture modes were observed: fracture across the weld throat, fracture along the AA7xxx/ER5356 interface, fracture along the AA6063/ER5356 interface, and fracture in the HAZ of AA7xxx (T-joint welded configurations only). All fracture modes aside from fracturing across the weld throat are a result of high concentrations of weld defects (linear porosity, lack of fusion or lack of penetration, and over penetration) along the fracture planes.
- No significant effect was observed on the shear-fracture stress and strain values from the exposure of welded AA7003 and AA7018 configurations to the GMW-14872 cyclic corrosion test. This was due to the existence of a passive layer of $Al_2O_3 \cdot 3H_2O$ which protected the weld configurations in the neutral pH environment.
- The effects of the various process variables of interest on the tensile-shear behaviour of the welded alloys was difficult to elucidate due the large number of observed weld defects, which introduced a substantial amout of scatter into the results.

These conclusions have several important implications with respect to the processing and utilization of Cu-lean AA7xxx extrusions for the fabrication of automotive bumper assemblies. Firstly, after prolonged periods of natural aging, followed by exposure to a very agressive environment (ASTM G85-A2 and potentiodynamic polarization solution), the HAZ and unaffected base alloy of AA7003 and AA7108 both displayed similar corrosion behaviours. This indicates that prolonged natural aging induces physiochemical changes within the HAZ which can lead to similar properties (microhardness and corrosion) that are observed in the unaffected base alloy. Thus, this makes it easier to predict the corrosion behaviour of the welded assembly. Second, the lack of any significant difference in the corrosion behaviour between as-welded T6 and as-welded T6+PB weld configurations demonstrates that downstream manufacturing heat-treatment processes can have the potential to not effect the corrosion performance of the assembled bumper system. Thirdly, exposure to an environment which closely mimics typical road conditions (GMW-14872) revealed only a handful of small corrosion pits on AA7108, making Cu-lean AA7xxx alloys a suitable replacement for AA6xxx, which are typically found in current welded bumper assemblies. Lastly, the presence of many weld defects can greatly influence the mechanical behaviour by introducing large variance into the results, as well as adding unpredictibility to the fracture mechanics of the weld joint. Therefore, it is of utmost importance that diligence is taken to adhere to proper welding techniques and procedures to reduce the presence of determintal weld defects and improve weld joint quality.

Bibliography

[1] A.H Clausen, O.S Hopperstad, and M Langseth, "Stretch Bending of Aluminium Extrusions for Car Bumpers," *Journal of Materials Processing Technology*, vol. 102, pp. 241-248, May 2000.

[2] Y Chen, K.O Pedersen, A.H Clausen, and O.S Hopperstad, "An Experimental Study on the Dynamic Fracture of Extruded AA6xxx and AA7xxx Aluminium Alloys," *Materials Science and Engineering A*, vol. 523, pp. 253-262, Oct 2009.

[3] K.G Kent, "Weldable Al:Zn:Mg Alloys," *Metallurgical Reviews*, vol. 15, pp. 135-146, Jan 1970.

[4] M.C Reboul, B Dubost, and M Lashermes, "The Stress Corrosion Susceptibility of Aluminium Alloy 7020 Welded Sheets," *Corrosion Science*, vol. 25, pp. 999-1018, Nov 1985.

[5] M.J. Robsinson and N.C. Jackson, "Exfoliation Corrosion of High Strength Al-Cu-Mg Alloys: Effect of Grain Structure," *British Corrosion Journal*, vol. 34, pp. 45-49, 1999.

[6] M.J. Robinson, "Mathematical Modelling of Exfoliation Corrosion in High Strength Aluminum Alloys," *Corrosion Science*, vol. 22, pp. 775-790, 1982.

[7] J. Wloka, T. Hack, and S. Virtanen, "Influence of Temper and Surface Condition on the Exfoliation Behaviour of High Strength Al-Zn-Mg-Cu Alloys," *Corrosion Science* , vol. 49, pp. 1437-1449, 2007.

[8] B.W. Lifka and D.O. Sprowls, "Relationship of Accelerated Test Methods for Exfoliation Resistance in 7XXX Series Aluminum Alloys with Exposure to a Seacoast Environment," in *Corrosion in Natural Environments*, 1973, pp. 306-333.

[9] S. Lee and B.W. Lifka, "Modification of the EXCO Test Method for Exfoliation Corrosion Susceptibility in 7xxx, 2xxx, and Aluminum-Lithium Alloys," in *New Methods for Corrosion Testing of Aluminum Alloys: ASTM STP 1134*, West Conshohocken, PA, 1992, pp. 1-19.

[10] J.F. Li, Z.Q. Jia, C.X. Li, N. Birbilis, and C.Cai, "Exfoliation Corrosion of 7150 Al Alloy with Various Tempers and its Electrochemical Impedence Spectroscopy in EXCO Solution," *Material Corrosion*, vol. 60, pp. 407-414, 2009.

[11] T. Ramgopal, P.I. Gouma, and G.S. Frankel, "Role of Grain-Boundary Precipitates and Solute-Depleted Zone on the Intergranular Corrosion of Aluminum Alloy 7150," *Corrosion*, vol. 58, pp. 687-697, 2002.

[12] T. Ramgopal, P. Schmutz, and G.S. Frankel, "Electrochemical Behavior of Thin Film Analogs of Mg(Zn,Cu,Al)2," *Journal of the Electrochemical Society*, vol. 148, p. B348, 2001.

[13] C. Kirshnan, Localized Corrosion Behaviour of Cu-lean AA7003 Extrusions, 2011, MASc Thesis, McMAster University. Hamilton, Ontario, Canada.

[14] M.B Shumaker, R.A Kelsey, D.O Sprowls, and J.G Williamson, "Evaluation of Various Techniques for Stress Corrosion Testing of Welded Aluminum Alloys," in *Stress Corrosion Testing: ASTM-STP 425*, Philadelphia, PA, 1967, pp. 317-341.

[15] R Grauer and E Wiedmer, "Polarization Measurements on Short-Circuit Elements and Welded Joints in Aluminum Alloys," *Werkstoffe Und Korrosion*, vol. 31, pp. 45-48, Jan 1980.

[16] C.D.S Tuck, "The Use of Micro-Electrodes in the Study of Localised Corrosion in Aluminium Alloys," *Corrosion Science* , vol. 23, pp. 379-389, Apr 1983.

[17] J.B., Mahoney, M.W., Pollock, G., and Rhodes, G.C. Lumsden, "Intergranular Corrosion Following Friction Stir Welding of Aluminum Alloy 7075-T651," *Corrosion*, vol. 55, pp. 1127-1136, Dec 1999.

[18] D.A. Wadeson et al., "Corrosion Behaviour of Friction Stir Welded AA7108 T79 Aluminium Alloy," *Corrosion Science* , vol. 48, pp. 887-897, Apr 2006.

[19] O. Hatamleh, P.M. Singh, and H. Garmestani, "Corrosion Susceptibility of Peened Friction Stir Welded 7075 Aluminum Alloy Joints ," *Corrosion Science*, vol. 51, pp. 135-143, Jan 2009.

[20] I. Polmear, "The Age Characteristics of Ternary Aluminum-Zinc-Magnesium Alloys," *Journal of the Institute of Metals*, vol. 86, pp. 113-120, Nov 1957.

[21] T. Sanders and J. Staley, "Review of Fatigue and Fracture Research on High Strength Aluminum Alloys," in *ASM Science Seminar*, St. Louis, MO, Oct 1978, pp. 467-522.

[22] I.J Polmear, *Light Alloys: Metallurgy of Light Alloys*, 3rd ed. Australia: John Wiley & Sons , 1995.

[23] J. Lendvai, "Precipitation and Strengthening in Aluminum Alloys," *Materials Science Forum*, vol. 217-222, pp. 43-56, 1996.

[24] S.K Maloney, I.J Polmear, and S.P Ringer, "The Chemistry in an Aged Al-2.1Zn-1.7Mg at% Alloy," *Scripta Materialia*, vol. 41, pp. 1031-1038, 1999.

[25] T. Engdahl, V. Hansen, P.J. Warren, and K. Stiller, "Investigation of Fine Scale Precipitates in Al–Zn–Mg Alloys after Various Heat Treatments," *Materials Science and Engineering: A*, vol. 327, pp. 59-64, 2002.

[26] H. Loffler, I. Kovacs, and J. Levandi, "Review Decomposition Process in Al-Zn-Mg Alloys," *Journal of Material Science*, vol. 18, pp. 2215-2240, 1983.

[27] D.A. Porter and K.E. Easterling, *Phase Transformations in Metals and Alloys*, 2nd ed. England: CRC Press, 1992.

[28] S.R. Ortner, C.R.M. Grovenor, and B.A. Shollock, "On the Structure and Composition of GP Zones in High Purity AlZnMg Alloys," *Scripta Metallurgica*, vol. 22, pp. 839-842, 1988.

[29] K. Hono, N. Sano, and T. Sakurai, "Quantitative Atom Probe Analysis of Some Aluminum Alloys," *Surface Science*, vol. 266, pp. 350-357, 1992.

[30] K. Stiller, P.J. Warren, V. Hansen, J. Angenete, and J. Gjonnes, "Investigation of Precipitation in an Al-Zn-Mg Alloy after Two-Step Ageing Treatment at 100 C and 150 C," *Materials Science and Engineering A*, vol. 270, pp. 55-63, 1999.

[31] S.S. Brenne, J. Kowalik, and M.J. Hua, "FIM/Atom Probe Analysis of a Heat Treated 7150 Aluminum Alloy," *Surface Science*, vol. 246, pp. 210-217, 1991.

[32] P.J. Warren, C.R.M. Grovenor, and J.S. Crompton, "Field-Ion Microscope/Atom-Probe Analysis of Effect of RRA Heat Treatment on the Matrix Strengthening Precipitates in Alloy Al-7150," *Surface Science*, vol. 266, pp. 342-349, 1992.

[33] A. Deschamps, F. Livet, and Y. Brechet, "Influence of Predeformation on Ageing In An Al-Zn-Mg Alloy I: Microstructure Evolution and Mechanical Properties," *Acta Materialia*, vol. 47, p. 281, 1999.

[34] A. Deschamps et al., "A Comparative Study of Precipitate Composition and Volume Fraction in an Al-Zn-Mg Alloy Using Tomographic Atom Probe and Small-Angle X-Ray Scattering," *Philosophical Magazine A*, vol. 81, pp. 2391-2414, 2001.

[35] J.K. Park and A.J. Ardell, "Microstructure of the Commercial 7075 Al Alloy in the T651 and T7 Tempers," *Metallurgical Trasnactions*, vol. 14A, pp. 1957-1965, 1983.

[36] J.K. Park and A.J. Ardell, "Precipitation at Grain Boundaries in the Commercial Alloy Al 7075," *Acta Metallurgica*, vol. 34, pp. 2399-2409, 1986.

[37] L.S Mondolfo, N.A Gjostein, and D.W. Lewison, "Structural Changes During the Ageing of an Al-Zn-Mg Alloy," *Transactions AIME*, vol. 206, pp. 1378-1385, 1956.

[38] Q. Meng and G.S. Frankel, "Effect of Cu Content on Corrosion Behavior of 7xxx Series Aluminunm Alloys," *Journal of The Electrochemical Society*, vol. 151, pp. B271-B283, 2004.

[39] J.D. Embury and R.B. Nicholson, "The Nucleation of Precipitates: The System Al-Zn-Mg," *Acta Metallurgica*, vol. 13, pp. 403-417, 1965.

[40] M. Raghavan, "Microanalysis of Precipitate Free Zones (PFZ) in Al-Zn-Mg and Cu-Ni-Nb Alloys," *Metallurgical Transactions A*, vol. 11A, pp. 993-999, 1980.

[41] J.K. Park and A.J. Ardell, "Microchemical Analysis of Precipitate Free Zones in 7075-Al in the T6, T7 and RRA Tempers," *Acta Metallurgica et Materialia*, vol. 39, pp. 591-598, 1991.

[42] M. Tanaka, R. Dif, and T. Warner, "Chemical Composition Profiles across Grain Boundaries in T6, T79 and T76 Tempered AA7449 Alloy," *Materials Science Forum*, vol. 396-402, pp. 1449-1454, 2002.

[43] Y.E Wu and Y.T Wang, "The Effect of Filler Metal and Postwelding Heat Treatment on Meachanical Properties of Al-Zn-Mg Alloy Weldments," *Journal of Materials Engineering and Performance*, vol. 19, pp. 1362-1369, Dec 2010.

[44] R.G. Hamerton, H. Cama, and M.W. Meredith, "Development of the Coarse Intermetallic Particle Population in Wrought Aluminium Alloys During Ingot Casting and Thermo-mechanical Processing," in *Aluminium Alloys: Their Physical and Mechanical Properties Parts 1-3*, Charlottesville, VA, 2000, pp. 143-155.

[45] A.K. Mukhopadhyay, V.V. Rama Rao, and C.R. Chakravorty, "Influence of Constituent Particles on the Quality of Hard Anodic Coatings on Fully Heat Treated AA7075 Extrusion Products," *Materials Science Forum*, vol. 217-222, pp. 1617-1622, 1996.

[46] R. Ayer, J.Y. Koo, J.W. Steeds, and B.K. Park, "Microanalytical Study of the Heterogeneous Phases in Commercial Al-Zn-Mg-Cu Alloys," *Metallurgical and Materials Transactions A*, vol. 16A, pp. 1925-1936, 1985.

[47] J.A. Wert, "Identification of Precipitates in 7075 Al after High-Temperature Aging," *Scripta Metallurgica*, vol. 15, pp. 445-447, 1981.

[48] M. Gao, C.R. Feng, and R.P. Wei, "An Analytical Electron Microscopy Study of Constituent Particles in Commercial AA7075-T6 and AA2024-T3," *Metallurgical and Materials Transactions A*, vol. 29A, pp. 1145-1151, 1998.

[49] H.H. Jo, H. Cho, K.W. Lee, and Y.J. Kim, "Extrudability Improvement and Energy Consumption Estimation in Al Extrusion Process of a 7003 Alloy," *Journal of Materials Processing Technology*, vol. 130-131, pp. 407-410, 2002.

[50] R. Poganitsch, L. Sigl, F. Jeglitsch, and F. Kutner, "Intermetallic Compounds in High Strength Al-Zn-Mg-Cu Alloys," *Aluminium Dusseldorf*, vol. 57, pp. 804-807, 1981.

[51] D.S. Park and S.W. Nam, "Effects of Manganese Dispersoid on the Mechanical Properties in Al-Zn-Mg Alloys," *Journal of Material Science*, vol. 30, pp. 1313-1320, 1995.

[52] G.E. Totten and D.S. MacKenzie, *Handbook of Aluminum*. New York, USA: Marcel Dekker Inc., 2003.

[53] L.M. Wu, W.H. Wang, Y.F. Hsu, and S. Trong, "Effects of Homogenization Treatment on Recrystallization Behavior and Dispersoid Distribution in an Al-Zn-Mg-Sc-Zr Alloy," *Journal of Alloys and Compounds*, vol. 456, pp. 163-169, 2008.

[54] J.D. Robson, "Optimizing the Homogenization of Zirconium Containing Commercial Aluminum Alloys Using a Novel Process Model," *Materials Science and Engineering A*, vol. 338, pp. 219-229, 2002.

[55] A. Deschamps and Y. Brechet, "Influence of Quench and Heating Rates on the Ageing Response of Al-Zn-Mg-(Zr) Alloy," *Materials Science and Engineering A*, vol. 251, pp. 200-207, 1998.

[56] I. Westermann, A.L. Haugstad, Y. Langsrud, and K. Marthinsen, "Effect of Quenching Rate on Microstructure and Mechanical Properties of Commercial AA7108 Aluminium Alloy," *Transactions of Nonferrous Metals Society of China (English Edition)*, vol. 22, pp. 1872-1877, 2012.

[57] A.K. Mukhopadhyay, Q.B. Yang, and S.R. Singh, "The Influence of Zirconium on the Early Stages of Ageing of a Ternary Al-Zn-Mg Alloy," *Acta Metallurgica et Materialia*, vol. 42, pp. 3083-3091, 1994.

[58] D.A. Jones, *Principles and Prevention of Corrosion*, 2nd ed. Upper Saddle River, NJ, USA: Prentice Hall, 1996.

[59] Z. Szklarska-Smialowska, "Pitting Corrosion of Aluminum," *Corrosion Science*, vol. 41, pp. 1743-1767, 1999.

[60] C.M. Liao, J.M. Olive, M. Gao, and R.P. Wei, "In-Situ Monitoring of Pitting Corrosion in Aluminum Alloy 2024," *Corrosion* , vol. 54, pp. 451-458, 1998.

[61] E. McCafferty, "General Relations Regarding Graph Theory and the Passivity of Binary Alloys," *Journal of the Electrochemical Society*, vol. 150, pp. B238-B247, 2003.

[62] N. Birbilis and R.G. Buchheit, "Electrochemical Characteristics of Intermetallic Phases in Aluminum Alloys," *Journal of the Electrochemical Society*, vol. 152, pp. B140-B151, 2005.

[63] R.G. Buchheit et al., "The Electrochemistry of Intermetallic Particles and Localized Corrosion in Al Alloys," *Journal of the Minerals, Metals and Materials Society*, vol. 53, p. 29, 2001.

[64] M. Buchler, T. Watari, and W.H. Smyrl, "Investigation of the Initiation of Localized Corrosion on Aluminum Alloys by Using Fluorescence Microscopy," *Corrosion Science*, vol. 42, pp. 1661-1668, 2000.

[65] G.O. Ilevbare, O. Schneider, R.G. Kelly, and J.R Scully, "In Situ Confocal Laser Scanning Microscopy of AA 2024-T3 Corrosion Metrology II. Trench Formation Around Particles," *Journal of the Electrochemical Society*, vol. 151, pp. B465-B472, 2004.

[66] G.O. Ilevbare, O. Schneider, R.G. Kelly, and J.R. Scully, "In Situ Confocal Laser Scanning Microscopy of AA 2024-T3 Corrosion Metrology I. Localized Corrosion of Particles," *Journal of the Electrochemical Society*, vol. 151, pp. B453-B464, 2004.

[67] N. Birilis, M.K. Cavanaugh, and R.G. Buchheit, "Electrochemical Behavior and Localized Corrosion Associated with Al7Cu2Fe Particles in Aluminum Alloy 7075-T651," *Corrosion Science* , vol. 48, pp. 4202-4215, 2006.

[68] J.R.T. Leclère and C.R. Newman, "Self-Regulation of the Cathodic Reaction Kinetics During Corrosion of AlCu Alloys," *Journal of the Electrochemical Society*, vol. 149, pp. B52-B56, 2002.

[69] J.R. Scully, T.O. Knight, R.G. Buchheit, and D.E. Peebles, "Electrochemical Characteristics of the Al2Cu, Al3Ta and Al3Zr Intermetallic Phases and Their Relevancy to the Localized Corrosion of Al Alloys," *Corrosion Science*, vol. 35, pp. 185-195, 1992.

[70] F. Andreatta, H. Terryn, and J.H.W. de Wit, "Corrosion Behaviour of Different Tempers of AA7075 Aluminum Alloy," *Electrochimica Acta*, vol. 49, pp. 2851-2862, 2004.

[71] R.P. Wei, C.M. Liao, and M. Gao, "Transmission Electron Microscopy Study of Constituent-Particle-Induced Corrosion in 7075-T6 and 2024-T3 Aluminum Alloys," *Metallurgical and Materials Transactions A*, vol. 29A, pp. 1153-1160, 1998.

[72] S. Dey, M.K. Gunjan, and I. Chattoraj, "The Effect of Temper on the Distribution of Pits in AA7075 Alloys," *Corrosion Science* , vol. 50, pp. 2895-2901, 2008.

[73] G.S. Chen, M. Gao, and R.P. Wei, "Microconstituent-Induced Pitting Corrosion in Aluminum Alloy 2024-T3," *Corrosion*, vol. 52, pp. 8-15, 1996.

[74] K. Nisancioglu, "Electrochemical Behavior of Aluminum-Base Intermetallics Containing Iron," *Journal of the Electrochemical Society*, vol. 137, pp. 69-77, 1990.

[75] R.G. Buchheit, L.P. Montes, M.A. Martinez, J. Michael, and P.F. Hlava, "The Electrochemical Characteristics of Bulk-Synthesized Al2CuMg," *Journal of the Electrochemical Society*, vol. 146, pp. 4424-4428, 1999.

[76] R.G. Buchheit, M.A. Martinez, and L.P. Montes, "Evidence for Cu Ion Formation by Dissolution and Dealloying the Al2CuMg Intermetallic Compound in Rotating Ring-Disk Collection Experiments," *Journal of the Electrochemical Society*, vol. 147, pp. 119-124, 2000.

[77] E.H. Dix and H.H. Richardson, "Equilibrium Relations in Aluminum-Copper Alloys of High Purity," *Transactions of the American Institute of Mining, Metallurgical, and Petroleum Engineers*, vol. 73, pp. 560-580, 1926.

[78] R.H. Brown and R.B. Mears, "The Electrochemistry of Corrosion," *Transactions of the Electrochemical Society*, vol. 74, pp. 495-517, 1938.

[79] M.S. Hunter, G.R. Frank, and D.L. Robinson, "Mechanisms of 2024 Alloy as Revealed by Electron Microscope," in *Proceedings of the Second International Congress on Metallic Corrosion*, 1963, p. 102.

[80] E.H. Dix, "Aluminum-Zinc-Magnesium Alloys - Their Developement and Commercial Production," in *Transactions of the American Society for Metals*, vol. 42, 1950, p. 1057.

[81] W.L. Fink and L.A. Wiley, *Metals Technology*, vol. 14, no. 8, 1947.

[82] M.S. Hunter and D.L. Robinson, in *International Conference in Fundamental Aspects of Stress-Corrosion Cracking*, 1968, p. 495.

[83] B.W. Lifka and D.O. Sprowls, "Significance of Intergranular Corrosion in High-Strength Aluminum Alloy Products," in *Localized Corrosion- Cause of Metal Failure STP 516*, 1971, pp. 120-144.

[84] J.R. Galvele and S.M. De Micheli, "Mechanism of Intergranular Corrosion of Al-Cu Alloys," *Corrosion Science*, vol. 10, pp. 795-807, 1970.

[85] S. Maitra and G.C. English, "Mechanism of Localized Corrosion of 7075 Alloy Plate," *Metallurgical Trasnactions A*, vol. 12A, pp. 535-541, 1981.

[86] T.S. Huang and G.S. Frankel, "Effects of Temper and Potential on Localized Corrosion Kinetics of Aluminum Alloy 7075," *Corrosion*, vol. 63, pp. 731-743, 2007.

[87] W. Zhang and G.S Frankel, "Transitions Between Pitting and Intergranular Corrosion in AA2024," *Electrochimica Acta*, vol. 48, pp. 1193-1210, 2003.

[88] T. Huang, X. Zhao, G.S. Frankel, B.Zoofan, and S.Rokhlin, "Growth Kinetics of Intergranular and Exfoliation Corrosion in AA7178," in *Proceedings from the Tri-Service Corrosion Conference*, 2003.

[89] Z. Zhao and G.S. Frankel, "On the First Breakdown in AA7075-T6," *Corrosion Science*, vol. 49, pp. 3064-3088, 2007.

[90] R.G. Buchheit, J.P. Moran, and G.E. Stoner, "Localized Corrosion Behavior of Alloy 2090-The Role of Microstructural Heterogeneity," *Corrosion*, vol. 46, pp. 610-617, 1990.

[91] M.J. Robinson, "The Role of Wedging Stresses in the Exfoliation Corrosion of High Strength Aluminum Alloys," *Corrosion Science*, vol. 23, pp. 887-899, 1983.

[92] D. McNaughtan, M. Worsfold, and M.J. Robinson, "Corrosion Product Force Measurements in the Study of Exfoliation and Stress Corrosion Cracking in High Strength Aluminum Alloys ," *Corrosion Science* , vol. 45, pp. 2377-2389, 2003.

[93] T. Marlaud, B. Malki, A. Deschamps, and B. Baroux, "Electrochemical Aspects of Exfoliation Corrosion of Aluminum Alloys: the Effects of Heat Treatment," *Corrosion Science*, vol. 53, pp. 1394-1400, 2011.

[94] T. Marlaud, B. Malki, C. Henon, A. Deschamps, and B. Baroux, "Relationship Between Alloy Composition, Microstrcuture and Exfoliation Corrosion in Al-Zn-Mg-Cu Alloys," *Corrosion Science*, vol. 53, pp. 3139-3149, 2011.

[95] G. Deshais and S.B. Newcomb, "Anodic Dissolution: Its Characterization and Relevance to Corrosion and Stress Corrosion Cracking in 7xxx Alloys," in *Proceedings of the International Symposium on Aluminum Surface Science and Technology*, 2000, pp. 277-282.

[96] E. Mattsson, L.O. Gullman, L. Knutsson, R. Sundberg, and B. Thundal, "Mechanism of Exfoliation (Layer Corrosion) of Al-5%Zn-1%Mg," *British Corrosion Journal*, vol. 6, pp. 73-83, 1971.

[97] D.G. Evans and P.W. Jeffrey, "Exfoliation Corrosion of AlZnMg Alloys ," in *NACE-3: U.R. Evans Conference on Localized Corrosion*, 1974, pp. 614-622.

[98] R. Braun, "Exfoliation Corrosion Testing of Aluminum Alloys," *British Corrosion Journal*, vol. 30, pp. 203-208, 1995.

[99] *ASM Handbook Volume 6: Welding, Brazing and Soldering*, 10th ed. USA: ASM International, 1993.

[100] S.A. David, S.S. Babu, and J.M. Vitek, "Welding: Solidification and Microstructure," *JOM*, vol. 55, pp. 14-20, 2003.

[101] B. Bjorneklett, O. Grong, A.O. Kluken, and O. Jensurd, "Embrittlement Phenomena in the HAZ of Al-Zn-Mg Weldments," *Materials Science Forum*, vol. 217-222, pp. 1527-1532, 1996.

[102] A. Romeyn, "Welding Al-Zn-Mg (7xxx Series) Alloys - A Literature Review," Department of Defence , Melbourne, Australia, 1983.

[103] M. Nicolas, Precipitation Evolution in an Al-Zn-Mg Alloy During Non-Isothermal Heat Treatments and in the Heat-Affected Zone of Welded Joints, 2002, PhD Thesis, Institut National Polytechnique de Grenoble, France.

[104] T. Ma and G. den Ouden, "Heat-affected Zone Softening During Arc Welding of Al-Zn-Mg Alloys," *International Journal for the Joining of Materials*, vol. 8, pp. 105-110, 1996.

[105] A.O. Kluken O.R. Myher, S. Klokkehaug, H.G. Fjoer, and O. Grong, "Modelling of Microstructure Evolution and Residual Stresses in Processing and Welding of 6082 and 7108 Aluminum Alloys," *ASM Proceedings of the International Conference: Trends in Welding Research*, pp. 233-238, 1998.

[106] B.I. Bjorneklett, O. Grong, O.R. Myhr, and A.O. Kluken, "A Process Model for the Heat-Affected Zone Microstructure Evolution in Al-Zn-Mg Weldments," *Metallurgical and Materials Transactions A*, vol. 30A, pp. 2667-2677, 1999.

[107] G. Fu, F. Tian, and H. Wang, "Studies of Softening of Heat-Affected Zone of Pulsed-Current GMA Welded Al-Zn-Mg Alloy," *Journal of Materials Processing Technology*, vol. 180, pp. 216-220, 2006.

[108] R.Y. Hwang and C.P. Chou, "The Study on Microstructural and Mechanical Properties of Weld Heat Affected Zone of 7075-T651 Aluminum Alloy," *Scripta Materialia*, vol. 38, pp. 215-221, 1998.

[109] ASM International, *Corrosion of Aluminum and Aluminum Alloys*, J.R. Davis, Ed., 1999.

[110] T. Enjo and T. Kuroda, "Effect of Copper Addition on Corrosion Resistance of Commercial Al-Zn-Mg Welds," *Transactions of Japanese Welding Research Institute*, vol. 14, pp. 77-82, 1985.

[111] T. Kuroda, S. Kanamitsu, and T. Enjo, "Corrosion Characteristics in Weld Heat-Affected Zone of Al-Zn-Mg Alloy," *Transaction of Japanese Welding Research Institute*, vol. 19, pp. 87-92, 1990.

[112] X. Wang, J. Zhao, and G. Gou, "Research on Salt For Corrosion Behavior of Welded Joint of 7N01-T4 Aluminum Alloy for High-Speed Train," *Adavanced Materials Research*, vol. 239-242, pp. 2822-2826, 2011.

[113] J. Onoro and C. Ranninger, "Exfoliation Corrosion Behaviour of Welded High Strength Aluminum Alloys," *British Corrosion Journal*, vol. 28, pp. 137-141, 1993.

[114] ASTM International, ASTM E112-13 Standard Test Methods for Determining Average Grain Size, 2013, West Conshohocken, PA.

[115] ASTM International, ASTM G85-11 Standard Practice for Modified Salt Spray (Fog) Testing, 2011, West Conshohocken, PA.

[116] GM World Wide Engineering Standards, GMW-14872 Cyclic Corrosion Laboratory Test, 2006.

[117] J. Dabrowski and J.R. Kish, "Exfoliation Corrosion Resistance of Fillet Arc-Welded Cu-Lean AA7xxx Lap Joints," in *COM 2012*, Niagara Falls, Ontario, Canada, 2012, p. 13.

[118] J. Dabrowski, M. Bruhis, and J.R. Kish, "Effect of Corrosion on the Strength of Fillet Arc Welded Cu-Lean AA7xxx Joints," in *Supplemental Proceedings: Materials Properties, Characterization, and Modeling, Volume 2*, Orlando, Florida, USA, 2012.

[119] K. Dehghani, A. Nekahi, and M.A.M. Mirzaie, "Optimizing the Bake Hardening Behaviour of Al7075 Using Response Surface Methodology," *Materials and Design*, vol. 31, pp. 1768-1775, 2010.

[120] X.G. Zhang, "Galvanic Corrosion ," in *Uhlig's Corrosion Handbook*, Winston Revie, Ed. Hoboken, New Jersey, USA: John Wiley and Sons, 2011, ch. 10, p. 1288.

[121] R.H Jones, *Stress Corrosion Cracking*. Materials Park, Ohio, USA: ASM International , 1992.

[122] J.F. Rudy and J. Rupert, "Effects of Porosity on Mechanical Properties of Aluminum Welds," *Welding Journal* , vol. 49, pp. 322s-336s, 1970.

[123] T.M. Morton, "Defects in 2021 Aluminum Alloy Welds," *Welding Journal* , vol. 51, pp. 304s-312s, 1971.

[124] I.I. Markov, "Influence of Porosity on Strength of Welded Butt Joints," *Welding Production*, vol. 19, pp. 45-49, 1972.

[125] H.M. Hussain, P.K. Ghosh, P.C. Gupta, and N.B. Potluri, "Fracture Toughness of Pulse Current Multipass GMA Welds of AL-Zn-Mg," *International Journal for the Joining of Materials* , vol. 11, pp. 77-88, 1999.

[126] R.J. Shore and R.B. McCauley, "Effects of Porosity on High Strength Aluminum 7039," *Welding Journal* , vol. 49, pp. 311s-321s, 1970.

[127] R.C. Wilcox, The Effect of Weld Penetration on the Tensile Strength of Fillet Welded Joints, 1995, Masters Thesis (University of Massachusetts).

Appendix A – Welded AA7003 and AA7108 Microhardness Plots

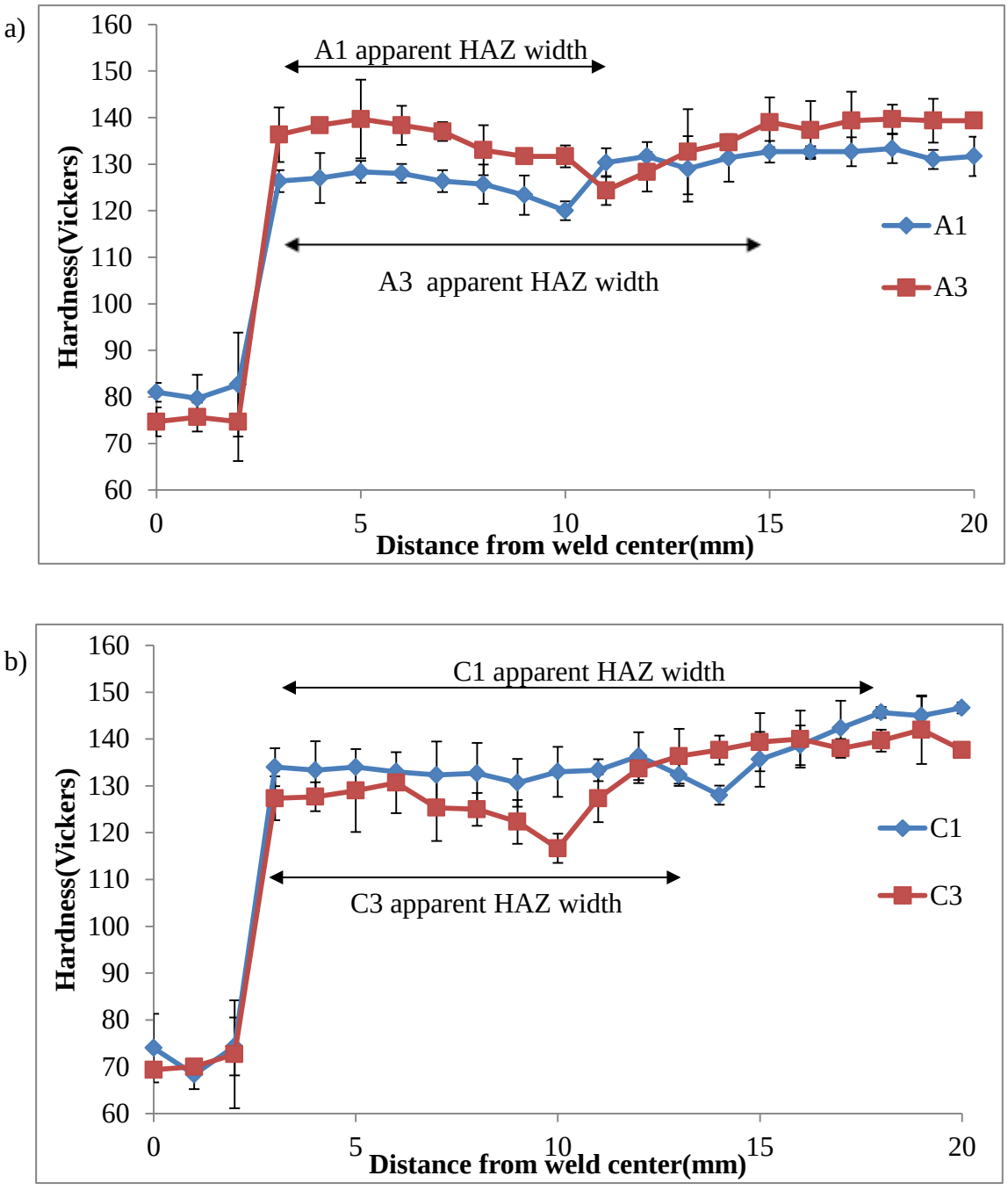

Figure A1 Microhardness plots of lap-joint welded (a) configuration A (ER5356/AA7003/⊥) and (b) configuration C (ER5356/AA7108/⊥).

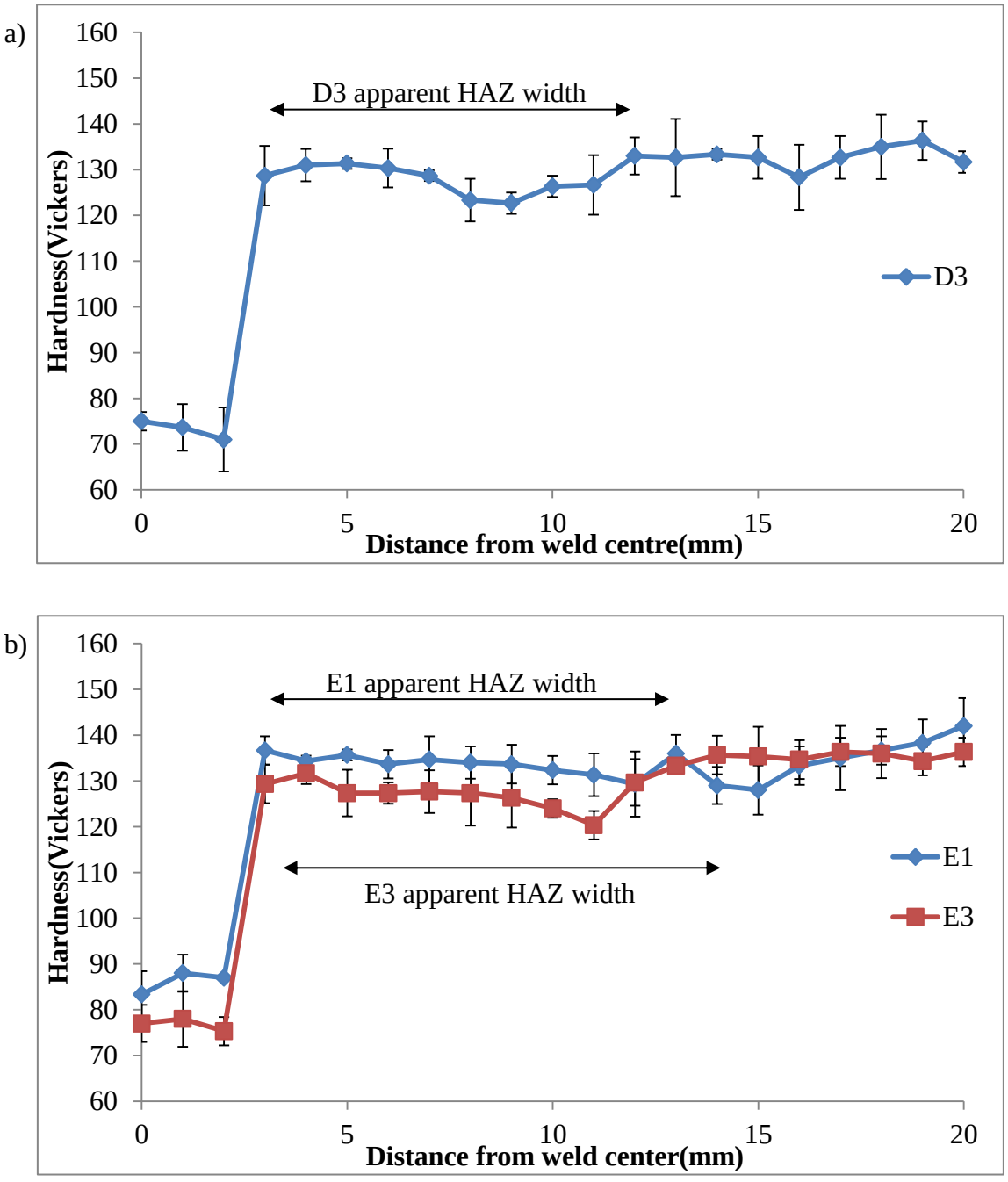

Figure A2 Microhardness plots of lap-joint welded (a) configuration D (ER4043/AA7003/⊥) and T-joint welded (b) configuration E (ER5356/AA7003/⊥).

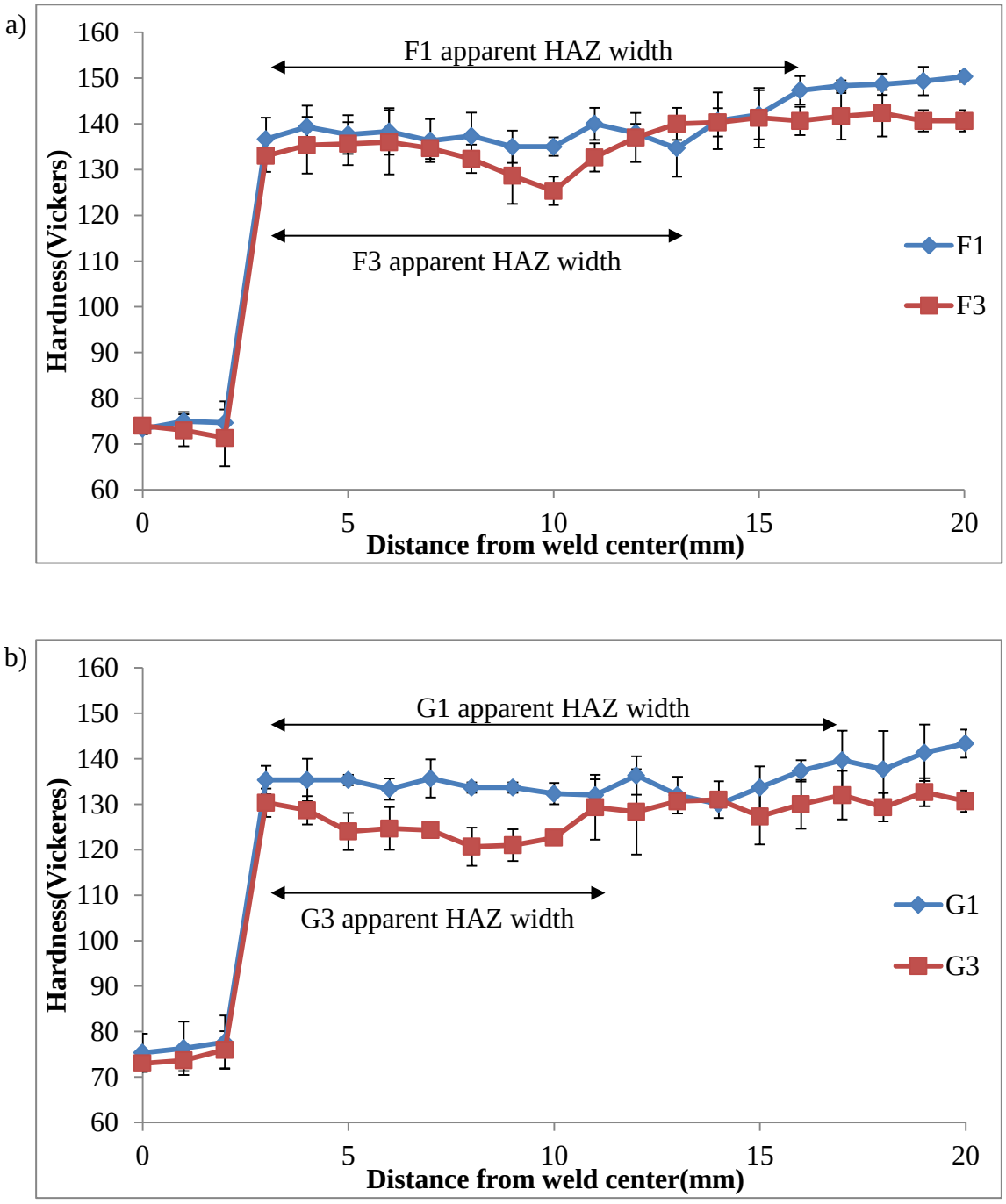

Figure A3 Microhardness plots of T-joint welded (a) configuration F (ER5356/AA7108/⊥) and lap-joint welded (b) configuration G (ER5356/AA7003/═).

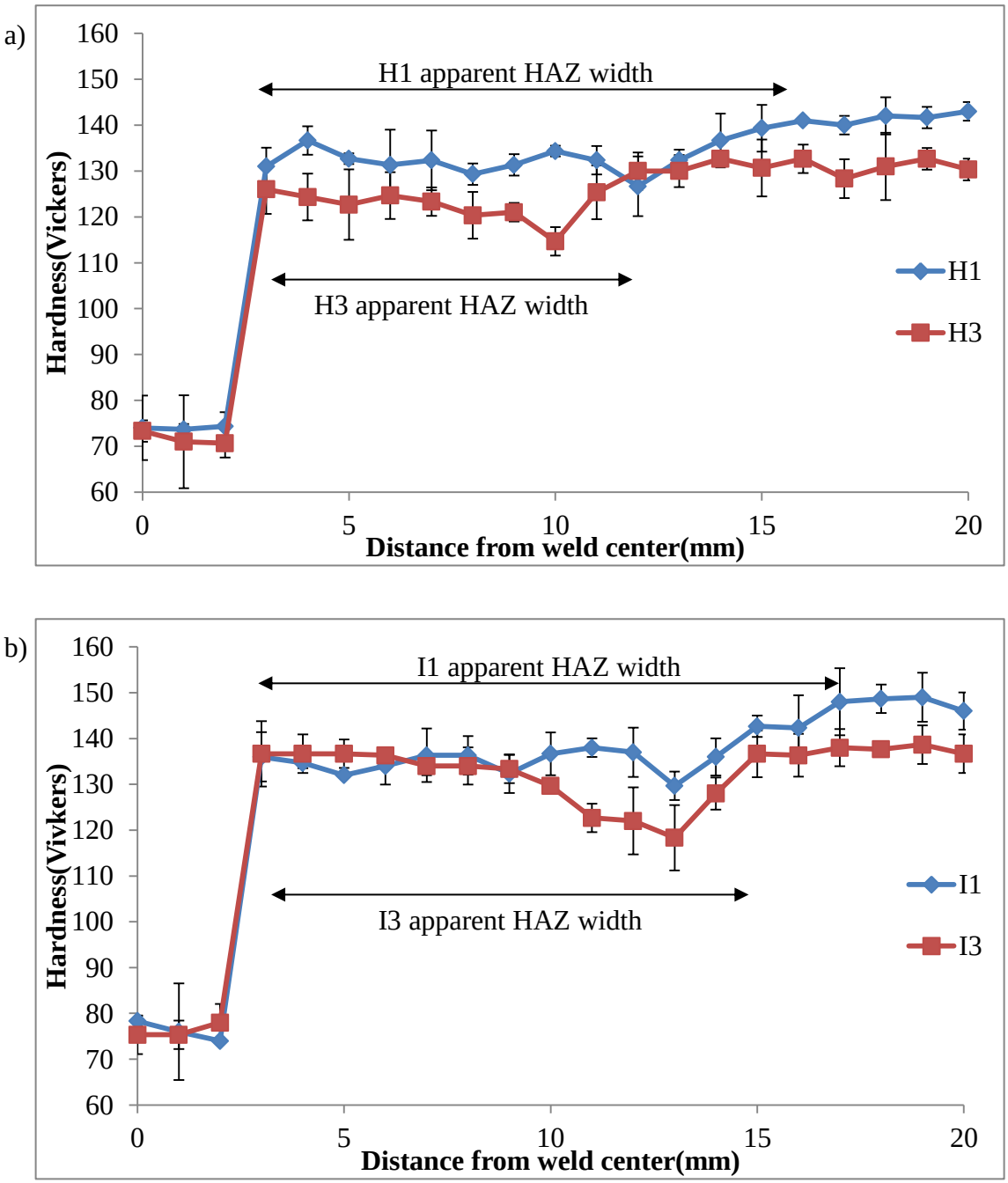

Figure A4 Microhardness plots of T-joint welded (a) configuration H (ER5356/AA7003/═) and lap-joint welded (b) configuration I (ER5356/AA7108/═).

Appendix B – Welded AA7003 and AA7108 Samples post Expousre to ASTM G85-A2

a) b)

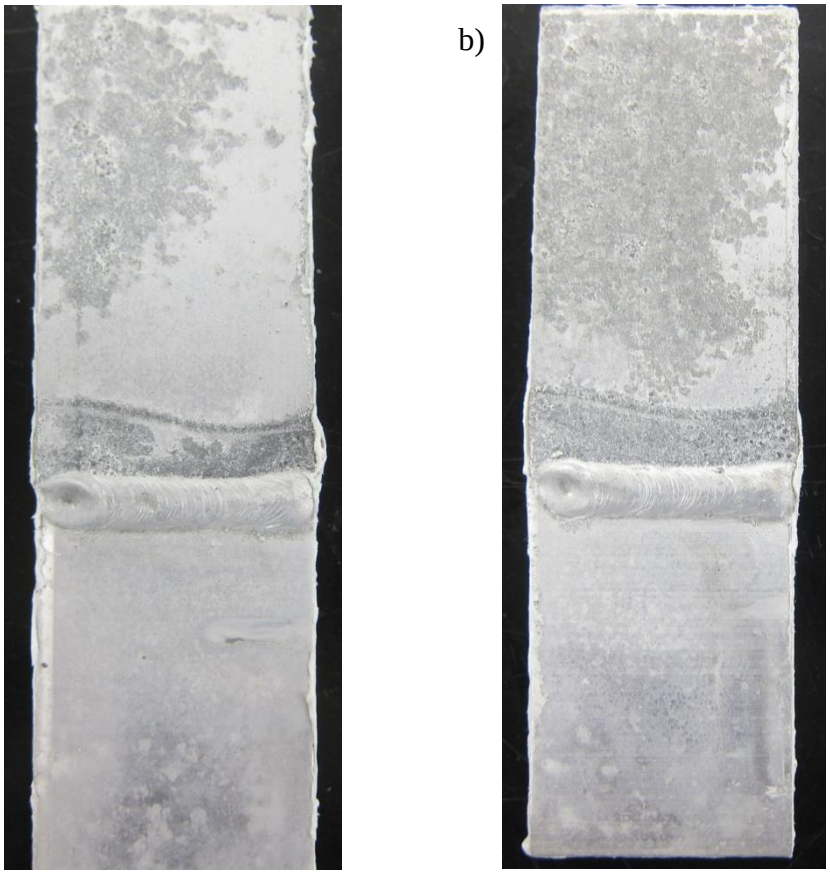

Figure B1 Duplicate samples of lap-joint welded configuration A1 (ER5356/AA7003/⊥) in the as-welded T6 condition.

a) b)

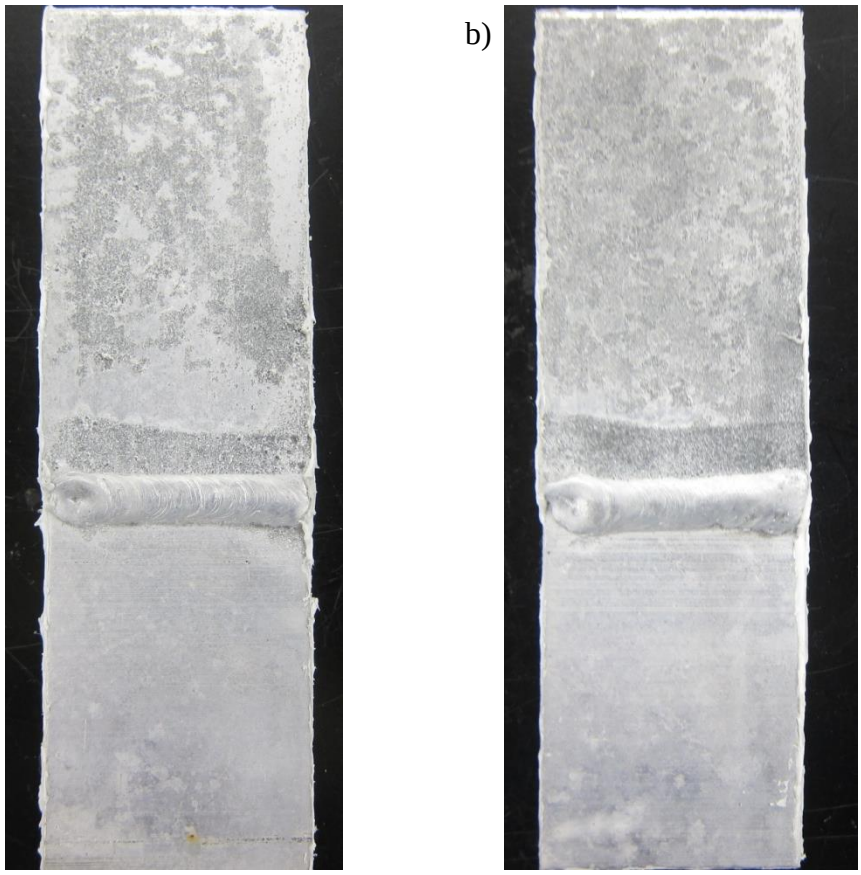

Figure B2 Duplicate samples of lap-joint welded configuration A3 (ER5356/AA7003/⊥) in the as-welded T6+PB condition.

a)  b) 

Figure B3 Duplicate samples of lap-joint welded configuration C1 (ER5356/AA7108/⊥) in the as-welded T6 condition.

a) b)

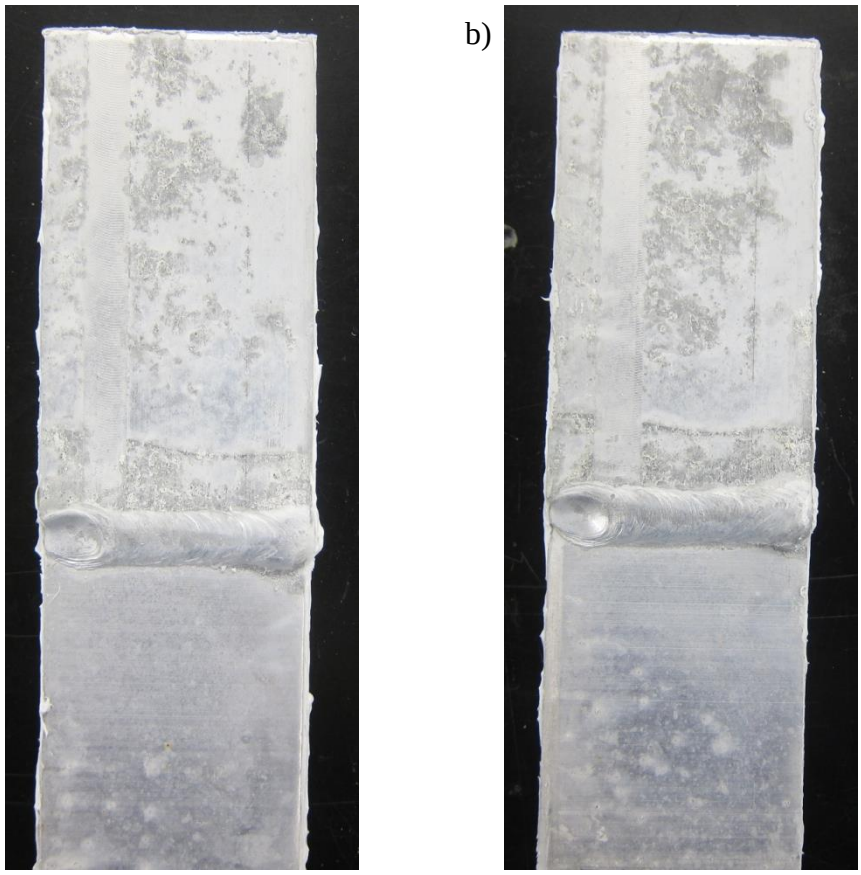

Figure B4 Duplicate samples of lap-joint welded configuration C3 (ER5356/AA7108/⊥) in the as-welded T6+PB condition.

a) b)

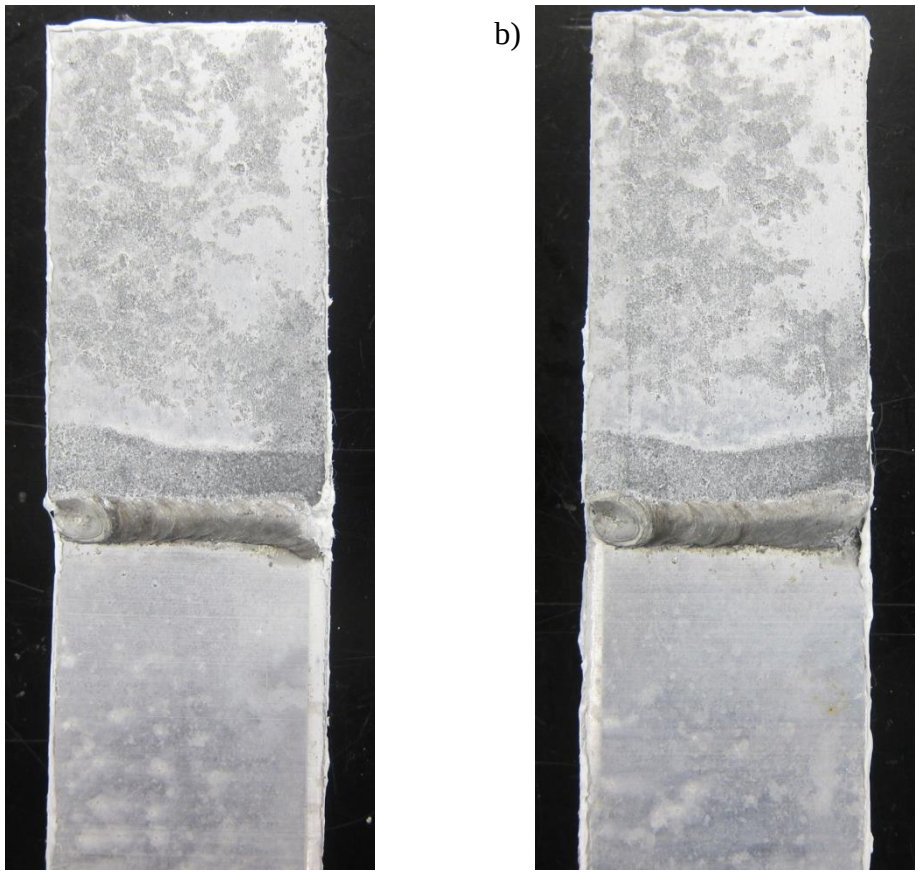

Figure B5 Duplicate samples of lap-joint welded configuration D3 (ER4043/AA7003/⊥) in the as-welded T6+PB condition.

a) b)

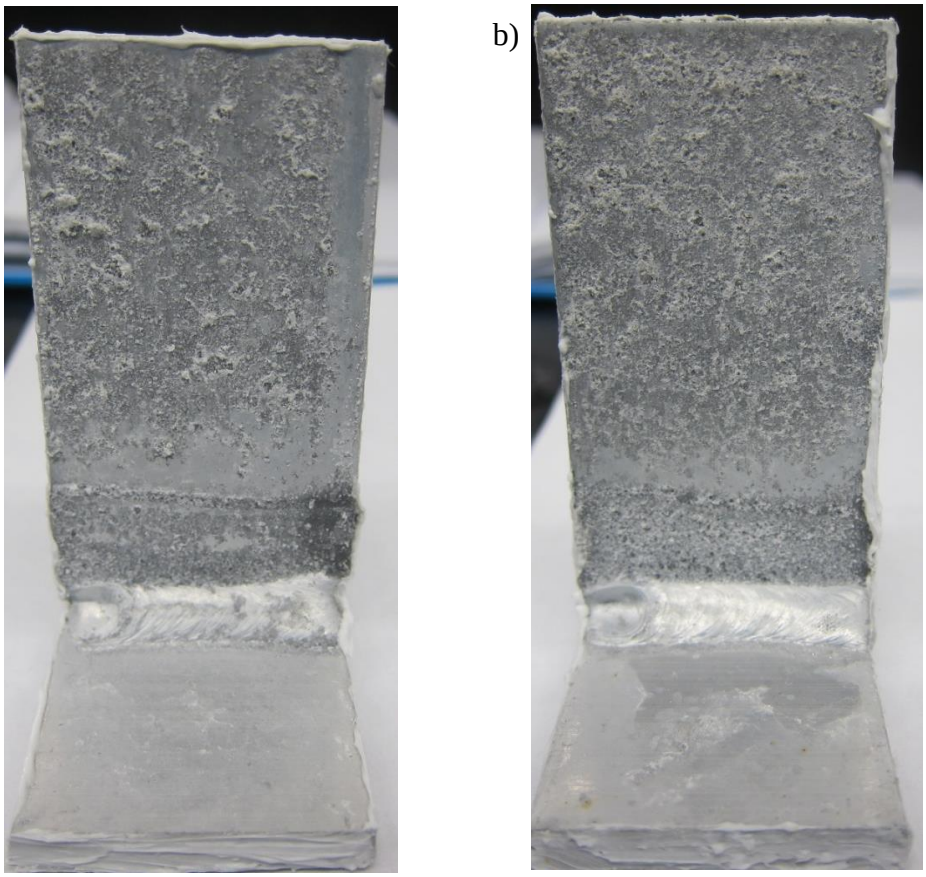

Figure B6 Duplicate samples of T-joint welded configuration E1 (ER5356/AA7003/⊥) in the as-welded T6 condition.

a) b)

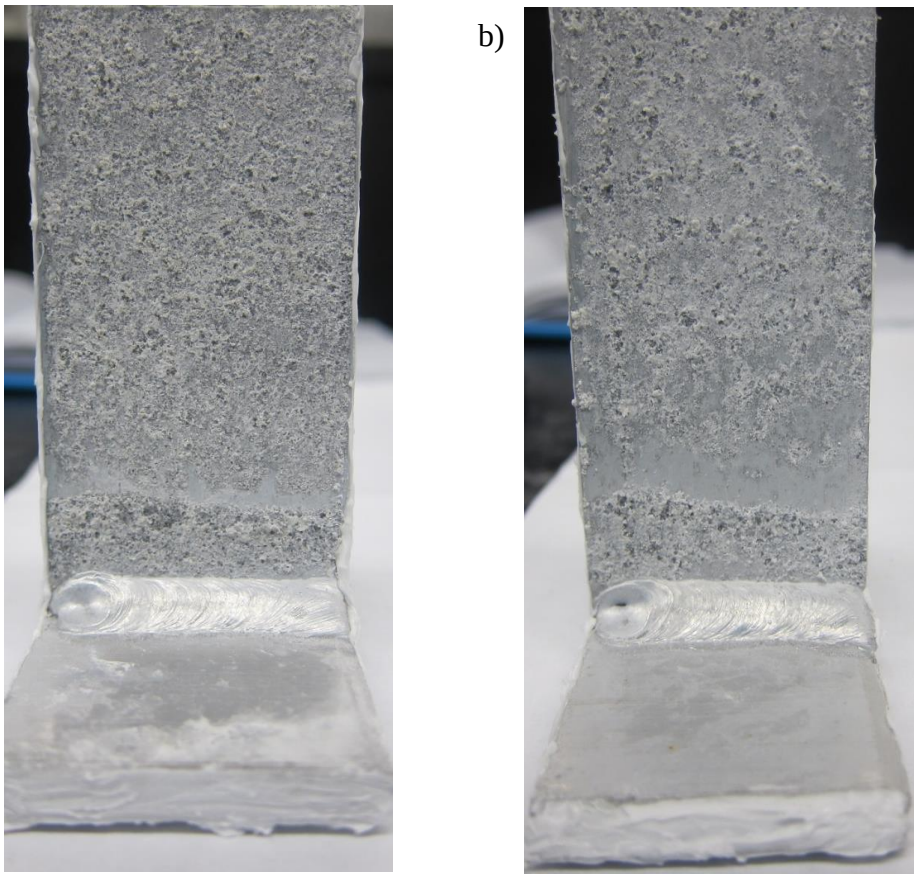

Figure B7 Duplicate samples of T-joint welded configuration E3 (ER5356/AA7003/⊥) in the as-welded T6+PB condition.

a) b)

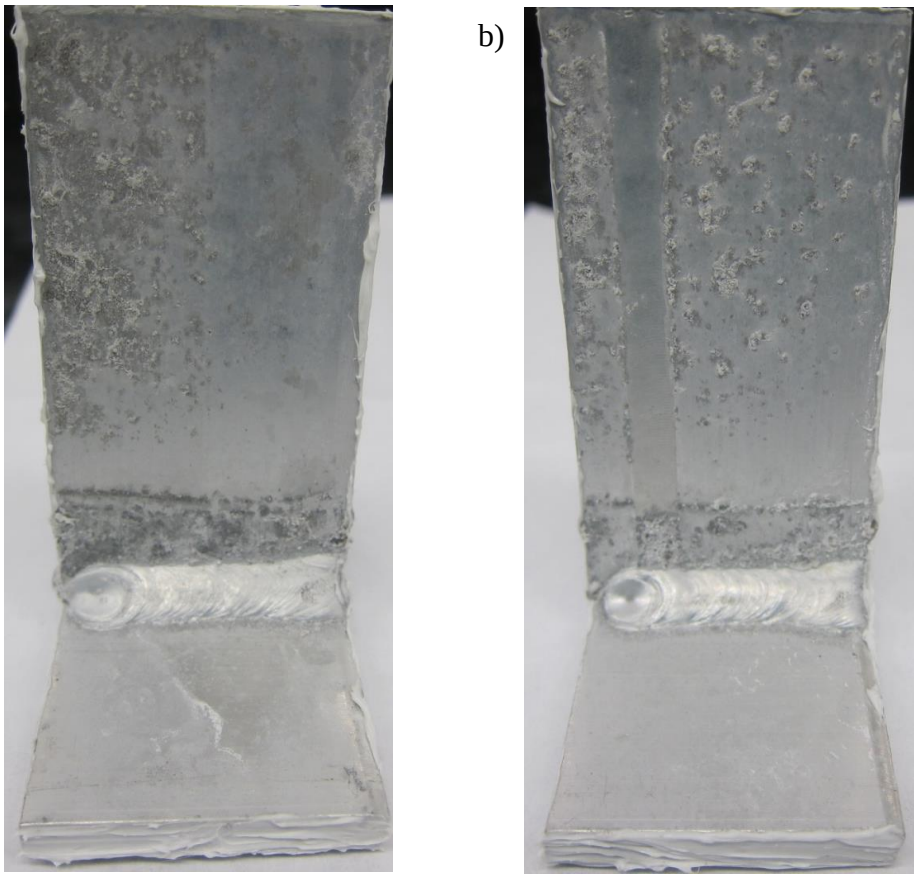

Figure B8 Duplicate samples of T-joint welded configuration F1 (ER5356/AA7108/⊥) in the as-welded T6 condition.

a) b)

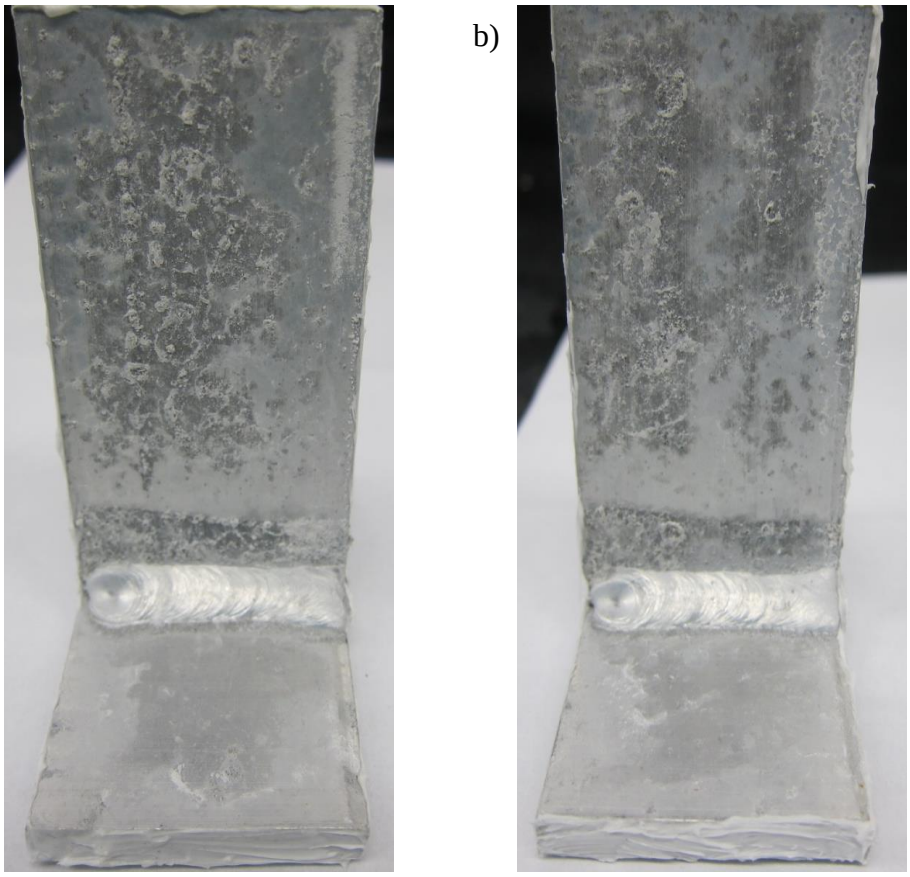

Figure B9 Duplicate samples of T-joint welded configuration F3 (ER5356/AA7108/⊥) in the as-welded T6+PB condition.

a) b)

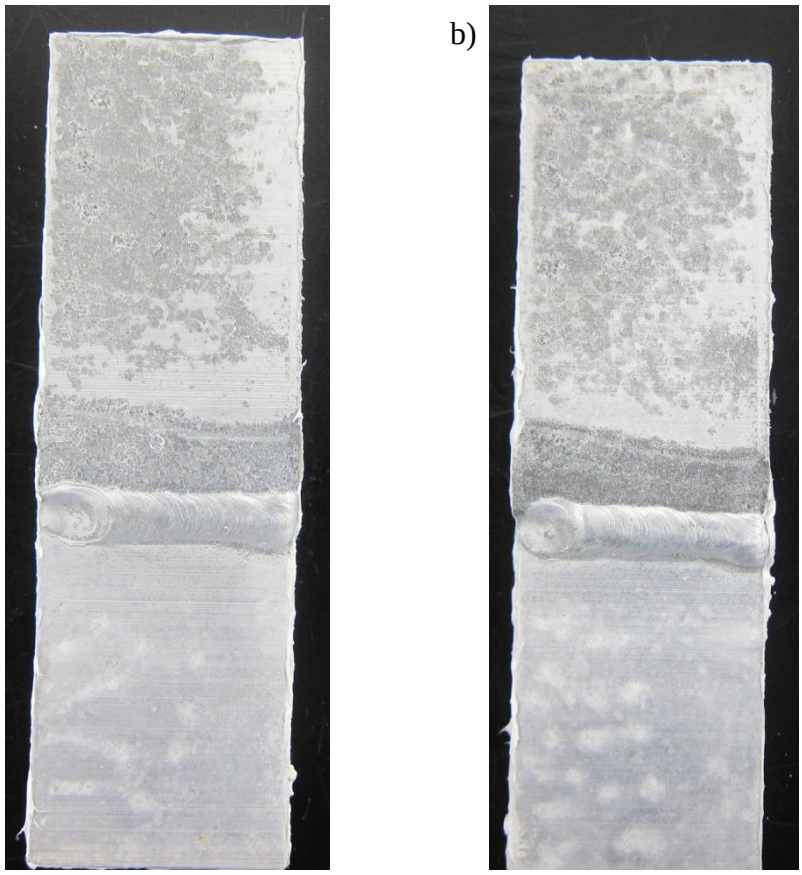

Figure B10 Duplicate samples of lap-joint welded configuration G1(ER5356/AA7003/═) in the as-welded T6 condition.

a) b)

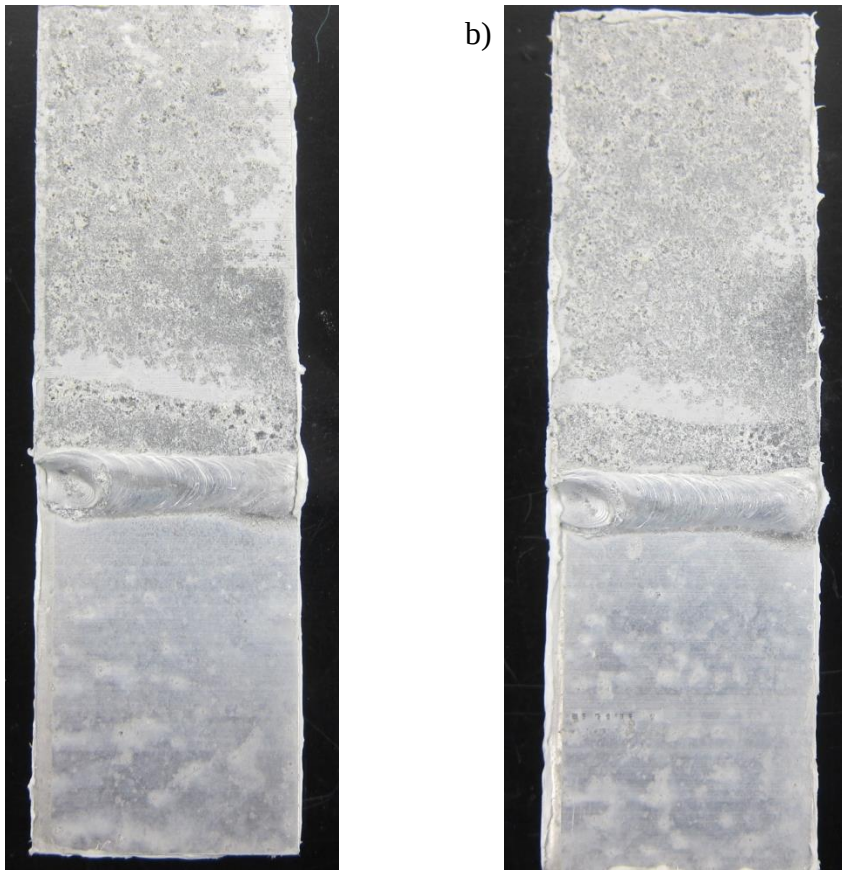

Figure B11 Duplicate samples of lap-joint welded configuration G3(ER5356/AA7003/═) in the as-welded T6+PB condition.

a) b)

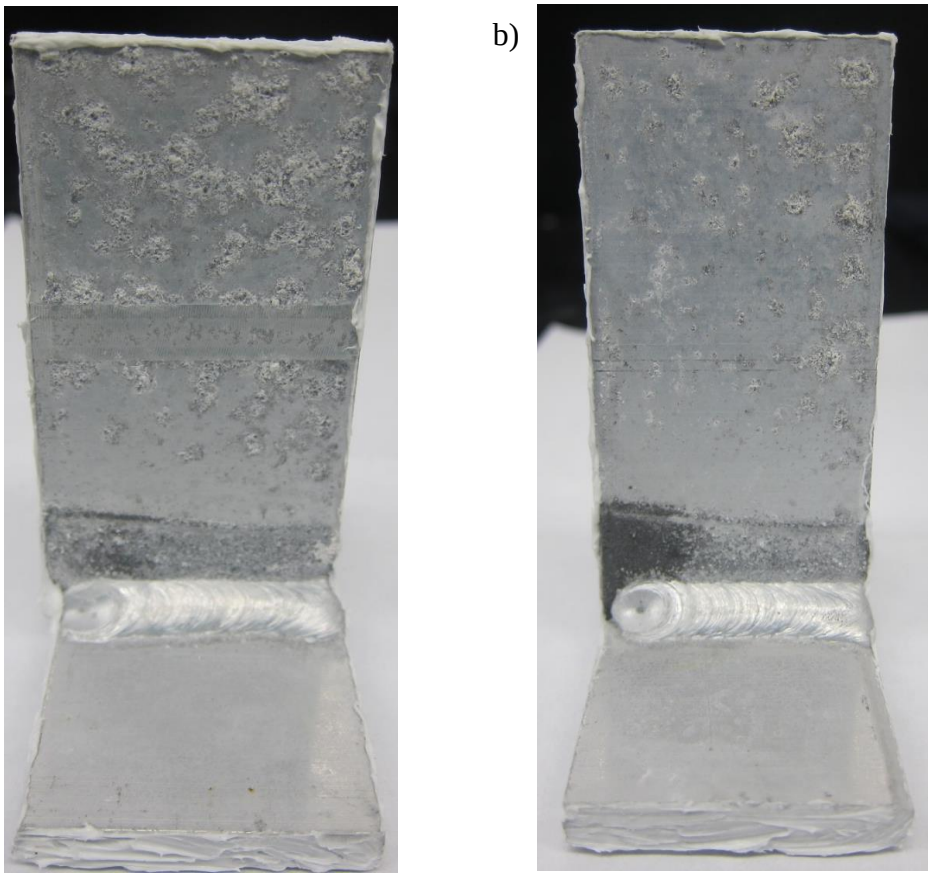

Figure B12 Duplicate samples of T-joint welded configuration H1(ER5356/AA7003/═) in the as-welded T6 condition.

a) b)

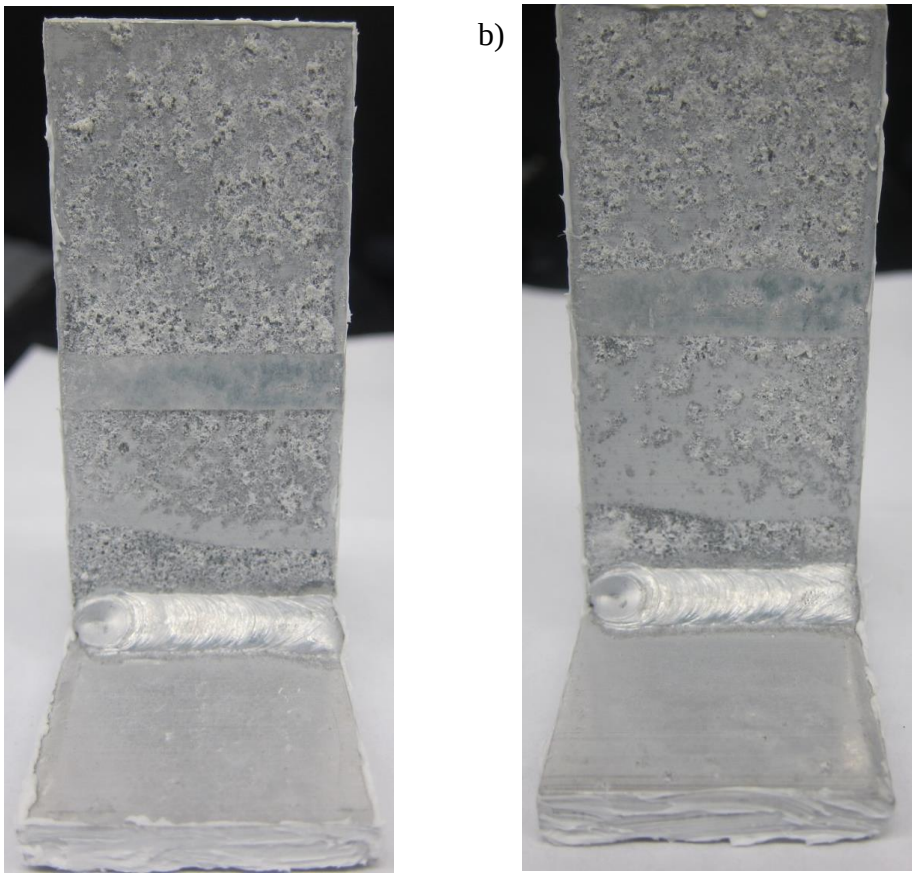

Figure B13 Duplicate samples of T-joint welded configuration H3 (ER5356/AA7003/═) in the as-welded T6+PB condition.

a) b)

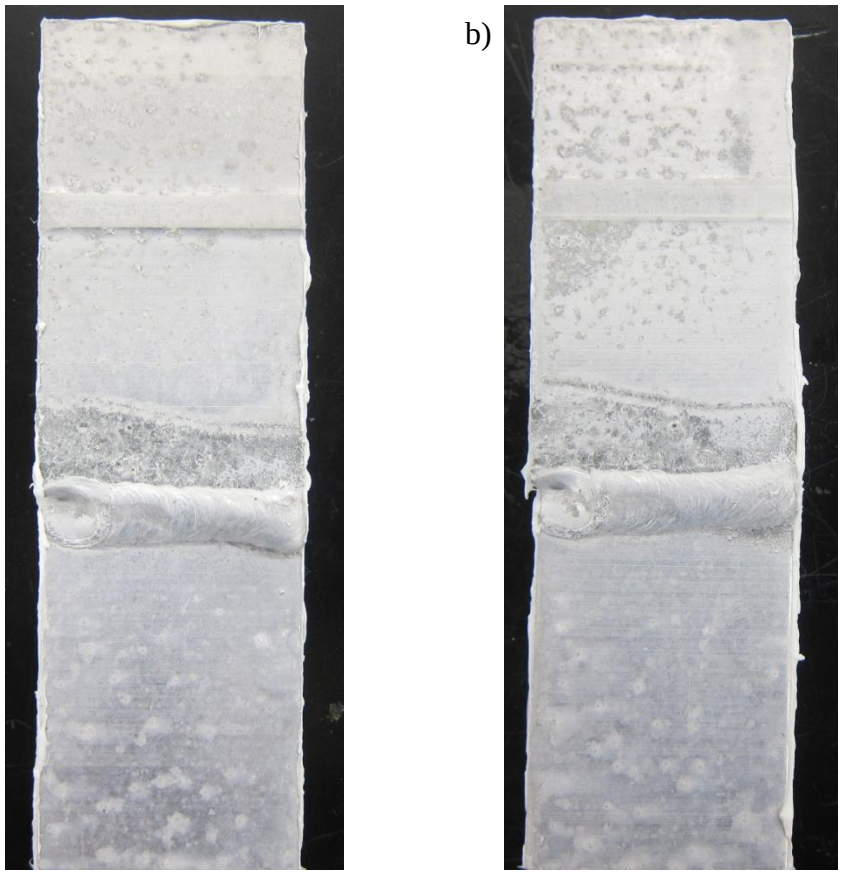

Figure B14 Duplicate samples of lap-joint welded configuration I1 (ER5356/AA7108/═) in the as-welded T6 condition.

a) b)

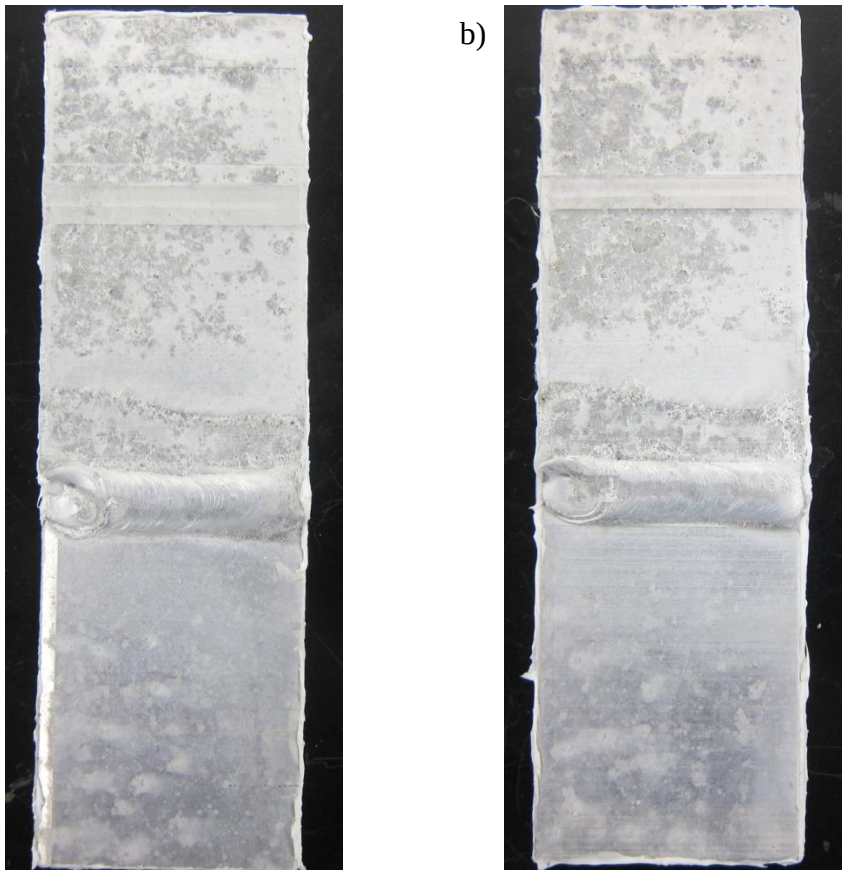

Figure B15 Duplicate samples of lap-joint welded configuration I3 (ER5356/AA7108/═) in the as-welded T6+PB condition.

Appendix C – Closes-up Images of the Weld Region of Welded AA7003 and AA7108 Samples Post Exposure to ASTM G85-A2

a)

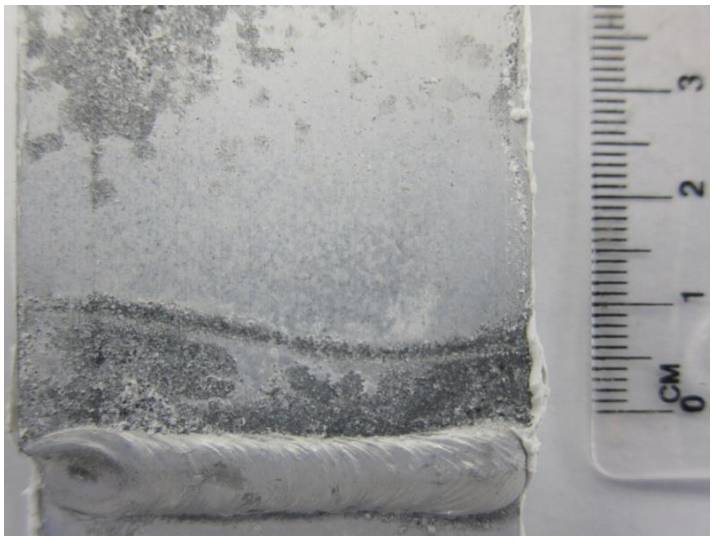

b)

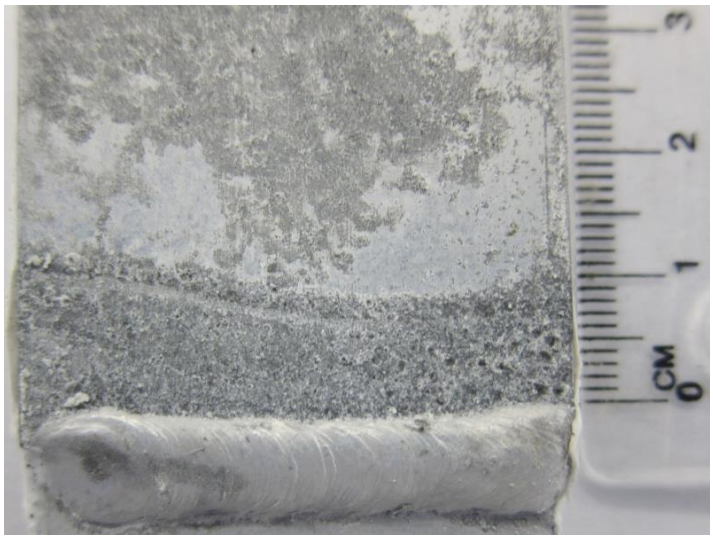

Figure C1 Close-up images of duplicate samples of lap-joint welded configuration A1 (ER5356/AA7003/⊥) in the as-welded T6 condition.

a)

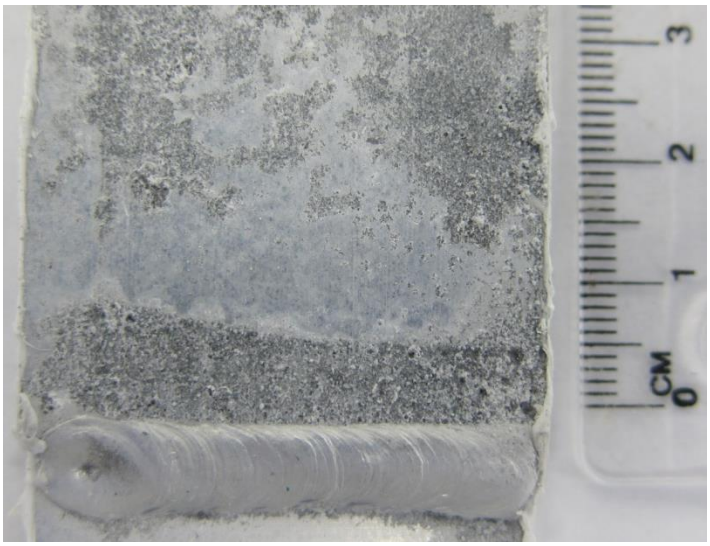

b)

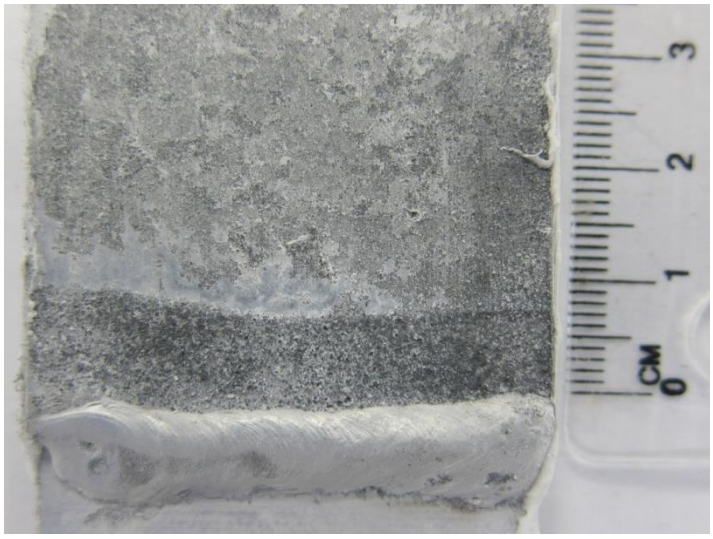

Figure C2 Close up images of duplicate samples of lap-joint welded configuration A3 (ER5356/AA7003/⊥) in the as-welded T6+PB condition.

a)

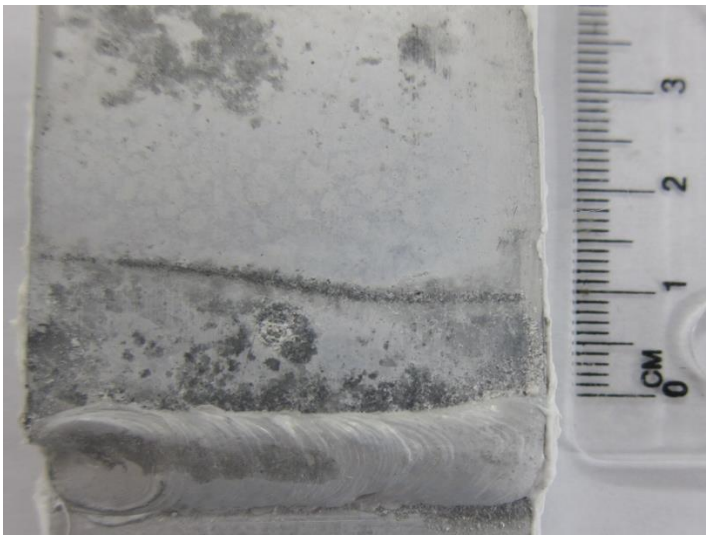

b)

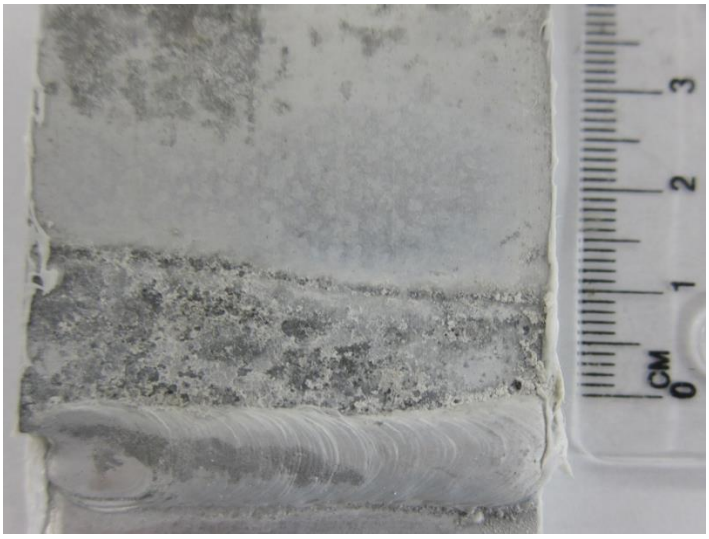

Figure C3 Close-up images of duplicate samples of lap-joint welded configuration C1 (ER5356/AA7108/⊥) in the as-welded T6 condition.

a)

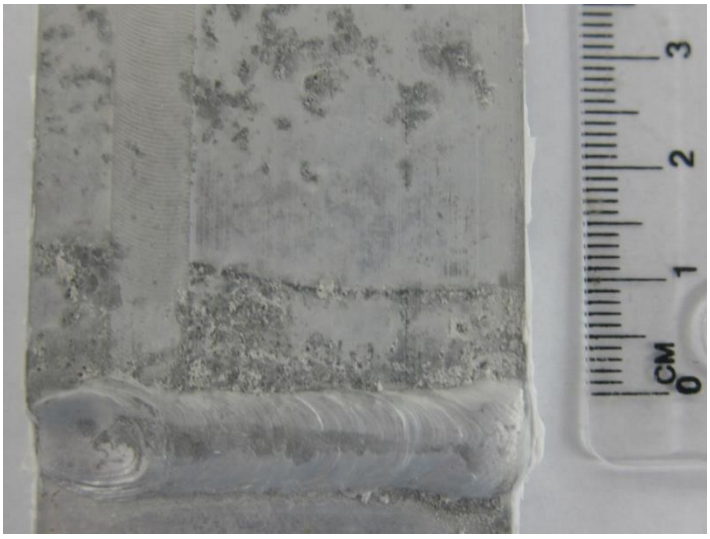

b)

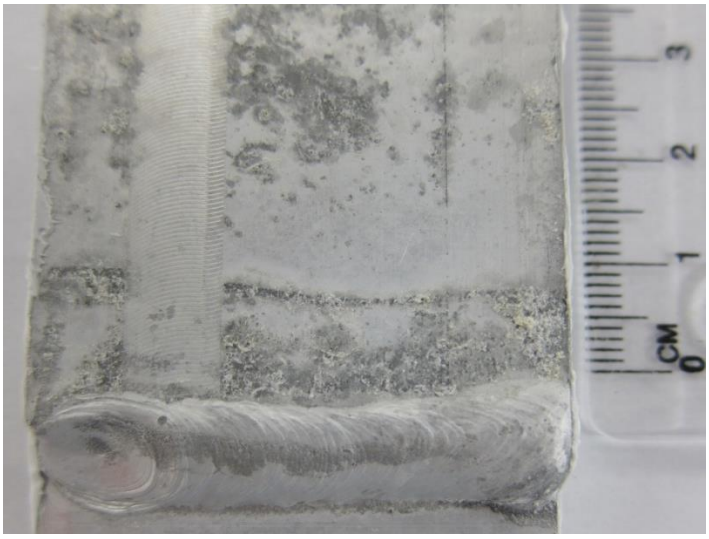

Figure C4 Close-up images of duplicate samples of lap-joint welded configuration C3 (ER5356/AA7108/⊥) in the as-welded T6+PB condition.

a)

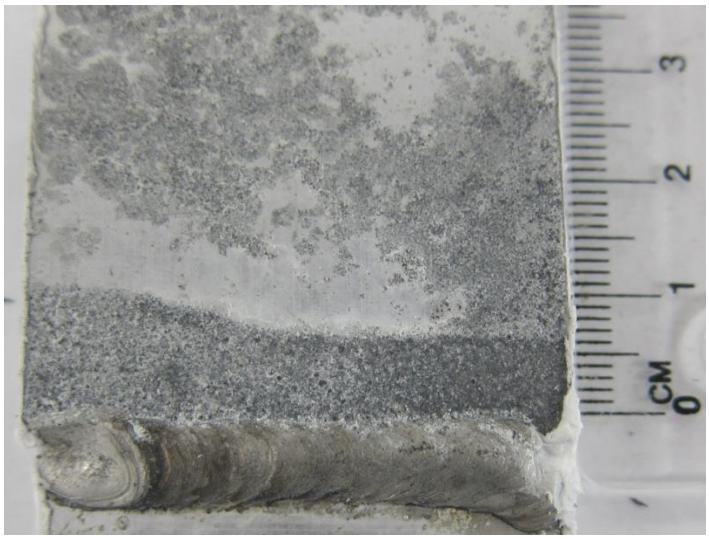

b)

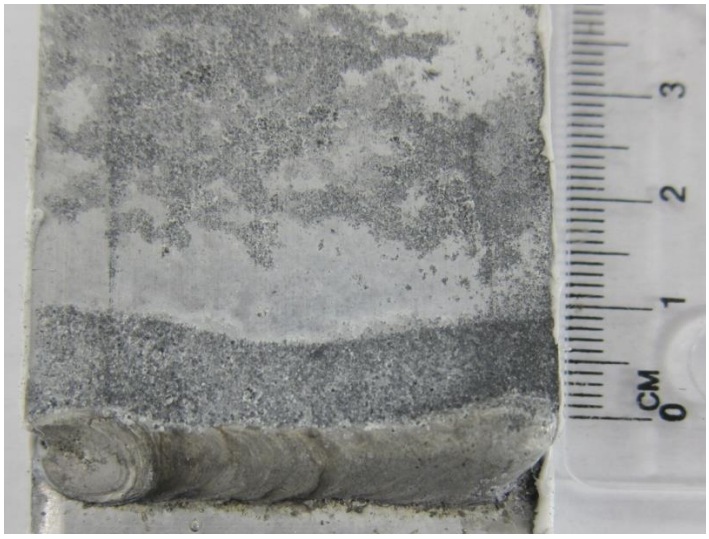

Figure C5 Close-up images of duplicate samples of lap-joint welded configuration D3 (ER4043/AA7003/⊥) in the as-welded T6+PB condition.

a)

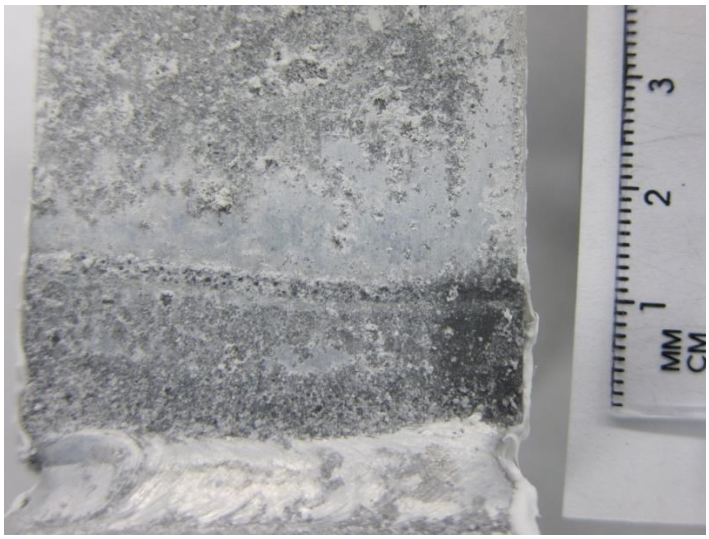

b)

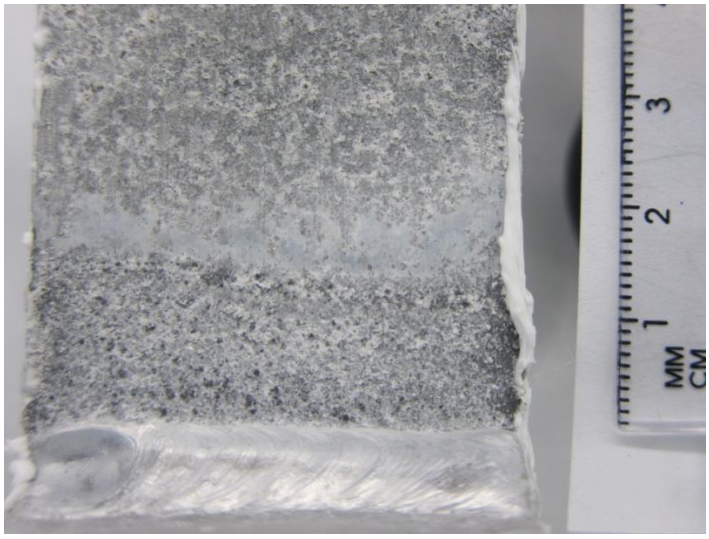

Figure C6 Close-up images of duplicate samples of T-joint welded configuration E1 (ER5356/AA7003/⊥) in the as-welded T6 condition.

a)

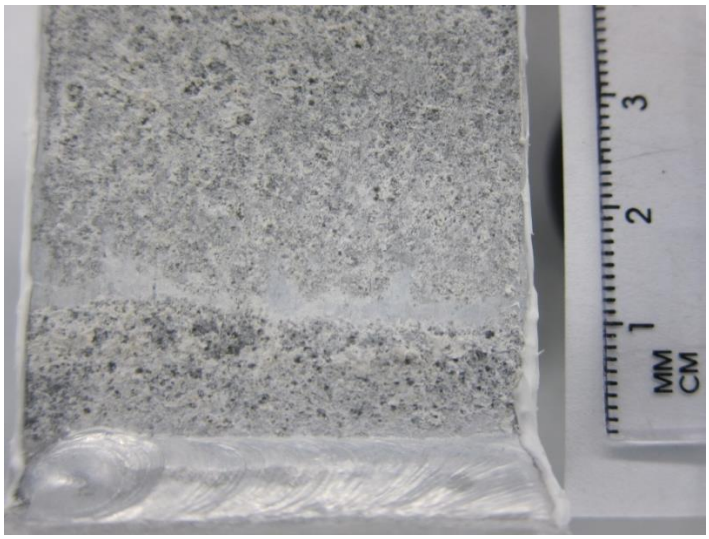

b)

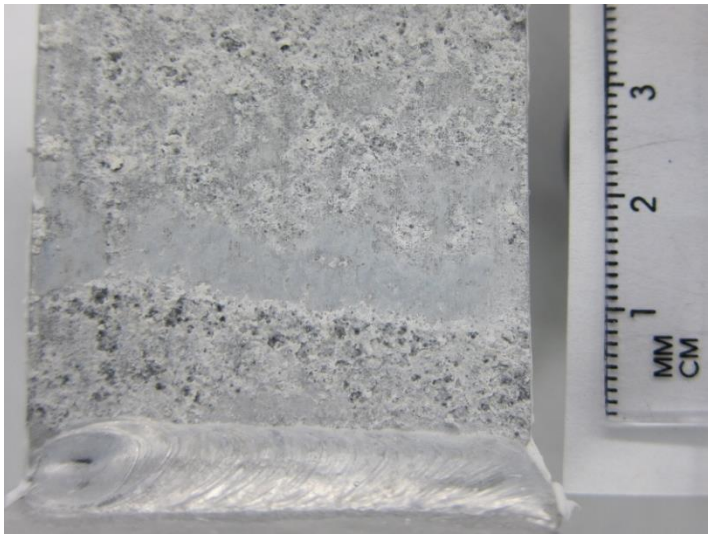

Figure C7 Close-up images of duplicate samples of T-joint welded configuration E3 (ER5356/AA7003/⊥) in the as-welded T6+PB condition.

a)

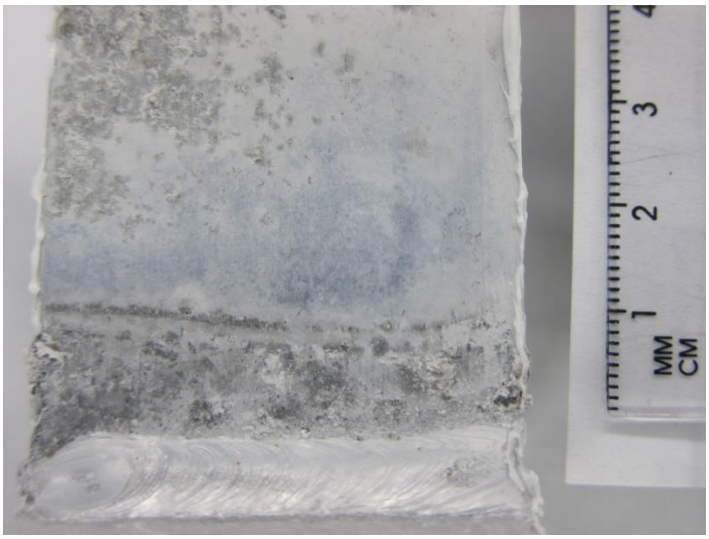

b)

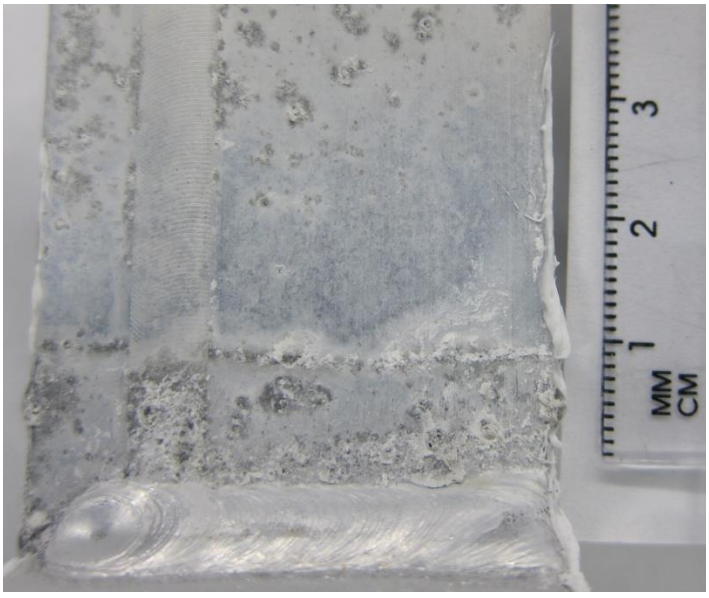

Figure C8 Close-up images of duplicate samples of T-joint welded configuration F1 (ER5356/AA7108/⊥) in the as-welded T6 condition.

a)

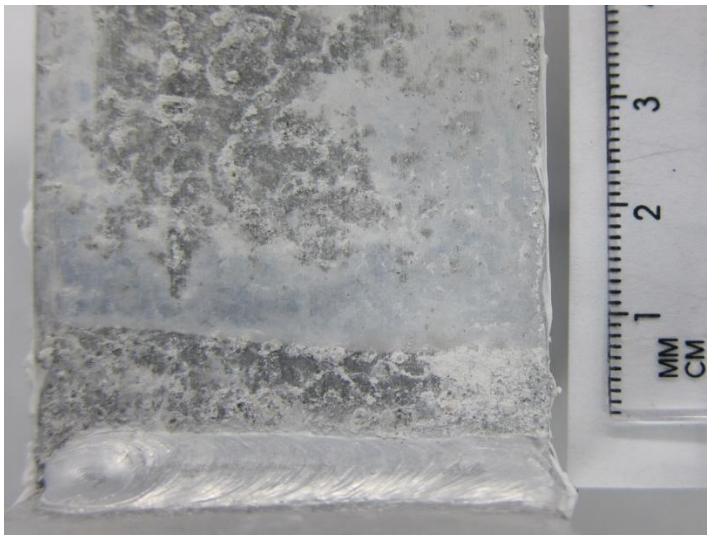

b)

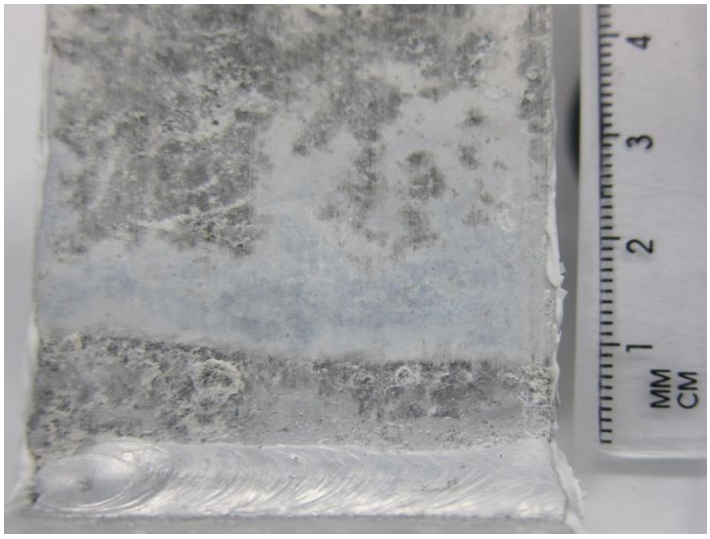

Figure C9 Close-up images of duplicate samples of T-joint welded configuration F3 (ER5356/AA7108/⊥) in the as-welded T6+PB condition.

a)

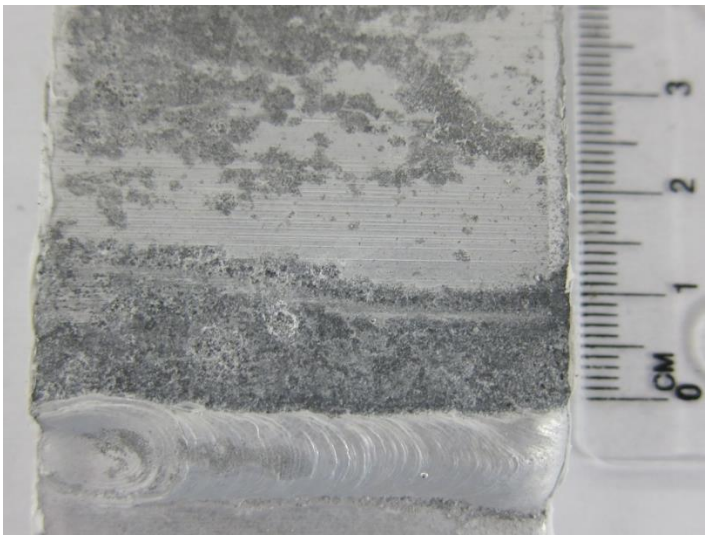

b)

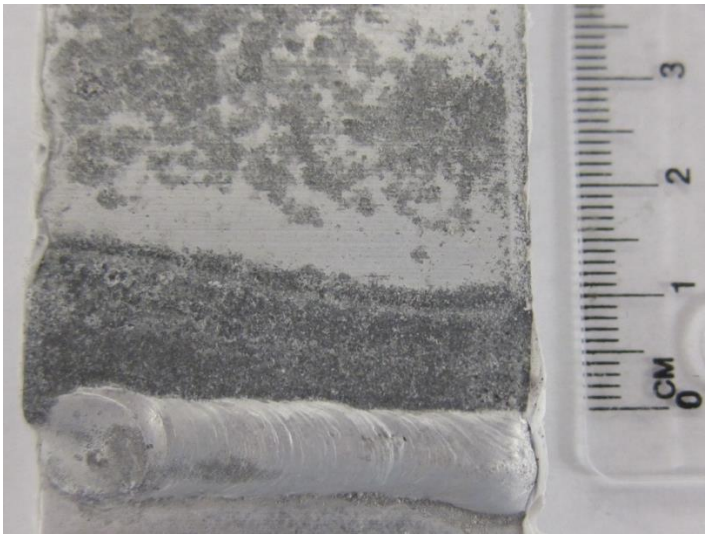

Figure C10 Close-up images of duplicate samples of lap-joint welded configuration G1 (ER5356/AA7003/═) in the as-welded T6 condition.

a)

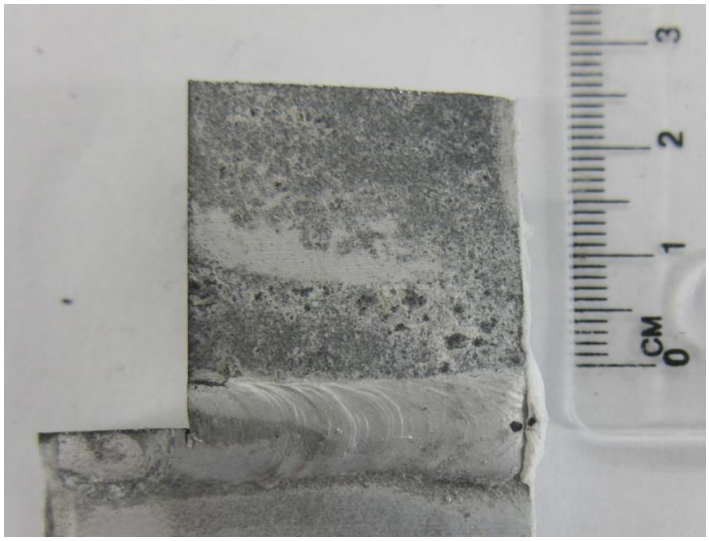

b)

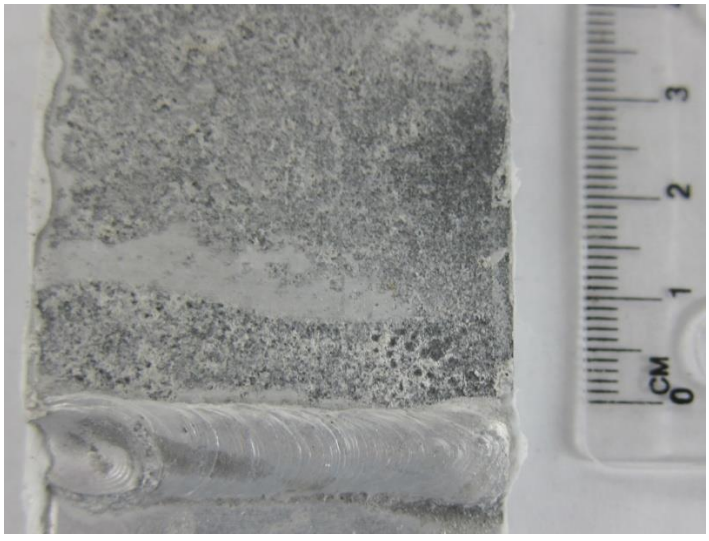

Figure C11 Close-up images of duplicate samples of lap-joint welded configuration G3 (ER5356/AA7003/═) in the as-welded T6+PB condition. Sample G3-2 was cross-sectioned prior to being photographed.

a)

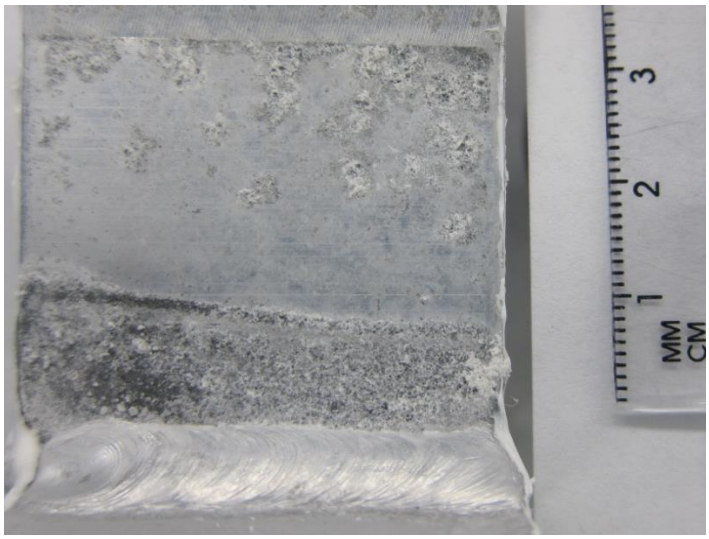

b)

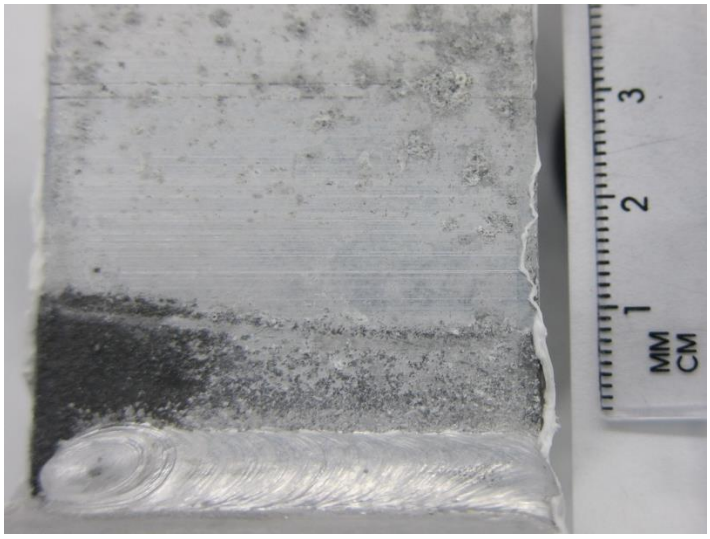

Figure C 12 Close-up images of duplicate samples of T-joint welded configuration H1 (ER5356/AA7003/═) in the as-welded T6 condition.

a)

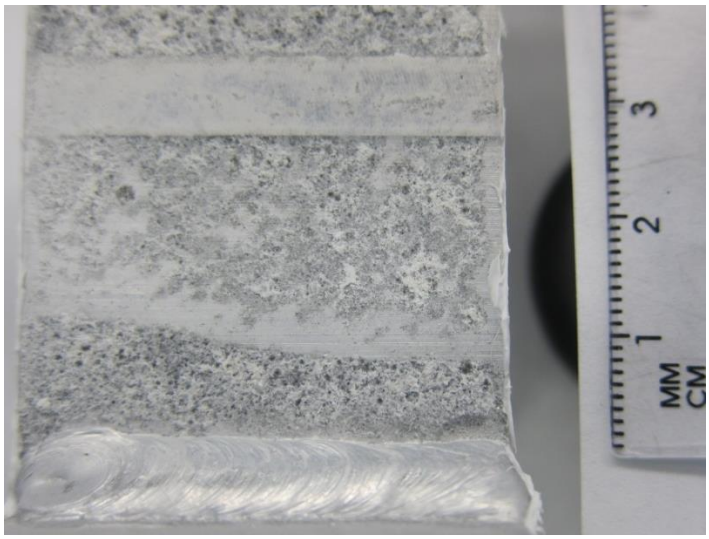

b)

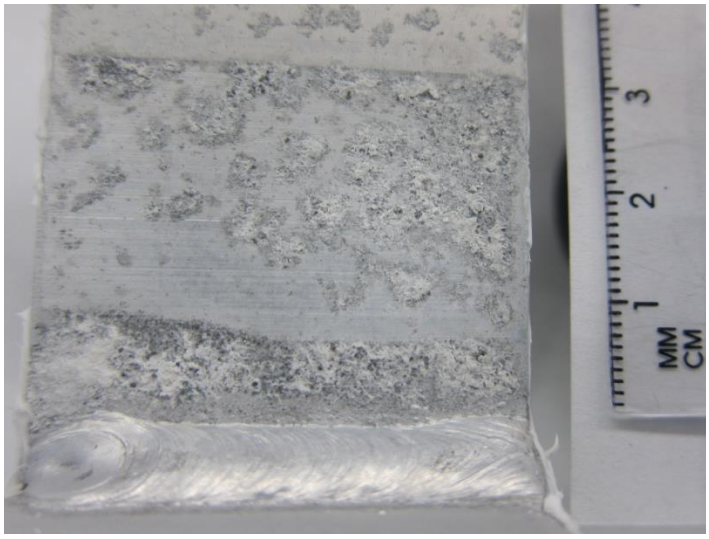

Figure C13 Close-up images of duplicate samples of T-joint welded configuration H3 (ER5356/AA7003/═) in the as-welded T6+PB condition.

a)

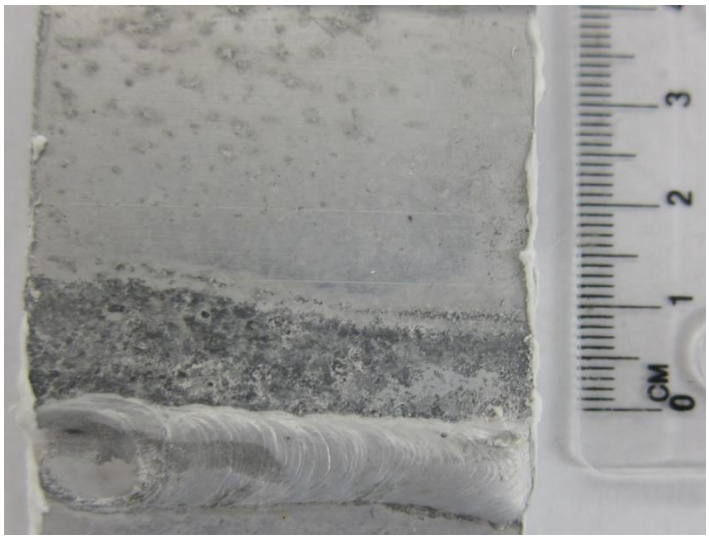

b)

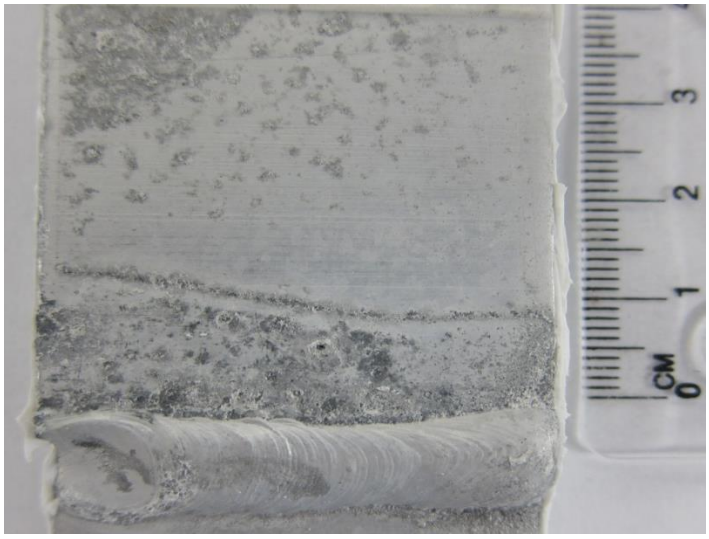

Figure C14 Close-up images of duplicate samples of lap-joint welded configuration I1 (ER5356/AA7108/═) in the as-welded T6 condition.

a)

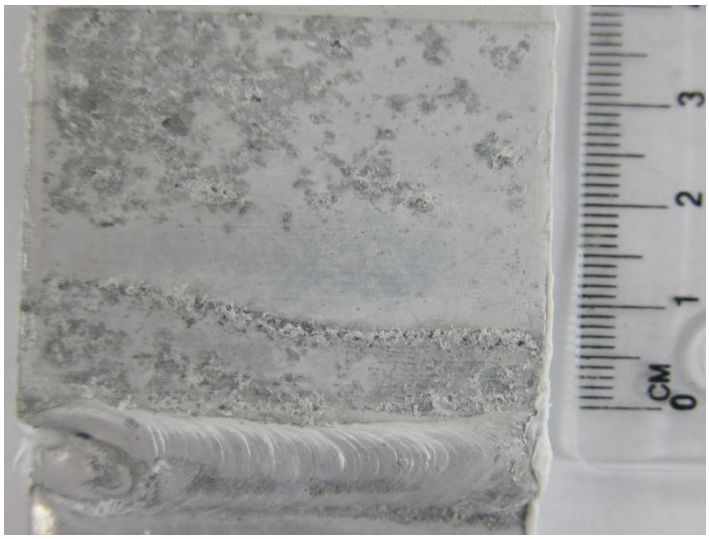

b)

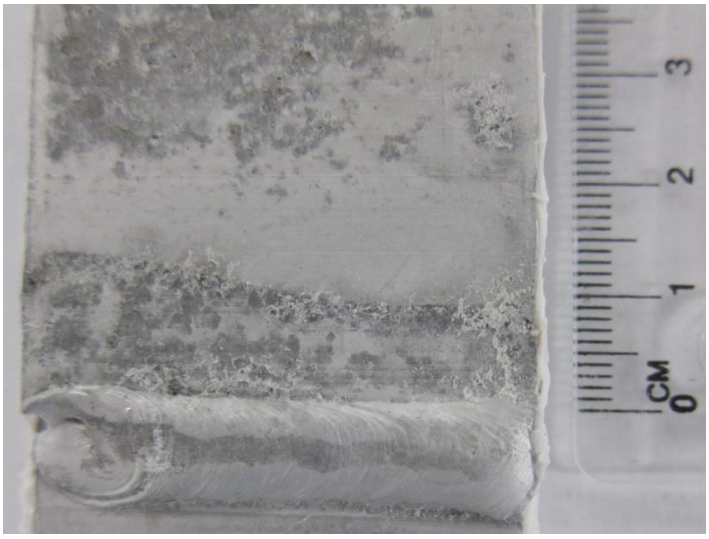

Figure C15 Close-up images of duplicate samples of lap-joint welded configuration I3 (ER5356/AA7108/═) in the as-welded T6+PB condition.

Appendix D – Large Area Cross-Sectional Scans of Welded AAA7003 and AA7108 Post ASTM G85-A2

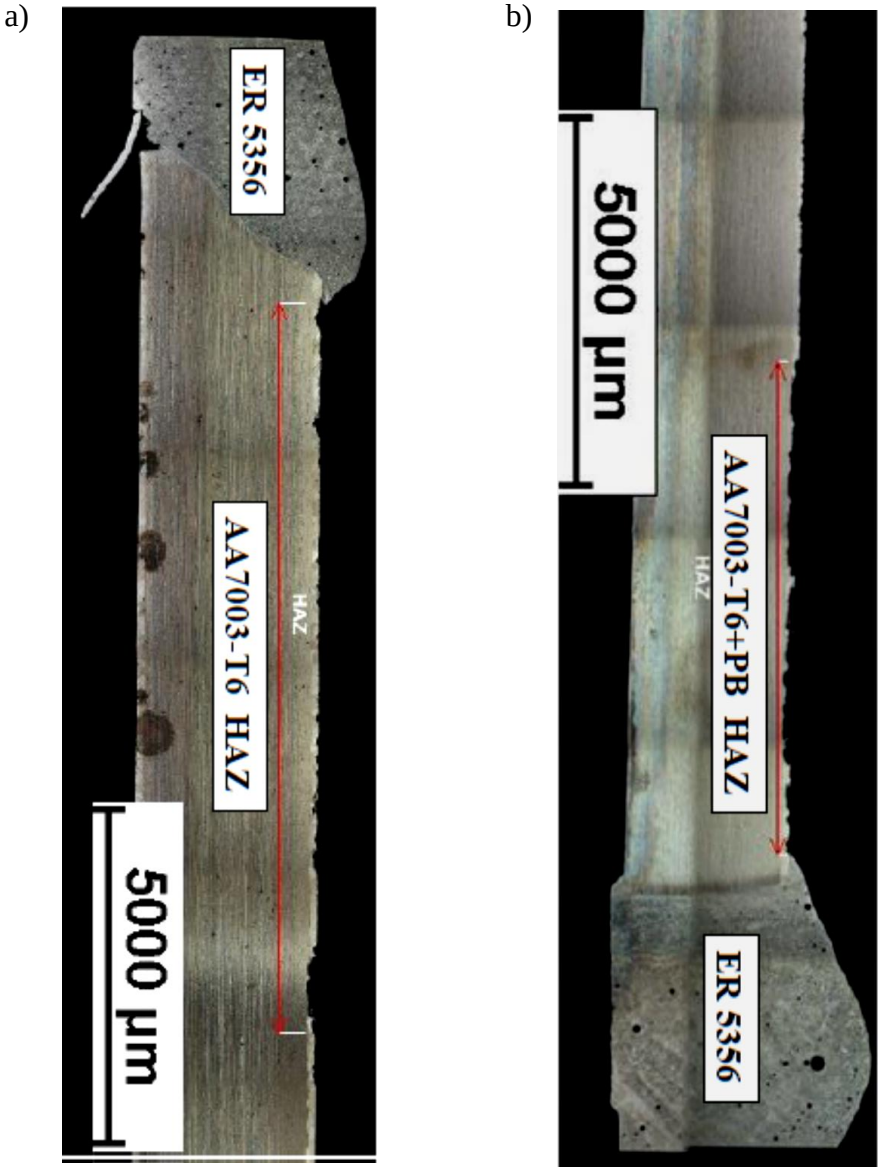

Figure D1 Large area scans of lap-joint welded configuration A (ER5356/AA7003/⊥) in the (a) as-welded T6 condition and (b) as-welded T6+PB condition post exposure to ASTM G85-A2.

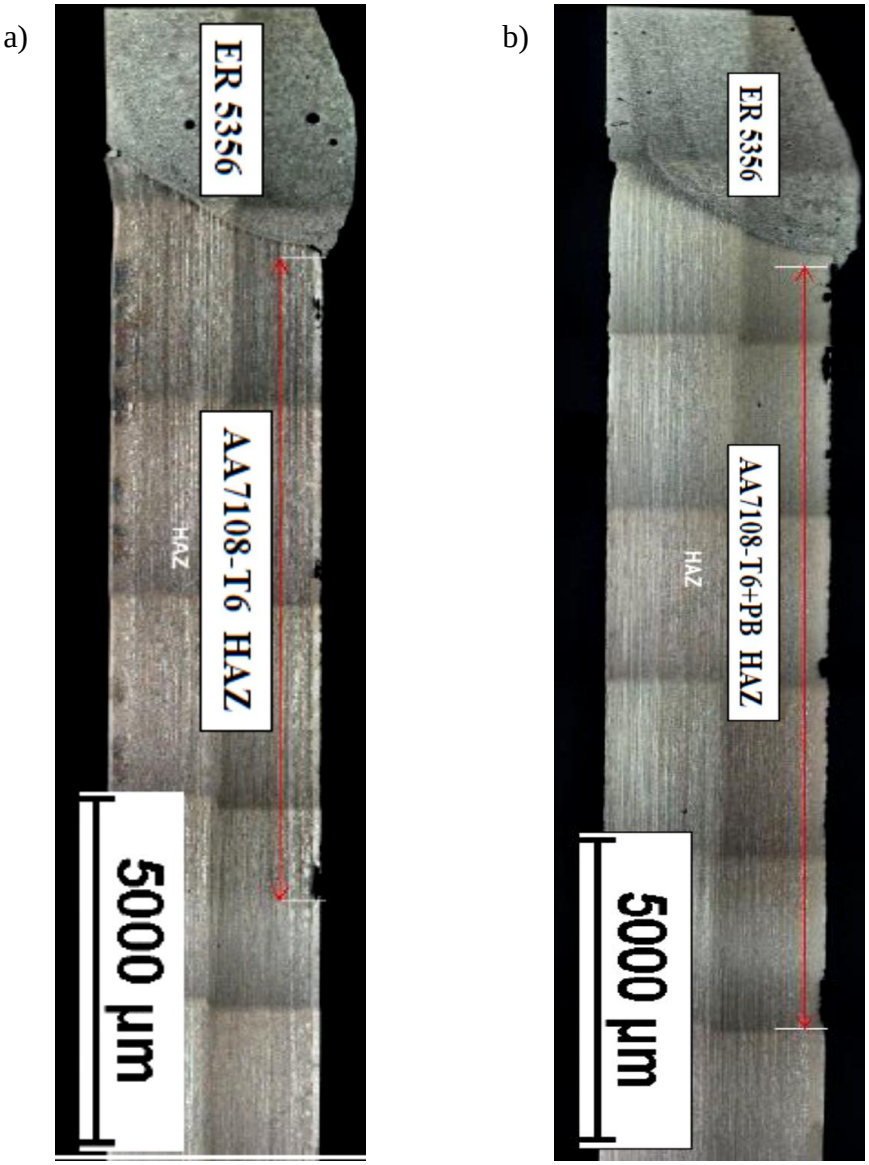

Figure D2 Large area scans of lap-joint welded configuration C (ER5356/AA7108/⊥) in the (a) as-welded T6 condition and (b) as-welded T6+PB condition post exposure to ASTM G85-A2.

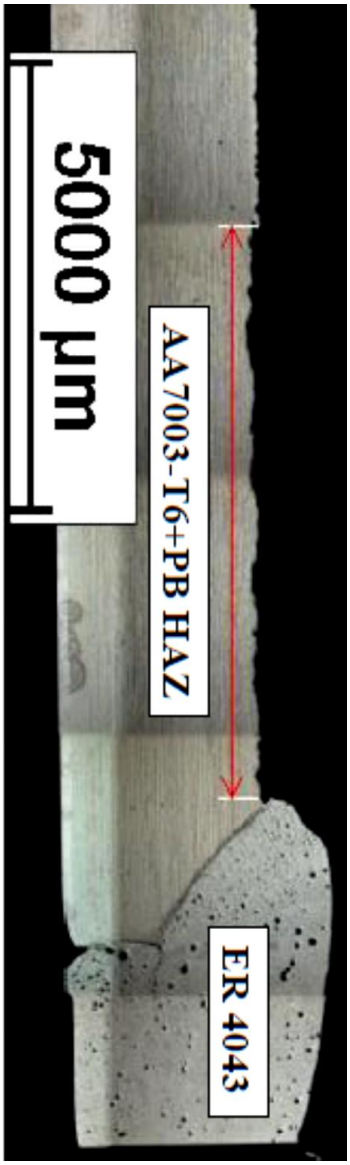

Figure D3 Large area scans of lap-joint welded configuration D (ER4043/AA7003/⊥) in as-welded T6+PB condition post exposure to ASTM G85-A2.

a)

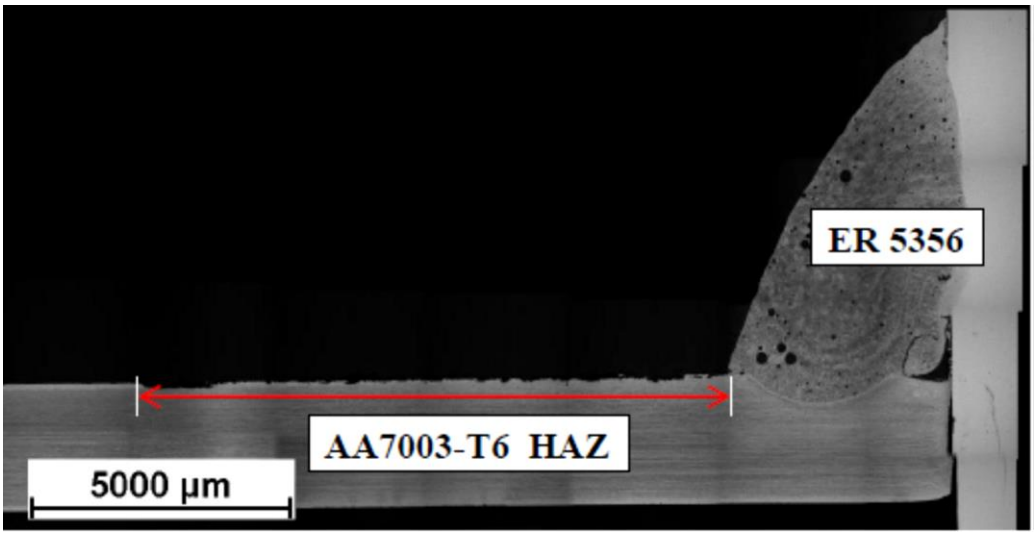

b)

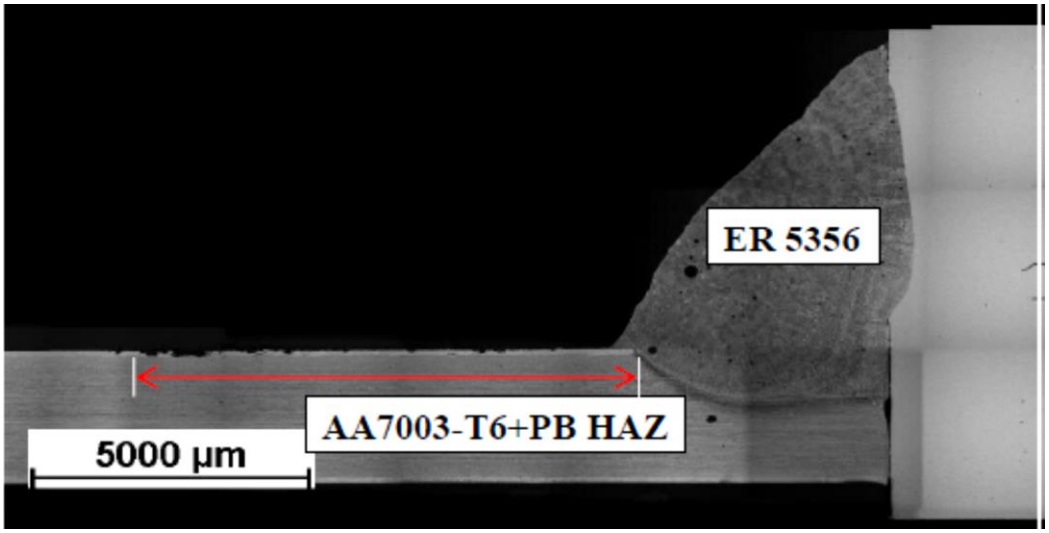

Figure D4 Large area scans of T-joint welded configuration E (ER5356/AA7003/⊥) in the (a) as-welded T6 condition and the (b) as-welded T6+PB condition post exposure to ASTM G85-A2.

a)

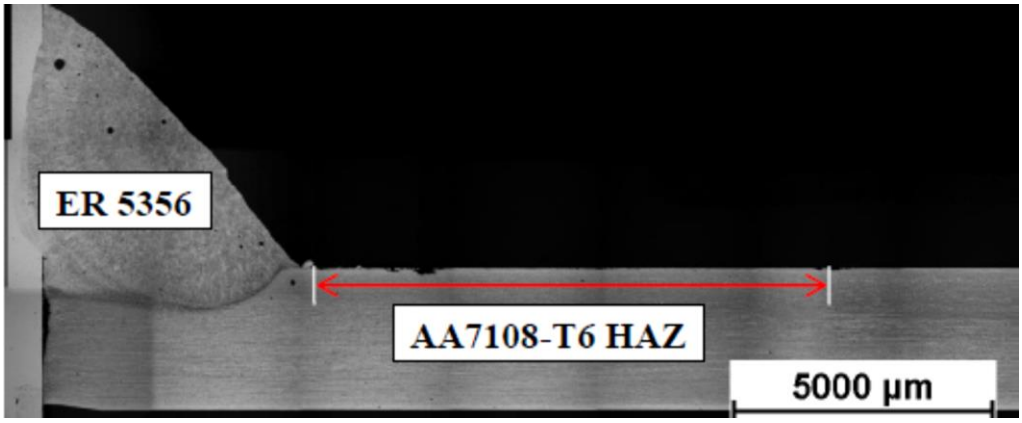

b)

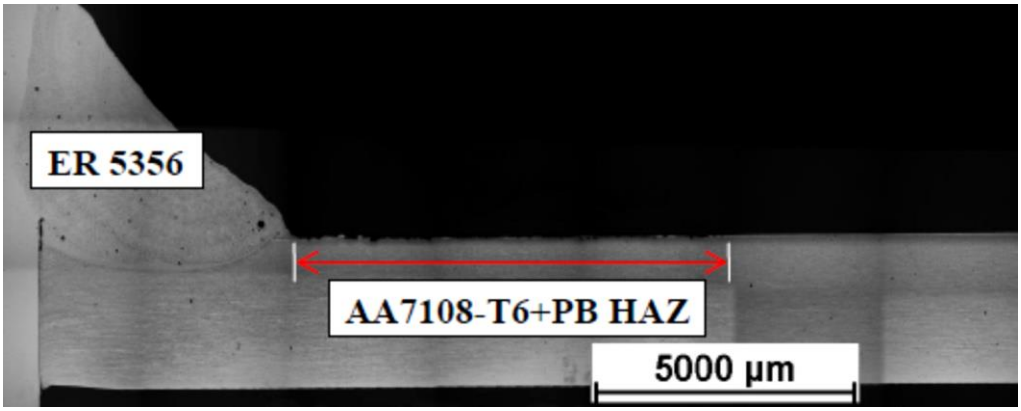

Figure D5 Large area scans of T-joint welded configuration F (ER5356/AA7108/⊥) in the (a) as-welded T6 condition and the (b) as-welded T6+PB condition post exposure to ASTM G85-A2.

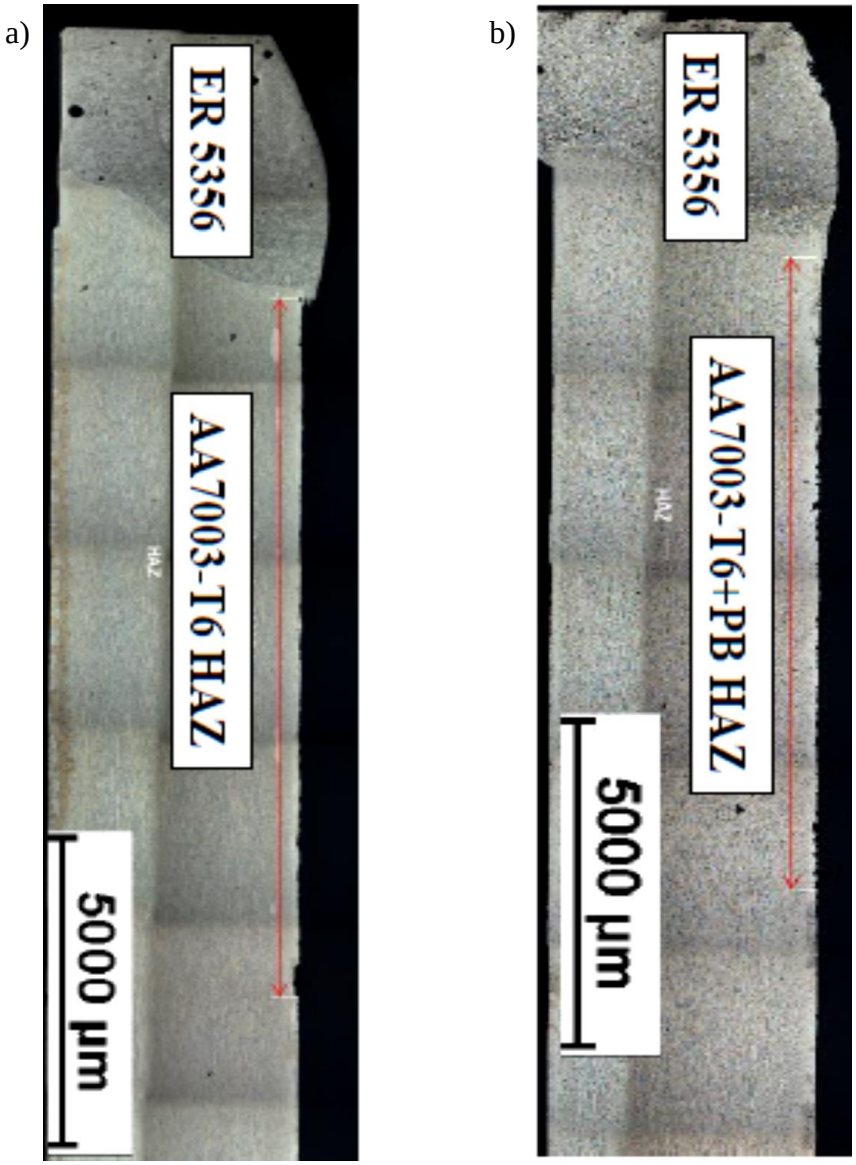

Figure D6 Large area scans of lap-joint welded configuration G (ER5356/AA7003/═) in the (a) as-welded T6 condition and the (b) as-welded T6+PB condition post exposure to ASTM G85-A2.

a)

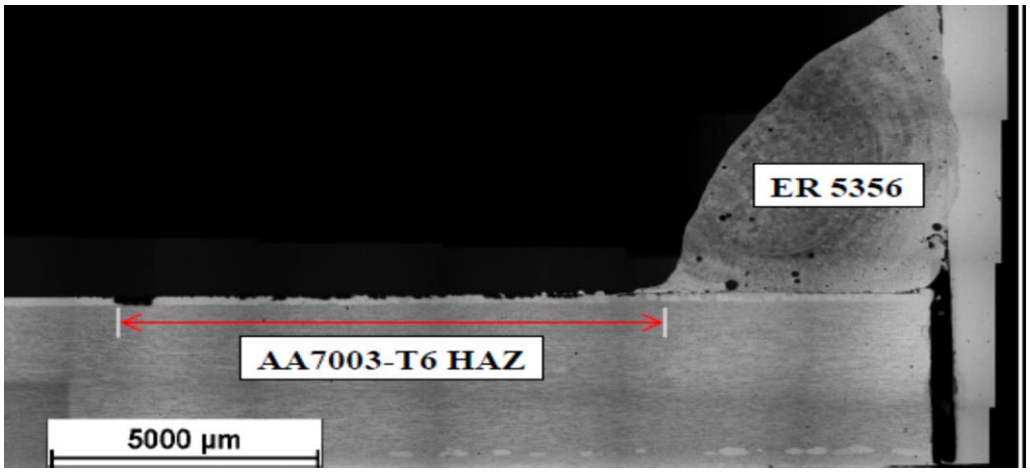

b)

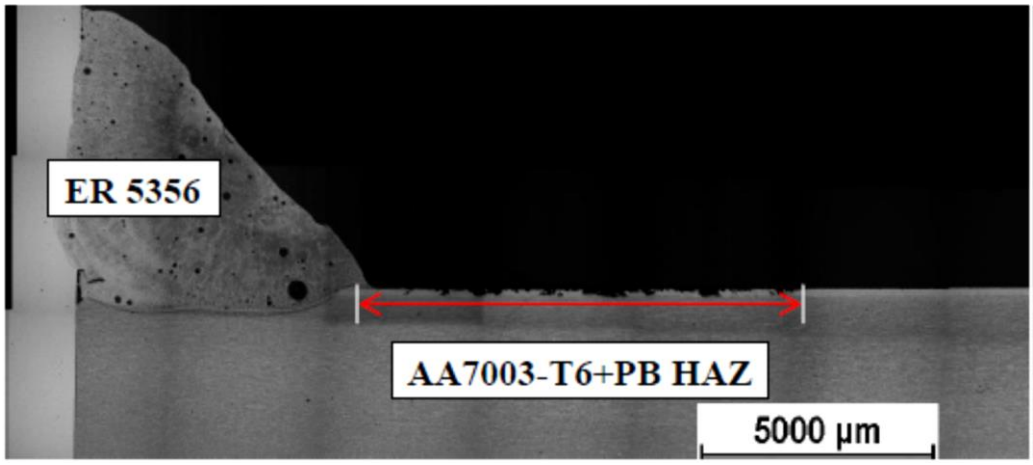

Figure D7 Large area scans of T-joint welded configuration H (ER5356/AA7003/═) in the (a) as-welded T6 condition and the (b) as-welded T6+PB condition post exposure to ASTM G85-A2.

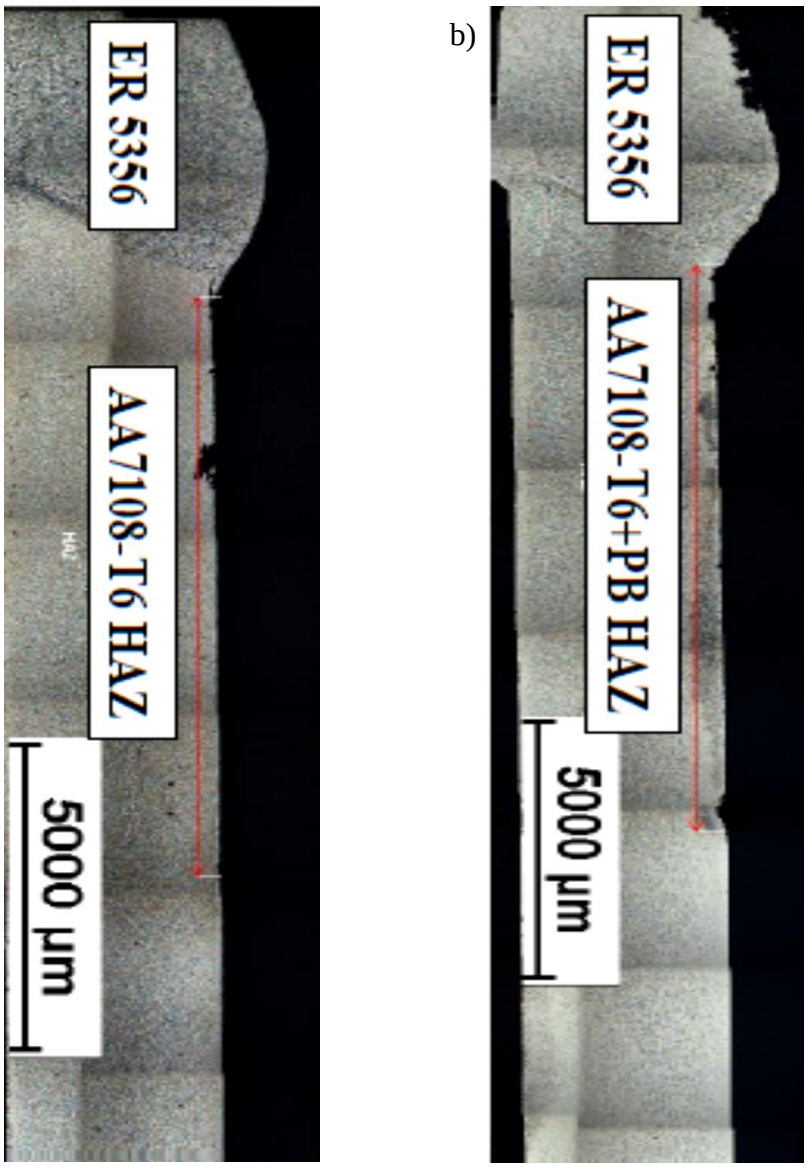

Figure D8 Large area scans of lap-joint welded configuration I (ER5356/AA7108/═) in the (a) as-welded T6 condition and the (b) as-welded T6+PB condition post exposure to ASTM G85-A2.

Appendix E – Close-up images of the Weld Region of Welded AA7003 and AA7108 samples post Exposure to GMW-14872

a)

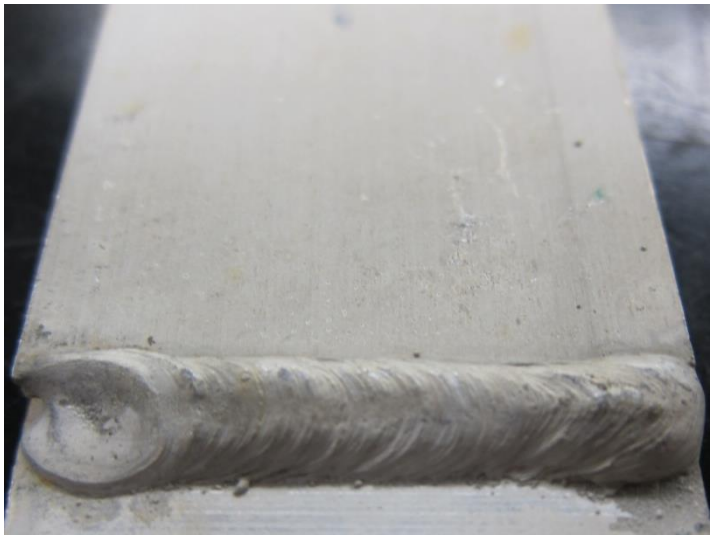

b)

Figure E1 Close-up images of lap-joint welded configuration A (ER5356/AA7003/⊥) in the (a) as-welded T6 condition and the (b) as-welded T6+PB condition post exposure to GMW-14872.

a)

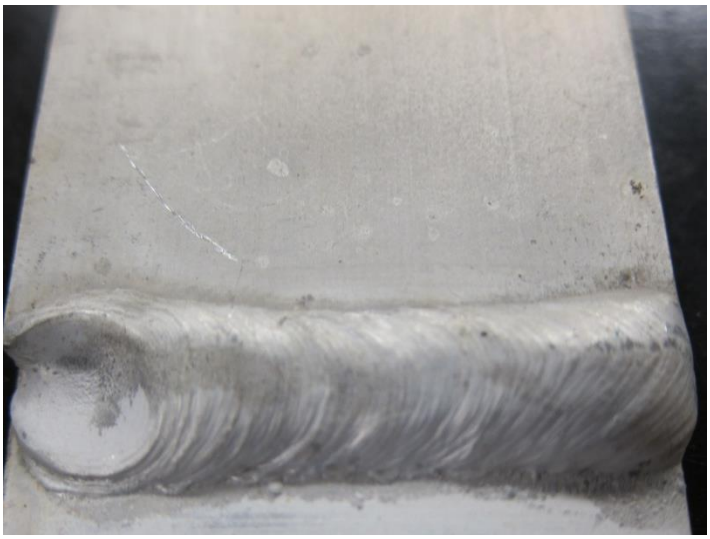

b)

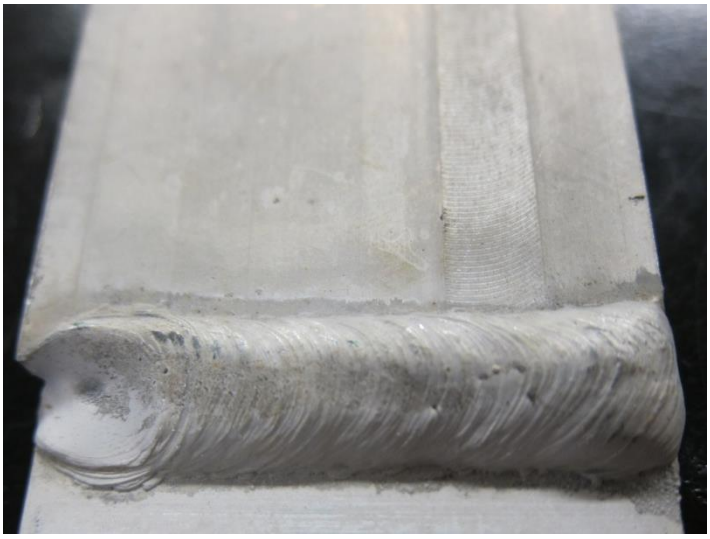

Figure E2 Close-up images of lap-joint welded configuration C (ER5356/AA7108/⊥) in the (a) as-welded T6 condition and (b) as-welded T6+PB condition post exposure to GMW-14872.

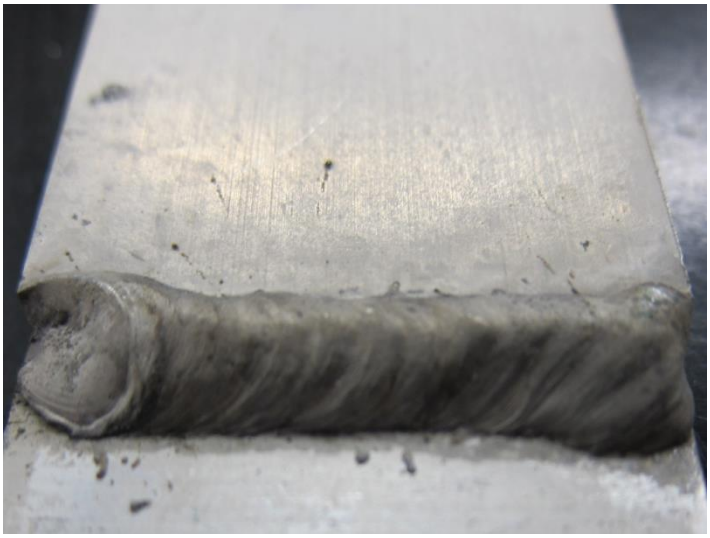

Figure E3 Close-up images of lap-joint welded configuration D (ER5356/AA7003/⊥) in the as-welded T6+PB condition post exposure to GMW-14872.

a)

b)

Figure E4 Close-up images of T-joint welded configuration E (ER5356/AA7003/⊥) in the (a) as-welded T6 condition and (b) as-welded T6+PB condition post exposure to GMW-14872.

a)

b)

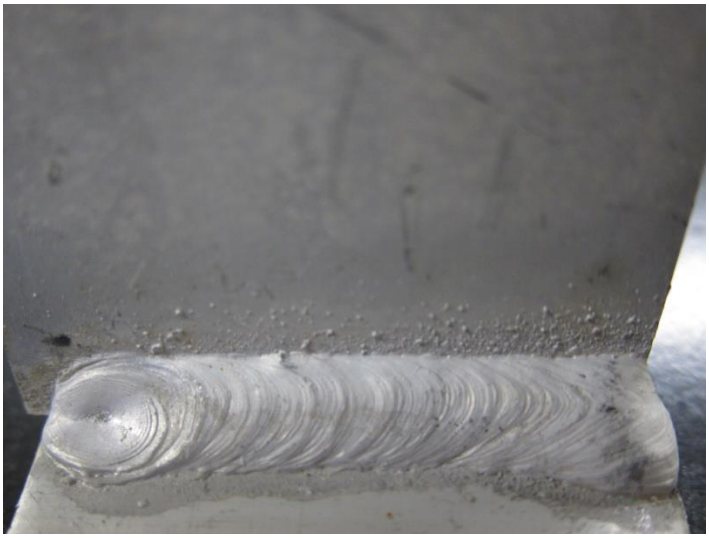

Figure E5 Close-up images of T-joint welded configuration F (ER5356/AA7108/⊥) in the (a) as-welded T6 condition and (b) as-welded T6+PB condition post exposure to GMW-14872.

a)

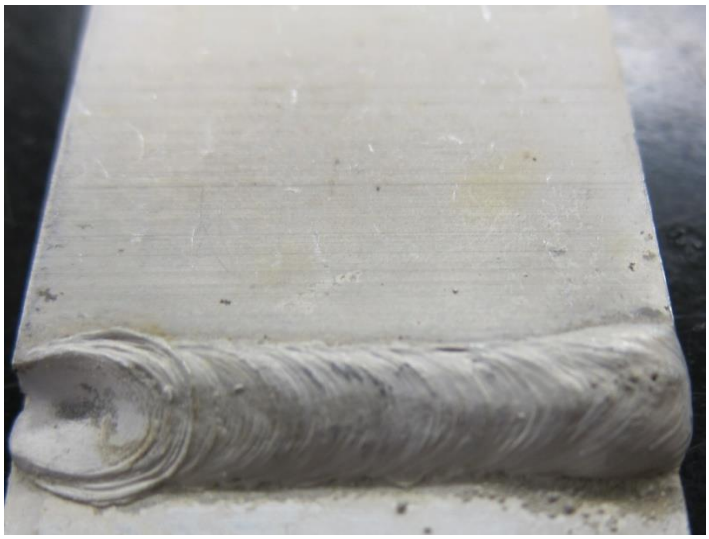

b)

Figure E6 Close-up images of lap-joint welded configuration G (ER5356/AA7003/═) in the (a) as-welded T6 condition and (b) as-welded T6+PB condition post exposure to GMW-14872.

a)

b)

Figure E7 Close-up images of T-joint welded configuration H (ER5356/AA7003/═) in the (a) as-welded T6 condition and (b) as-welded T6+PB condition post exposure to GMW-14872.

Figure E8 Close-up images of lap-joint welded configuration I (ER5356/AA7108/═) in the (a) as-welded T6 condition and (b) as-welded T6+PB condition post exposure to GMW-14872.